

ANALYSIS OF COMPLETE CONTACT PROBLEMS WITH PARTICULAR REFERENCE TO GAS TURBINE ENGINES

Thesis submitted to the Department of Engineering Science, University of Oxford in partial fulfilment of the requirements for the degree of Doctor of Philosophy

by

ARUN P. BALASUBRAMANIAN

LINACRE COLLEGE

OXFORD

TRINITY TERM, 2017

Abstract

Frictional contacts are often found in different engineering assemblies (for e.g., dovetail/fir-tree contact) and are frequently subjected to constant centrifugal loads, vibration and other forms of cyclic loads and cause a damage phenomenon called fretting fatigue. Fretting occurs mainly due to the oscillatory micro-slip between contacting interfaces and accelerates the nucleation and early propagation of cracks, and thereby causes a significant reduction in the fatigue life of the engineering components. Therefore the aim of this thesis is to study elaborately the behaviour of complete contacts, especially the interfacial conditions, in the long run to minimize the occurrence of fretting damage.

An asymptotic solution has been formulated for a particular case of complete contact, where the edge of contact is located near to an adjacent wall of material and separated by a finite clearance. Semi-infinite crack, wedge and trench asymptotes were used to investigate the behaviour of the edge of contact, when the side clearance is negligible, infinite and finite respectively. The interfacial requirements, namely the edge closure criteria and minimum coefficient of friction needed for adhered conditions, are established for internal edge angles $\pi/2$, $3\pi/4$ and $\pi/4$ radians.

The second part of my thesis concerns the study of wedging behaviour in complete contacts found in blade root assemblies. A contact is considered to be wedged when the friction present at the interface is enough to retain the deformed configuration in the absence of external load. However wedging occurs for the specific case where the coefficient of friction exceeds a particular value. A condition for the occurrence of wedging was derived in terms of the internal dovetail angle. Finite element simulations of the dovetail assembly have been carried out and the results are compared with the analytical calculations.

Attention has also been focussed on the numerical aspects of the work, where a finite element code exploiting the static reduction method was implemented for Rolls-Royce proprietary software SC03, to solve quasi-static frictional elastic contact problems. At present level of implementation, the procedure is intended to work for two dimensional, frictional contact problems where the contact interface is located approximately along a straight line.

Acknowledgement

I would like to thank my Supervisor Prof. David Hills for his excellent and able guidance throughout the course of my studies. I am extremely honoured and pleased to have worked with a person of his calibre, who cares about my work and always there to help me out with advices and suggestions. His knowledge, expertise and enthusiasm has helped me maintain the focus on the subject and enabled me reach the objective of the thesis. Apart from academics, i must say that he is a gem of a person. I have learnt a lot of personal skills from him and our professional association will be remembered sweetly forever.

I would like to thank Dr. Neeraj Cherukunnath, my co-supervisor from Rolls-Royce for his exceptional guidance and support concerning numerical aspects of the work, during the early part of my research studies.

I would like to gratefully acknowledge Rolls-Royce plc and the Technology Strategy Board for funding this work under the programme SILOET-II, Project 10, Work Package 3.0 and granting permission for its publication. I also would like to thank Mechanical Methods team in Rolls-Royce, Derby for the continuous support and encouragement.

I would like to express my sincere thanks to Dr. Robert Paynter, who generously shared his expertise on FEA of contact assemblies and various other soft skills. I also would like to acknowledge the help and support from Dr. Robert Flicek, Dr. Rodolfo Fleury and Rangarajan Ramesh. The technical discussions i had with all of them are extremely beneficial during the course of my research.

Special thanks to Dr. Jane Chanaa from Linacre college for extending much needed moral support during those difficult phases in pursuit of my PhD. I would like to extend my thanks to all my colleagues in the department, especially Matthew Ryder and Mahdi for their friendship and frequent banter, which enabled a lively work environment.

Finally, i would like to thank my family members for the endless support and encouragement through out the course of my research.

Preface

This thesis is a result of the research work carried out by the author in the Department of Engineering Science, University of Oxford, under the supervision of Professor David A. Hills. The research is original and no part of it has been submitted for a degree at this university or elsewhere. The work of others has been drawn freely though with due acknowledgement in the text.

Some of the work described in this thesis has been published in the following papers:

(i) Balasubramanian, Arun., and Hills, David., (2017), Partial slip under complete contacts near adjacent corners. *The Journal of Strain Analysis for Engineering Design*, 52(6). 380-388.

(ii) Balasubramanian, Arun., and Hills, David., (2017), Complete contacts in almost conforming sockets. *The Journal of Strain Analysis for Engineering Design* (Under review)

(iii) Balasubramanian, Arun., and Hills, David., (2017), *Response of complete contacts subjected to cyclic loading* (To be submitted)

Contents

Abstract i

Acknowledgement ii

Preface iii

Contents iv

List of Symbols vii

1 Introduction 1
- 1.1 Motivation . . . 2
- 1.2 Contact mechanics . . . 4
  - 1.2.1 Historical background . . . 4
  - 1.2.2 Types of contact problems . . . 7
- 1.3 Literature review . . . 11
  - 1.3.1 Friction . . . 11
  - 1.3.2 Fretting fatigue . . . 12
  - 1.3.3 Complete contacts . . . 17
  - 1.3.4 Frictional shakedown . . . 20
- 1.4 Summary of thesis . . . 22

2 The Semi-infinite crack problem & its application to closely fitted contact problems 24
- 2.1 Introduction . . . 24
- 2.2 Description of problem set-up . . . 26
- 2.3 Introduction to linear elastic fracture mechanics . . . 29
  - 2.3.1 Motivation . . . 29
  - 2.3.2 Linear elastic crack tip field . . . 31
- 2.4 Governing asymptotic formulation and its application to representative contact problems . . . 35
  - 2.4.1 Formulation for the block resting in a closely fitted trench . . . 36

2.4.2 Application to finite example contact problem . . . 41
2.5 Conclusion . . . 52

3 Semi-infinite Trench formulation and its application to contact problems with finite Edge Separation 54
3.1 Introduction . . . 54
3.2 Asymptotics of a block resting on a free surface . . . 55
3.3 Solution methodology . . . 59
3.4 Setting up of the asymptotic form . . . 61
3.5 Influence of non-singular terms (T-stress) on the behaviour of the contact . . . 68
3.6 Displacement component formulation for T-stress . . . 71
3.6.1 Derivation of radial displacements u_r . . . 72
3.6.2 Derivation of tangential displacements u_θ . . . 74
3.7 Application to finite models . . . 75
3.8 Conclusion . . . 81

4 Analysis of complete contacts with inclined sides in the form of a trapezium 83
4.1 Motivation . . . 83
4.2 Response of contacts with internal angle $\pi/4$ radians . . . 85
4.3 Response of contacts with internal angle $3\pi/4$ radians . . . 88
4.3.1 Asymptotic structure: Very small edge clearance . . . 89
4.3.2 Asymptotic structure: Very large edge clearance . . . 94
4.3.3 Asymptotic structure: Small edge clearance . . . 97
4.4 Initial observations of overall contact behaviour . . . 103
4.4.1 Motivation . . . 103
4.4.2 Analysis of contact behaviour for extreme geometries . . . 104
4.5 Discussion of results . . . 107
4.6 Conclusion . . . 110

5 Frictional shakedown and self-wedging 113
5.1 Introduction . . . 113
5.1.1 Shakedown . . . 114
5.1.2 Critical coefficient of friction . . . 115
5.2 Simple Force Resultant Considerations . . . 117
5.3 Finite element model . . . 120
5.4 Results . . . 121
5.4.1 Wedging and sliding as a function of coefficient of friction . . . 123
5.4.2 Wedging and sliding as a function of internal angle . . . 125
5.4.3 Contact behaviour as a function of blade geometry . . . 126
5.5 Conclusion . . . 130

6 Static Reduction method **131**
6.1 Motivation . . . 131
6.2 Introduction . . . 133
6.3 Literature review . . . 134
6.4 Mathematical description of Static Reduction method . . . 136
6.4.1 Elimination of degrees of freedoms using a Static Reduction process . . . 136
6.4.2 Recovery of the eliminated degrees of freedoms using back-substitution . . . 138
6.5 Application of Static Reduction method to general contact problems . . . 139
6.5.1 Single elastic body in contact with a rigid body . . . 140
6.5.2 Contact between two elastic bodies . . . 147
6.6 Partitioning of reduced contact stiffness matrix . . . 150
6.7 Time evolution solution algorithm for frictional Quasi-static contact problems . . . 152
6.7.1 Introduction . . . 152
6.7.2 Frictional constraints . . . 153
6.7.3 Solution procedure . . . 154
6.7.4 Algorithmic setting . . . 155
6.7.5 Application of Static Reduction procedure to example numerical models . . . 159
6.7.6 Introduction . . . 159
6.7.7 Frictional contact of an elastic block in contact with a rigid plane . . . 159
6.7.8 Frictional contact of an elastic body in contact with another elastic body . . . 161
6.7.9 Conclusion . . . 168

7 Concluding remarks and future work **170**
7.1 Overview . . . 170
7.2 Conclusion . . . 172
7.3 Future work . . . 175

Bibliography **178**

Appendix A User subroutine to assign displacement boundary conditions **190**

List of Symbols

f	Coefficient of friction
K_I^N, K_{II}^N	Notch stress intensity factors
P	Normal load
Q	Shear load
K_I, K_{II}	Crack stress intensity factors
σ_0	T-stress
a	Size of the block
d	Width of the finite clearance
r,θ	Polar coordinates
E	Young's modulus
υ	Poisson's ratio
κ	Kolosov's constant
$\sigma_{\theta\theta}$, σ_{yy}	Tractions in normal direction in polar and rectangular coordinates
$\sigma_{r\theta}$, σ_{xy}	Tractions in shear direction in polar and rectangular coordinates
u_r, u_θ	Radial and tangential displacements
λ_I, λ_{II}	Eigen-values for mode I and mode II singularities

f^n_{Edge}, f^{cr}_{Edge}	Coefficient of friction calculated by wedge and crack asymptotes
f_c	Critical coefficient of friction
F_N	Contact reactions in the vertical direction
F^s_0	Force applied in the upward direction to enable sliding
F^U_0	Force applied in the downward direction to enable sliding
P_0	Resultant contact loads in the vertical direction
P_{max}	Maximum load applied to the shank portion of dovetail
f^c	Total contact reactions
f^w	Contact reactions due to external loads
p_j, q_j	Normal and tangential nodal reactions
w_j, v_j	Normal and tangential nodal displacements
K, K^C	Global and contact stiffness matrices
u^C	Contact displacement vector
ϵ	Tolerance computed at each time step

Chapter 1

Introduction

The aim of this thesis is to develop methods to be used to analyse the frictional response of complete contacts observed in practical engineering applications. A complete contact is one where the contacting surface of the undeformed bodies conform, and the contact size is established by a discontinuous slope ("edge") in one contacting body. In this context the turbine fan blade root is "almost complete" . The blade to disc interface present in the blade root assemblies of gas turbine engines often pose various structural problems. Therefore an accurate prediction of the response of contacts is essential from the design point of view. This thesis is divided in to three parts and the following aspects are addressed: (i) Development of numerical methods to analyse contact problems using static reduction techniques (ii) Shakedown studies on a typical dovetail component used in blade root assembly and the occurrence of self-wedging at characteristic physical coefficient of friction (iii) Partial slip problems in complete contacts with particular reference to the adjacent stress concentrators. Motivation of the physics of the problem in the context of industrial needs is addressed. A brief review of theoretical concepts of contact mechanics has been done. Literature related to complete contacts and fretting fatigue are reviewed. Finally a short summary of the outline of thesis is presented.

1.1 Motivation

Engineering components are very frequently subject to fatigue loading due to their operating conditions eg., mechanical vibrations. If the resulting cyclic load is severe enough and persists for an extended number of cycles, material failure is expected eventually as a result of propagation of fatigue cracks. Unfortunately, fatigue failures can be extremely difficult to predict accurately, because the failure can occur at stresses well below the yield limit of the material throughout the service life of the component. Consequently, research in the area of fatigue failure has been ongoing for over 150 years (Schutz [1996] [1]) and although much progress has been made, many critical problems still need to be studied. The primary motivation for research in fatigue failure comes from the fact that numerous engineering structures fail in this manner. These failures invariably cause major financial losses and at times lead to fatalities. Even with the absence of any such failures, gaps in our current understanding of fatigue still increase the operational costs of the engineering projects. This is because of the lack of accurate prediction methods, which are compensated for by adopting conservative methods in every day operations & design.

While such conservatism does not always incur an unacceptably high cost, in certain applications, e.g. the gas turbine engines used in aerospace industry, a marginal increase in component weight leads to other undesirable effects that significantly decrease the overall efficiency of the component. Hence, in many cases, there is a very strong incentive to improve the current approaches for predicting the fatigue performance of engineering components in extreme operating conditions.

Another commonly observed failure mechanism in aero space components arises when two parts are in frictional contact with each other and are subject to relative movement due to the mechanical vibrations happening in the engine. This phenomenon of fatigue that is happening

due to the contact between the bodies and a small relative slip on the interface is termed *fretting fatigue*. One common example of where this damage process occurs is the blade to disc assembly of gas turbine engines (refer Figure 1.1). In order to facilitate maintenance and replacement of blades in the engine, it is traditional not to weld them to the disc, but simply by slide the root of the blades in to the disc. This paves the way for some slip between the blade and disc interface, during engine operating conditions, which then accelerates crack initiation near the contact interface. Fretting fatigue has been the topic of research for many years, especially in the aerospace industry. The first recorded literature concerning fretting fatigue was published by Eden *et al.,* [1911][2]. Then later Waterhouse [1992][3] summarised different aspects of fretting fatigue problems.

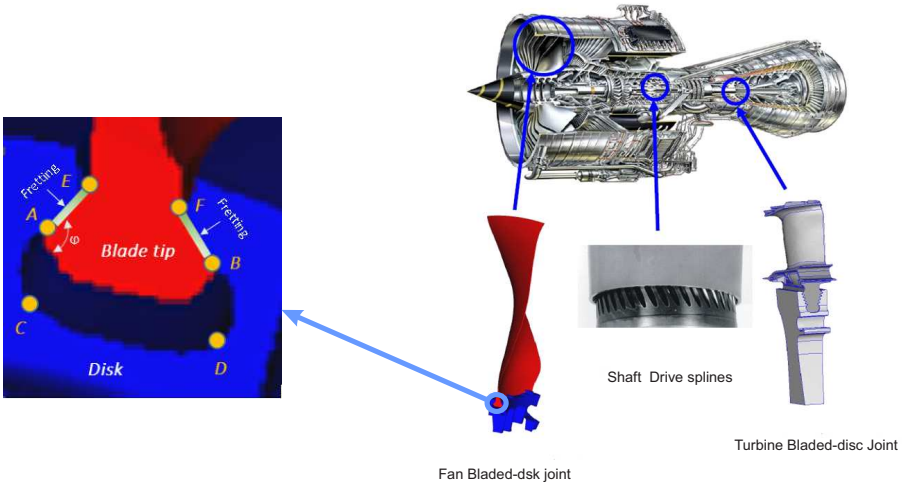


Figure 1.1: Bladed disk contact of an Aero engine component showing the region of stress concentration and Fretting Fatigue (AE and FB)

The objective of this thesis is to develop methods that augment existing techniques in assessing the fretting performance of the engineering components when subjected to high cycle fatigue. The life of the components subjected to fretting damage is primarily dependent on the conditions that arise out of the region where the fretting accumulation occurs and the fatigue cracks initiate. This occurs along the edge of contact, where the damage process is accelerated

by the stress concentration effects in the region. Since most of fretting damage is localized along the edge of contact, the methods developed in this thesis emphasize these regions to bring an accurate description of stress state locally. Efficient numerical algorithms have been presented to run FE analysis of the contact problems in a shorter period of time, which in turn facilitates the determination of conditions under which a frictional system may shake down when subjected to periodic loading.

1.2 Contact mechanics

1.2.1 Historical background

Contact mechanics is a niche area and is an essential part of solid mechanics. Contacts play a major role in transferring loads to a deformable body (the only other way is body forces) and therefore it is extremely critical to analyse the resulting reactions along the interface of each component. The origin of contact mechanics started from the early part of 1882, where Hertz recorded his research on frictionless contact of two elastic bodies of elliptical profile. Hertz's analytical model involving elastic contacts was a breakthrough in the field of contact mechanics and is still used by many researchers to study a wide contact problems. Since then several researchers have made significant contributions to the field of contact mechanics and the subject has evolved quite rapidly.

The subject of contact mechanics has been reviewed by many people including Carter [1922][4], Cattaneo [1938][5] and Mindlin [1949][6], Muskhelishvili [1953a,b][7][8], Gladwell [1980][9], Johnson [1985][10], Hills *et al.,* [1988][11], Barber [2008][12] and Ciavarella [2007][13].

Carter [1922][4] was the first to solve rolling contact problem incorporating shear tractions, where he tried to relate linearly the tractive force and wheel creep in rails, and idealised the

problem by assuming both bodies as two-dimensional half planes. Twenty years later Cattaneo [1938][5] and Mindlin [1949][6] made significant advances in studies of partial slip contacts. They independently developed a solution for the problem of a stationary Hertzian contact pressed by a normal force P and subsequently by a sinusoidal shear force $Q(t)$. Their solution provides a basic understanding of the contact tractions in partial slip problems and contributed immensely to advancements in fretting fatigue tests. Another significant extension to the original partial slip solution was obtained by Hills *et al.,* [1988][11], where they showed how the contact tractions are modified by the application of super-imposed bulk tension. Since the bulk load is commonly present in both the experimental specimen and engineering reality, the solution was extremely helpful in investigating fretting fatigue experiments.

Muskhelishvili's [1953a][7] research showed how the complex variable method explained in his monograph was significant in solving contact problems. Gladwell [1980][9] summarised various contact geometries that had been solved in the previous decades. Johnson [1985][10] provided insights into a range of contact problems including line/point loading of an elastic half space, normal contact of elastic half space (Hertz theory), normal contact of in-elastic solids, tangential loading and sliding contact, rolling contact of in-elastic bodies, calendering and lubrication, dynamic effects and impacts, thermo elastic contact, and rough surface contacts.

Application of linear elastic fracture mechanics formulation to solve contact propelled crack problems was initiated by Fleming *et al.,* [1977][14], where he developed a mathematical model of subsurface crack propagation to infer the delamination response of a sliding contact. They also developed an equation to predict wear rate, which should apply in delamination wear to materials in which crack nucleation is easy. Dundurs and Comninou [1979][15] studied the importance of inequalities and related conditions to be incorporated in contact and crack problems, and explored the ensuing consequences. An asymptotic analysis of transitions from slip to separation, stick to slip, and stick to separation was carried out.

Liu and Tan [1992][16] used the boundary element method (BEM) for two-dimensional contact mechanics analysis, which was then applied to solve a number of angled crack problems involving crack surfaces in contact. Their formulation is based on a quadratic iso-parametric boundary element, and using which they quantified the near tip fields for both open and closed crack tips. The crack tip region was modelled in the analysis using special elements with mid-side nodes. Their research shows that friction between the crack surfaces in contact can indeed have a significant effect on the crack tip stress intensity factors.

Jäger [1998][17] and Ciavarella [1998a,b] [18][19] published significant results on partial slip problems, mainly developed for contacts of any profile to which a half-plane idealization can be applied. This enabled Ciavarella [1998][18] to obtain the partial slip solution for contact between a flat and rounded punch and a half plane, which has important applications in modelling Dovetail/Firtree joints in the blade root assembly of a gas turbine engine.

Churchman and Hills [2006][20] focussed their studies on shakedown effects in complete contacts. Their numerical analysis of complete contacts reveals that when subjected to cyclic loads the contact some times shakes down after few loading cycles. The favourable residual displacement locked in during this phase inhibits slip in the subsequent cycles. This subject was then studied in depth by Klarbring *et al.,* [2007][13] for discrete contact problems and by Barber *et al.,* [2008][12] for continuum problems.

Contact modelling of rough surfaces presents much difficulties due to the distinct nature of contact at the asperities. The arbitrary shape of the asperities coupled with anisotropic behaviour makes it a challenging task to develop analytical models to characterise their behaviour. The first stochastic model to analyse the elastic and plastic contacts of rough surfaces was developed by Greenwood and Williamson [1966][21]. They assumed the surfaces in the form of hemispherically tipped asperities of uniform radius of curvature and used a gaussian distribution to characterise their heights. Nayak [1973][22], Bush et al., [1975,1979][23],[24]

and Gibson [1982][25] developed elastic contact model that modelled asperities as elliptical paraboloids with randomly oriented elliptical contact areas. However statistical models are often limited by the abstractions on the asperity geometry and height distributions. The advent of computer technology enables digitization of profiles measured for different surfaces and predict the contact behaviour much quicker. Earlier research shows that finite element methods were used to simulate plane strain elastic contact problems with less number of cylindrical asperities in contact. Tian and Bhushan [1996][26] adopted a variational approach that uses direct quadratic mathematical programming to study 3-D rough surface contact problem with larger number of contact points. The method guaranteed the uniqueness of the solution and significantly reduced the computational time. Bailey and Sayles [1991][27] and Yu and Bhushan [1996][28] analyzed the sub-surface stress fields and the effect of friction on the contact stresses and contact area. Merriman and Kannel [1989][29] and Cole and Sayles [1992][30] developed a 2-D model to analyse the contact of layered rough bodies. Oden and Martins [1985] [31] and Martins et al., [1990][32] developed a continuum model of sliding of two rough surfaces to be used with a finite element method.

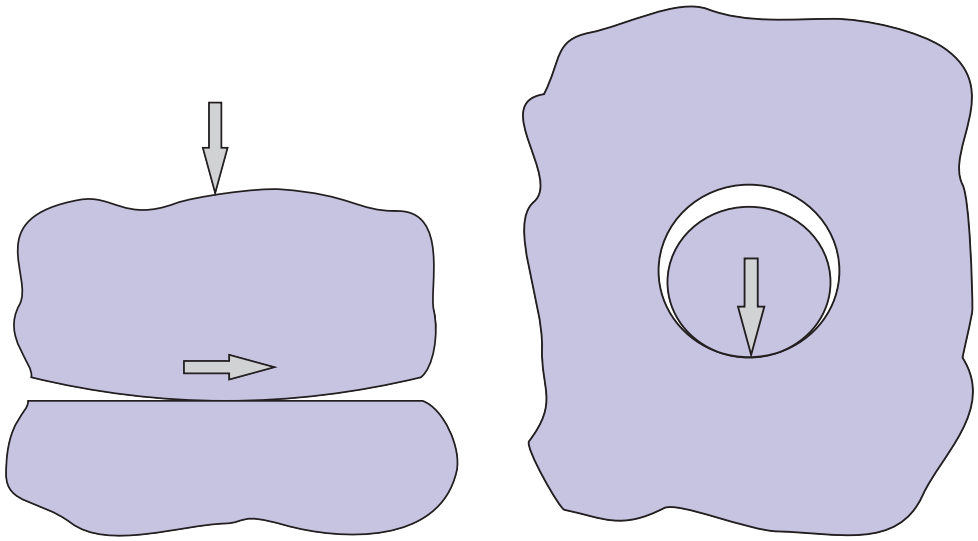
1.2.2 Types of contact problems

Contacts can be broadly classified in to two categories namely *conforming* and *non-conforming* contacts. By definition, the conforming contacts are those with a finite contact extent when no external loads are applied and this implies that the contact is defined purely by the geometry of at least one of the contacting bodies. On the other hand, non-conforming contacts (often termed as *in-complete* contacts) are characterized by infinitesimal contact area in the absence of external loads. Here the contact zone is small compared to the actual size of the contacting body and as we move closer to the contact zone, the influence of the far regions can be neglected and

the arrangement can be idealised as half-planes or half-spaces, which helps in simplifying the problem definition and deriving analytical solutions. These definitions imply that in-complete contacts are characterized by smoothly varying curved bodies, whereas the conforming contacts are formed between bodies where the edges have definite sharp profiles.

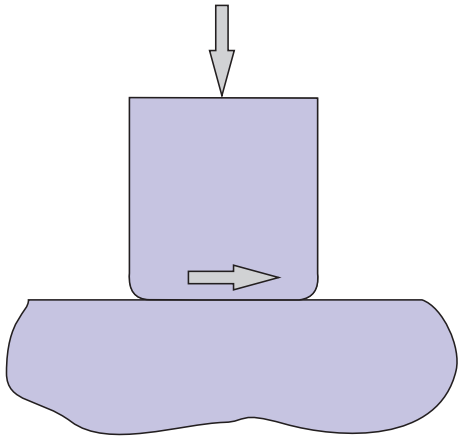
The different categories of contacts are shown in Figure 1.2. In-complete contacts are shown in Figure 1.2a-1.2b, while conforming contacts are shown in Figure 1.2c-1.2f. The pressure distribution for in-complete contacts tend smoothly to zero as the contact edge is approached. Although the contacts shown in Figure 1.2a and 1.2b are grouped under same category, there lies a difference in the way the contact model is idealised. As discussed before, the contacting bodies shown in Figure 1.2a can be modelled as half-planes, considering the fact that size of the contact area is much less than that of actual size of contacting bodies. Whereas for the pin in hole type contact, the contact area is appreciable when compared to the dimensions of the contacting body and the curvature is too high and therefore it may not be possible to idealise this contact using half-plane approach. The flat and rounded contact shown in Figure 1.2c is categorised as a conforming contact, since major portion of the contact area is defined by the geometry of the upper contacting body. But then, because of the smooth edges, locally the contact behaves as in-complete and the size of contact zone there depends on the externally applied loads. The flat and rounded contact exhibits a more complex pressure distribution than the other two in-complete contacts described above, and it gives a bounded pressure distribution as the edge is approached. Therefore, in some ways, flat and a rounded contact can be seen as a transition between conforming and non-conforming contacts.

Complete contacts, on the other hand, are defined as those where the size of contact zone is independent of the applied external loads. Because of the presence of sharp edges, these contacts usually exhibit a singular pressure distribution adjacent to the edges. The order of singularity depends on the contact edge angle, degree of material dissimilarity of the contacting bodies,

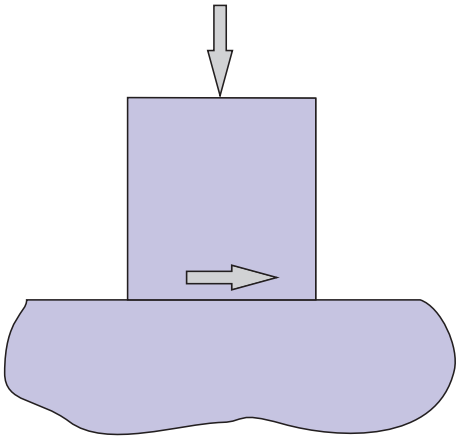


(a) In-complete contact

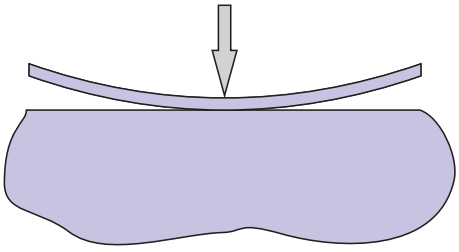
(b) Pin-in hole contact



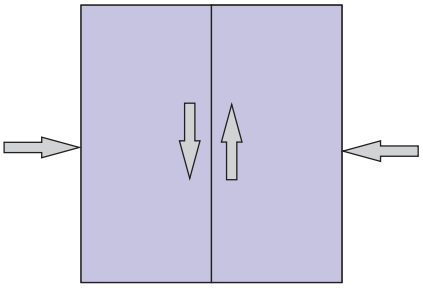
(c) Flat and rounded contact



(d) Complete contact



(e) Receding contact



(f) Common edge contact

Figure 1.2: Types of contact models

and the coefficient of friction. A typical example of a complete contact is shown in Figure 1.2d where an atomically sharp punch makes contact with a half-plane. The edges of complete contacts may some times 'lift off' due to the application of shear and this consequently reduces the size of contact zone. Thus it can be concluded that the size of contact zone observed in a complete contact may decrease as a result of applied loads, but cannot increase.

Receding contacts are defined as the class of contacts where the size of the contact zone decreases on application of load as shown in Figure 1.2e. It was shown by Dundurs and Stippes [1970][33] that when a monotonically increasing normal load is applied to these contacts, the edges tend to lift off, accompanied by an adjacent slip region. Because of significant separation occurring near the edges, the contacts behave as in-complete ones locally and therefore a bounded pressure distribution is observed. From an alternative definition of receding contact, it can be said that the size of contact area never increases, and this implies that all complete contacts are also receding contacts.

A typical common edge contact is shown in Figure 1.2f, where the contact area is defined by both bodies simultaneously, and it shares the edges of both bodies. Unlike the other contacts which have been discussed above, the pressure distribution for common edge contacts assumes a finite value all along the whole interface. However, in engineering applications it is very unlikely that we observe a contact with perfect alignment and hence the practical applicability of common edge contacts at one scale are quiet slim. In the event of any misalignment, the common edge contact then tends to behave as complete contacts very locally near the edge. Therefore, when analysing common edged contacts, some factor of misalignment needs to be considered and the edge ought to be treated as “complete”.

1.3 Literature review

1.3.1 Friction

Friction can generally be defined as the resistance to movement when two surfaces slide against each other. In simple terms it can be defined as the measure of tangential reaction force between two surfaces in contact. Physically these reaction forces results from many different mechanisms, which may depend on the contact geometry and topology, material properties of contacting bodies, displacement and relative velocity of the bodies, presence of lubrication etc.

The first friction model came from Leonardo Da Vinci [1452-1519], where he measured the force of friction between objects on both horizontal and inclined surfaces and later recognised the difference between rolling and sliding friction and the beneficial effect of lubricants. Robert Hooke [1653-1703] discussed the question of sticking and adhesion in the context of elastic and in-elastic deformation happening along the contact. Guillaume Amontons [1663-1705][34] of France extended the studies on friction by publishing significant results in a classical paper presented to the Académie Royale in 1699. These results were later confirmed and expanded by Coulomb [1785][35]. He then went on to develop the well known friction model called *Couloumb friction*, which is still being used by the scientific community involved in friction related studies. It simply states that the frictional force along a sliding interface is directly proportional to the applied normal force.

Thus for a typical sliding contact, the total shear force along the interface is defined as $Q = fP$, where P is the total normal force and f is the coefficient of friction. Thus Coulomb´s friction law assumes that the frictional force is independent of the contact area and the relative sliding velocity. The numerical algorithm developed for solving quasi-static contact problems in this thesis (refer chapter §6.7) makes use of Couloumb's friction law to resolve the contact

constraints (inequalities) along the interface. The frictional slip that occurs along the contact can be broadly classified into *partial slip* and *gross sliding*. Gross sliding can be termed as the relative rigid body movement of the contacting bodies, whereas partial slip problems can be defined as the case where some particles of the contact will be in an adhered condition throughout the loading regime, while the rest may be in slip. Couloumb's law was initially developed for addressing the effects of gross sliding, although it could also be applied for the partial slip problems in a discrete or pointwise sense. The partial slip occurring in contacts leads to a phenomenon called *fretting fatigue*, whereas gross sliding can cause *fretting wear*. The analysis done in this thesis mainly concerns partial slip problems, which address the fretting fatigue phenomenon.

1.3.2 Fretting fatigue

Fretting fatigue is a type of damage that occurs in the regions of contact between two parts such as that of blade/disc interface in the dovetail region of a gas turbine engine. It is characterized by relatively small displacements during vibratory loading, where only a portion of the edge of contact moves, termed slip, while the remainder of the contact region sticks. The relative displacements are typically of the order of tens of microns or less and are difficult to reproduce under laboratory conditions. As a consequence of this, surface damage and crack initiation are likely to occur. Furthermore, if the fretting of the surface of contact is combined with cyclic loads on one of the bodies, then the crack initiation and propagation may be accelerated, causing a significant reduction in the fatigue life of the component. This process of fretting fatigue can cause a life reduction of as much as ten times the standard fatigue life (Hills and Nowell [1994][36]). Thus, a better understanding of mechanisms (partial slip conditions) that contribute to the fretting fatigue phenomenon is critical to predict accurately the life of the

components in extreme loading conditions.

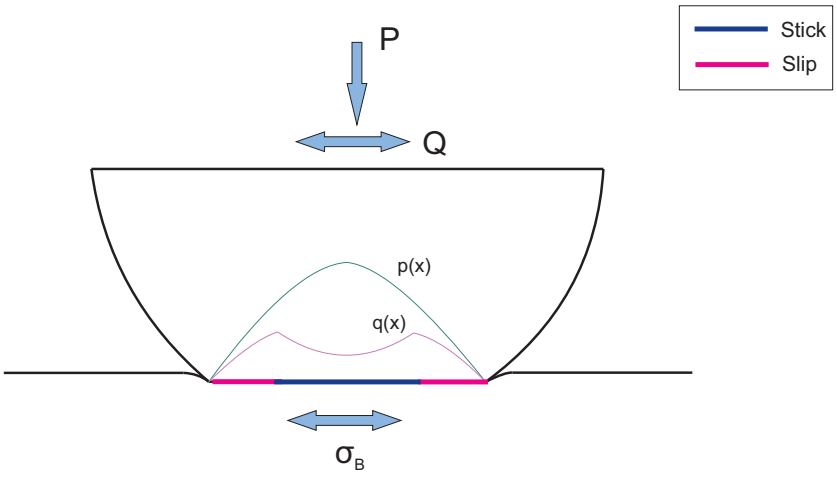


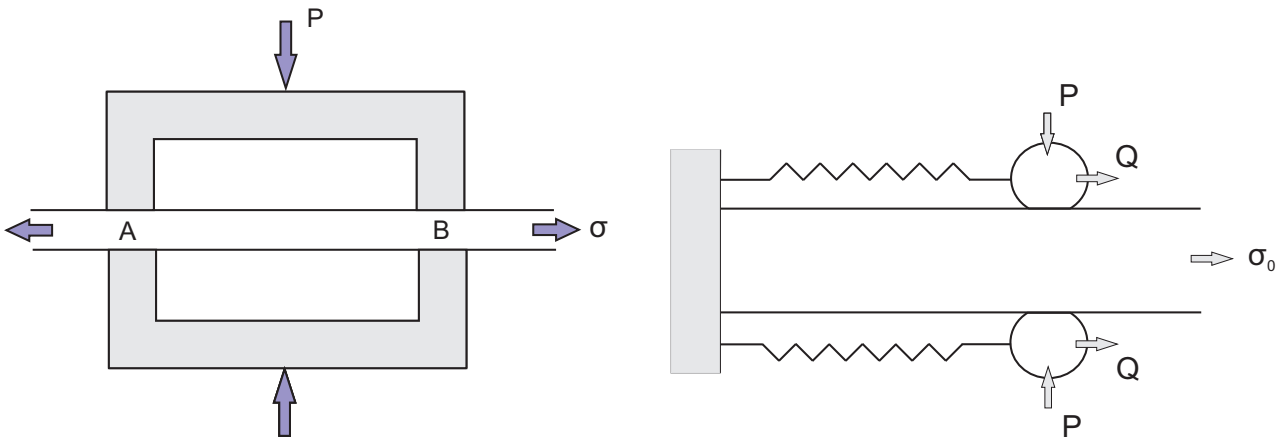
Figure 1.3: Hertzian contact: Partial slip configuration

Depending upon the displacement behaviour across the contact interface, different types of surface damage may be expected. Vingsbo and Söderberg [1988][37] studied the importance of different regimes of fretting. Under adhered conditions it is unlikely that surface damage occurs along the contact. For smooth and curved surface contacts (e.g. Hertzian contact), slip zones may be observed at the edges with a central stick zone as shown in Figure 1.3. Surface damage and wear are expected to occur along the region where the contact is subjected to slip. This partial slip behaviour then leads to crack initiation and when combined with bulk cyclic tension may lead to fretting fatigue. Gross sliding of the components commences when the applied tangential force equals the total frictional force along the contact. Fouvry *et al.*, [1996][38] have showed that under these conditions, wear occurs along the contact at a rate exceeding the crack propagation rate and so increases the fatigue life of the component. However with persistent surface wear, failure may occur due to reduced bulk strength of the component.

Fretting fatigue has been studied extensively for the past three decades, with both analytical and experimental models very well established for simple geometries and isotropic materials.

Fretting experiments to evaluate the fatigue life of components stared as early as 1927 by Tomlinson [1927][39], who designed fatigue test machines to study the partial slip behaviour. Their experiments revealed that slip amplitudes of the order of $0.1\mu m$ were sufficient to cause fretting damage. Experimental investigations of fretting fatigue have undergone significant advancements since then. The most commonly used mode of testing was the usage of 'bridge' type fretting pads (refer Figure 1.4a) and these remained popular until the early 1990's. The simplicity of the apparatus enabled normal fatigue specimen to be used either in bending or cyclic tension. The bridges are simply clamped to the sides of the specimen by a proving ring and the cyclically strained specimen cause relative movement between the bridge feet and the specimen. However difficulties are encountered with such an arrangement at large loads, where the bridge is subjected to excess bending and the contact response may not reveal the true characteristics of the problem. Nishioka and Hirakawa [1972][40] published significant results during the late 1960's and early 1970's. They used a contact configuration with cylindrical pads clamped against a flat specimen (refer Figure 1.4b). The test geometry has a number of advantages: pad alignment is less critical and the contact stresses may be obtained by performing classical contact analysis. Further, the critical parameters for subsequent stress analysis (normal Load P, tangential load $Q(t)$, specimen remote stress $\sigma(t)$ may all be readily measured and controlled). The geometry has since been adopted by a large number of other researchers, including Bramhall [1973][41] and Hills et al., [1988][11]. The normal load is fixed usually, whereas the tangential load is cycled and applied using springs.

Other types of experiments were carried out which closely mimics the geometry of the real components e.g., dovetail assembly. Such experiments were performed by Ruiz et al., [1984][43], Papaniknos and Meguid [1994][44], and Conner and Nicholas [1994][44]. An enhanced version of Ruiz's apparatus is still in use at Oxford and is shown in Figure 1.5. The blade loads representing the centrifugal force in the engine are applied to two opposing blade specimens.



(a) Bridge type pads **(b)** Cylindrical pads

Figure 1.4: Geometry used for fretting fatigue analysis (Nowell et al., [2006][42])

These are mounted in a central disk specimen, which is also subjected to load, simulating the disk expansion under centrifugal loading. The relative slip in the engine can be accurately represented using these loading conditions, which may be important for wear of coatings. The blade vibration is simulated by the high cycle fatigue loads which are applied by the mechanical shaker units clamped to each blade.

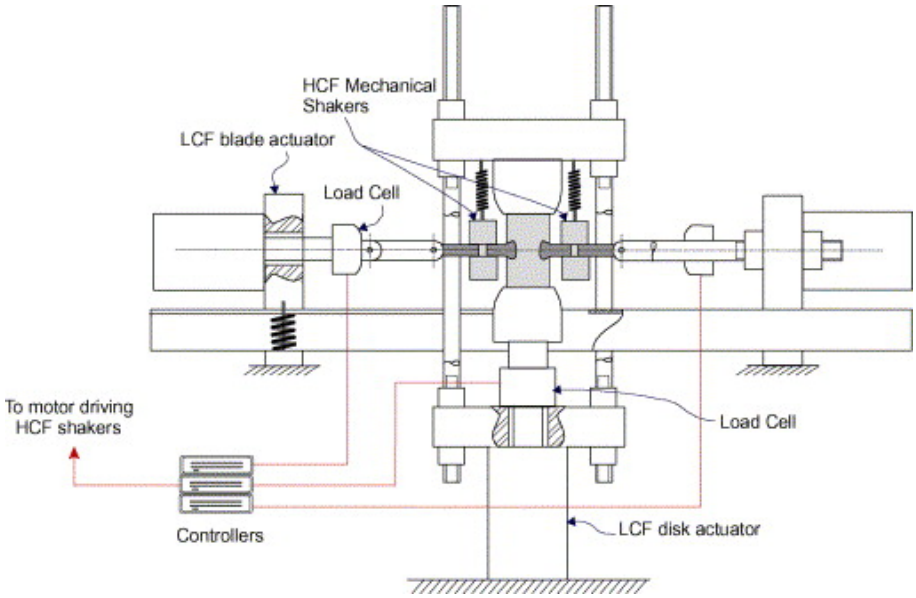


Figure 1.5: Diagram of biaxial dovetail fretting fatigue apparatus used in Oxford (Nowell et al., [2006][42])

Fretting crack formation in contacts occur due to the cyclic plastic deformation and cumulative deformation which occurs within depths of a fraction of several grains and therefore requires a thorough analysis of components at a micro-structure level. Goh et al., [2001][45] developed a crystal plasticity model to resolve the deformation behaviour at the scale of individual grains in order to understand its crystallographic behaviour and how it is connected to contact conditions. They employed state of the art constitutive models to account for the discreteness of grains, crystallographic surface texture, and heterogeneous plastic deformation at the scale of grains. They further performed 2D finite element fretting analysis using the constitutive model, to show the impact of micro-structure on the fretting deformation behaviour. Zhang et al., [2009][46] extended the studies to a more realistic three dimensional problem and substantiated earlier results that the distribution of plastic strain is heterogeneous and the dominance of ratchetting in the plastic strain field. They further evaluated the dependence of normal and tangential force components on the fatigue crack formation. McCarthy et al., [2014][47] studied the effect of grain orientation on the crack nucleation life, using J2 plasticity and conventional crystal plasticity models and compared their relative advantages.

Contact models are usually associated with roughness due to the asperity effects and consequently affects the response of the contact as compared with a smoother one. The presence of asperities concentrate the load in the smaller areas of contact and subsequently produce large stresses. The length scales of the asperities are usually quiet different to that of the overall contact. Nowell et al., [2000][48] mentioned a number of length scales pertinent to the fretting problem. Proudhan et al., [2005][49] investigated the effect of contact roughness on the crack nucleation conditions. The crack initiation phase seems to be sensitive to the surface quality, with higher the roughness, lesser is the tangential force needed to initiate the crack.

The development of asymptotic approaches enabled significant advances in fatigue life prediction of components. Several asymptotic forms were presented by Hills *et al.,* [2012][50],

where they employed successfully the formulations to correlate the fretting fatigue life of both Hertzian and flat and rounded contacts, which collapse the test results of contacts of different sizes onto the same fretting fatigue life curve. The asymptotic forms can also be used to predict accurately the transition between finite and infinite fatigue life of contacts of different sizes. The asymptotic approach used in this thesis may not relate directly to fatigue life correlation, but in some ways can be seen as an aid to understand better the partial slip phenomena occurring near the adjacent edges of the blade/disc interface in a typical dovetail assembly, which can then be used as an input for fatigue calculations.

1.3.3 Complete contacts

Complete contacts are characterised by sharp edges, which often do not arise in practical engineering applications, but one example is the spline connection between split shafts in a gas turbine engine. Design procedures for fretting fatigue in these assemblies have prompted an investigation of near-edge stress state in complete contacts. Classical contact models concerning an elastic flat punch pressed into an elastically similar half plane in the presence of friction has been studied by researchers in the past. For this kind of problem, the contact response is dependent upon the finite dimensions of the punch and therefore a closed form solution is not been available. However, for specific cases solutions are already available.

Khadem and O'Connor [1969 a,b] [51] [52] considered the problem of elastic square compressed by elastically similar half planes. They derived a numerical solution for these problems for the cases of fully adhered & frictionless contact surfaces. Mugadu and Hills [2003][53] derived a solution for the rigid rounded flat semi-infinite punch pressed in to an incompressible half plane, subjected to constant normal load, oscillatory shear load and an oscillatory bulk load within the half plane. However, the solution is applicable for specific case of materials and

may not work for elastically similar materials.

Complete contacts almost invariably present a singular state of stress adjacent to the edge of contact and therefore are very vulnerable to fretting damage close to these regions. Asymptotic procedures are invaluable in providing an accurate description of the stress state locally. The concept behind this approach is that we focus attention very close to the edge of contact, assuming the loads and boundary conditions are applied remotely. A Semi-infinite notch formulation can be applied to obtain an accurate solution for these problems, providing that the edges are sharp. Williams [1952][54] derived a solution for a semi-infinite elastic wedge subject to in-plane, remote loading and investigated the nature of stress field close to the apex of the notch. The main requirement here is that the displacement field across the domain considered needs to be continuous, and this implies that the contact we intend to study is fully adhered. Hence, if the contacting bodies are elastically similar, the presence of contact can be ignored and the edge can then be idealised as a notch with contact angle identical to the actual internal angle of the geometry and William's solution can be used to represent the stress state in the region. Most of the notch asymptotics that has been dealt in this thesis is based on William's solution.

Bogy [1968][55] derived significant further solutions for fully adhered contact between dissimilar materials. Solution for sliding frictional contact between elastically different materials was published by Gdoutos and Theocaris [1975][56] and Comninou [1976][57]. Application of asymptotic approaches to elastically similar complete contacts was started initially by Mugadu and Hills [2002][58] and later extended by Churchman [2006][20] and Karuppanan [2007][59] during their doctoral research. Churchman and Hills [2006a][60] studied the behaviour of an elastic punch pressed into an elastically similar half plane, subjected to a constant normal load and oscillating shear load. They used sliding wedge asymptotics to address and quantify the effect of slip between the bodies. The results were later extended by Karuppanan and Hills

[2007][61], where they applied the same approach to solve contact problems with trapezium-shaped punches. Flicek et al., [2015][62] quantified the finite extent of slip and separation occurring near the edge of complete contacts using wedge asymptotes. Qualitative implications were derived for larger slip and separation lengths.

Navarro et al., [2003][63] developed a solution for a sharp as well as flat and rounded square punches, subjected to monotonically increasing proportional shear force and bulk tension, with particular attention to effect of tension in stabilising the partial slip regime. They summarised the partial slip behaviour for the application of shearing force and bulk tension at various ratio's and further concluded that the presence of bulk tension enables a stable partial slip regime. Cartwright and Paynter [2011][64] investigated the problem of slip and wear using the wedge asymptotes and established necessary and sufficient condition for the avoidance of wear. A method to quantify the fretting fatigue damage arising at the edges of complete contacts subject to oscillating loading was presented by Hills et al., [2012][65]. Williams wedge analysis was used and the key feature was that the response can be predicted for any complex geometry. The solution permits the fatigue strength measured in a laboratory experiment to be used to predict reliably the behaviour of any engineering component. Juoksukangas et al., [2013][66] studied the effect of contact edge geometry on the fretting fatigue behaviour of complete contacts. Sharp and rounded square ended contact geometries were used. A 2-D elasto-plastic finite element contact model was created to calculate the fretting cracking risk for these geometries using the Findley multi-axial fatigue criterion. Results shows that the model with slightly in-complete contact edge is more prone to cracking than the sharp edges contact.

Hills *et al.,* [1996][67] described the concept of the distributed dislocation technique and since then it has been applied to solve partial slip contact problems in an asymptotic sense. Churchman and Hills [2006a][68] showed how this approach can be applied to compute the stress intensity factors for a crack arising at the edge of a three quarter plane. Churchman

and Hills [2005][20] then used this approach to quantify the extent of slip and also to define an inner slipping asymptote. Paynter and Hills [2010][69] obtained a solution for computing the slip and separation extent at the edge of complete contact using a semi-infinite wedge formulation. They accounted for the presence of slip and separation by making some changes to the Williams solution.

1.3.4 Frictional shakedown

If an engineering system consists of elastic contacts with frictional interfaces, then the instantaneous state generally depends on the previous loading history and the problem behaves in an inherently non-linear fashion. However, if the system is subjected to cyclic loading conditions, it would tend to move towards steady state response after a certain number of loading cycles (Banerjee and Hills [2006][70]) and the contact eventually *shakes down*. In the majority of the cases the number of cycles required to attain a steady state response is very small and therefore contacts generally spend most of their fatigue life in steady state operating conditions. Hence, practically, it would be interesting to investigate when a contact reaches a steady state response and, if it does, then to determine the ensuing frictional response of the contact for the subsequent loading cycles.

Frictional shakedown can be defined as the process where the contacts tend to move towards the steady state response, where favourable residual displacements formed during the first few cycles reduces or inhibit slip in the subsequent cycles. There are clear parallels between frictional slip and plastic flow in elasto-plastic solids. Both are dissipative mechanisms and depends on the loading history, but not on the rate of loading. This raises the question as to whether an approach similar to plasticity theorem formulated by Melan [1996][71] could be used for frictional contacts in order to predict shakedown. Shakedown studies on frictional contacts

have only begun recently and most of the research has been spent on analysing whether results from plasticity theory could be used to address frictional problems.

Churchman and Hills [2006][60] did some studies on this front and tried to apply this approach to predict shakedown in complete contacts subject to oscillatory shear loading. Klarbring et al., [2007][13] have proved, for two and three dimensional discrete systems, that Melan's theorem can be applied to frictional elastic systems with Coulomb friction contact conditions, if and only if there is *no coupling* between the tangential (slip) displacements and normal contact reactions. For such a case, a single load factor is sufficient to characterize the shakedown conditions. However for *coupled* systems, the attainment of final steady state response depends heavily on the initial displacement conditions and a range of load factors are required to determine the occurrence of shakedown. Primarily they identified a class of two-dimensional systems with a degeneracy in the stiffness matrix, for which the shakedown theorem could be established if the friction coefficient is less than a certain critical value. A similar result was established for continuum problems by Barber *et al.*, [2008][12]. Bjorkman and Klarbring [1987][72] have presented an approach for calculating the shakedown limit, which they formulated as a linear programming problem for which several efficient solution algorithms exist. Flicek et al., [2014][73] used the same programming approach and investigated the influence of initial displacement conditions on the magnitude of frictional dissipation present in the steady state. Several finite element simulations of transient contact problems were performed with various initial conditions to determine the shakedown limit and the results are compared with the corresponding results obtained by the numerical approach.

1.4 Summary of thesis

This thesis attempts to develop methods that accurately predict the frictional response of complete contacts as observed in blade to disc interface components viz., dovetail, fir-tree joints present in gas turbine engines. The work done in this thesis can be divided in to three parts. The first part of the work is based upon a purely numerical approach, where a computationally efficient numerical reduction method has been implemented as a plugin for a finite element code, in order to solve quasi-static frictional contact problems. The second part of the work mainly concerns partial slip in complete contacts, where asymptotic forms were applied to predict the stress state along the regions adjoining edges of blade/disc contact and female socket end. The third phase of work is focused on shakedown studies on a typical dovetail component used in blade root assembly, where we predict the occurrence of a self-wedging phenomenon at a characteristic coefficient of friction. A brief outline of this dissertation is given below.

Chapter 2 discusses how a semi-infinite formulation based on linear elastic fracture mechanics can be applied to solve complete contact problems with negligible finite width (between blade root tip and socket end) and evaluate the contact conditions near the edge. The crack-tip stress intensity factors K_I and K_{II} arising out of the root tip plays a pivotal role in computing the stress state locally and helps in the calculation of closure conditions and coefficient of friction for the edge considered. The predicted results are then compared with finite element results for the purpose of demonstration.

In chapter 3, a semi-infinite solution has been derived for the case where there is a finite width slot present between the edges of blade/disc contact and socket end. Influence of non-singular terms relevant to the T-stress component, on the solution of semi-infinite crack form is discussed. The displacement components concerning T-stress has been formulated and included in the semi-infinite Trench solution. The solution, comprising the stress intensities (K_I, K_{II})

and T-stress component σ_o, is then applied to finite example problems. Convergence studies of the notch intensities computed by the trench method are performed. The interfacial traction ratio computed by the trench method is eventually compared with the finite element results.

In chapter 4, response of the contacts with inclination $\pi/2$ and $3\pi/4$ radians has been considered. Asymptotic forms relevant to the geometries were applied and a qualitative study of results have been performed.

In chapter 5, the phenomenon of wedging behaviour in complete contacts has been addressed with particular reference to the blade root assemblies in an aero engine. The sensitivity of wedging behaviour was studied in terms of the coefficient of friction, internal contact angle and the material adjoining the contact region.

In chapter 6, a brief mathematical description of static reduction method is given. Then procedure to obtain the reduced stiffness matrix for representative contact problems (single body/two body contact) is discussed. The solution procedure for solving quasi-static frictional contact problems is given. The numerical solution obtained by Gauss-Seidel procedure is then discussed in an algorithmic setting. Static reduction method is applied to run several example numerical models and the numerical results are discussed. The behaviour of the plugin code is validated by a comparison of equivalent results with SC03 and ABAQUS contact solvers.

In chapter 7, concluding remarks from each of the above chapters are consolidated. Future course of work has been identified and recommendations provided for further enhancement of the work presented.

Chapter 2

The Semi-infinite crack problem & its application to closely fitted contact problems

2.1 Introduction

Conventionally it is not possible to obtain a general closed form solution for the contact tractions beneath complete contacts. But then, practically, this may not present a major concern, because when it occurs, slip in-variably starts from the edges of the contact. Observation points near these edges are generally not influenced or are only weakly influenced by the geometries or the loading conditions observed in the far region and therefore the stress state they suffer may be formulated using bonded semi-infinite wedge principles. The classical example is a half-plane in contact with a quarter plane, encapsulating the complete set up as a 270^o wedge problem as shown in Figure 2.1, assuming the displacements are continuous along the interface and the contacting bodies are elastically similar. The flexibility with this approach is that the

wedge angle is very much customizable and the semi-infinite form will work for any other angle that the contact edge assumes. The main idea, here, is to quantify the magnitude of stress intensification arising at the edges due to the application of external loads and to use that to compute the stress state adjoining the asymptotic region, which facilitates the prediction of closure conditions and coefficient of friction needed to keep the edge in an adhered condition.

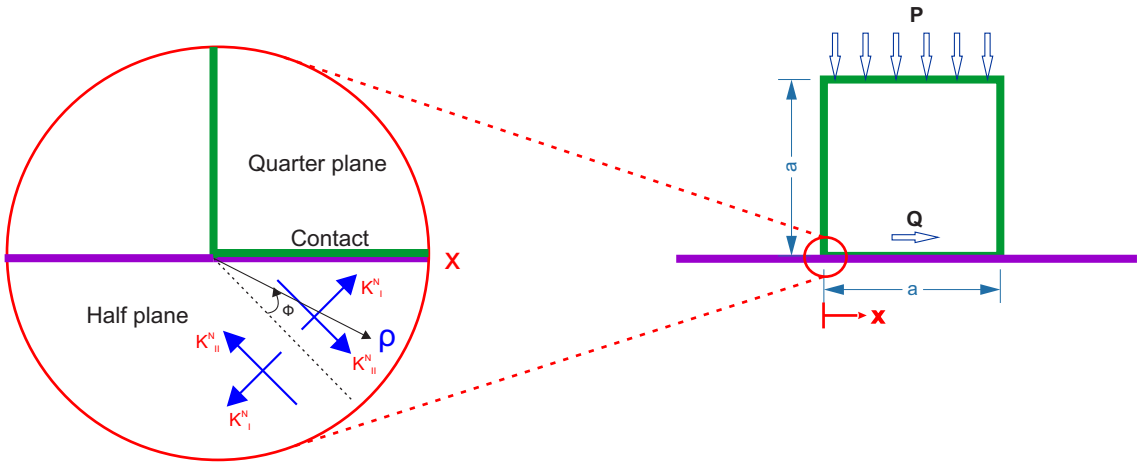


Figure 2.1: Semi-infinite description of a block in contact with a half-plane modelled as a 270^o wedge problem

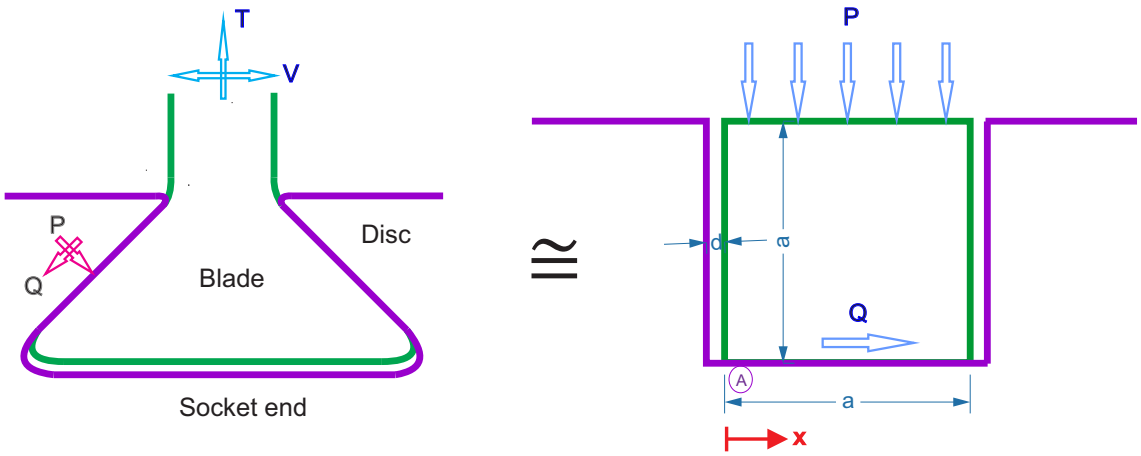
The presence of sharp edge adjoining the blade/disc interface produces stress intensification effects.

Very close to the edge of a blade root tip another component is present called a disc socket. We may idealise this so that it possess similar sharp features which will modify the contact edge state of stress. The stress concentration effects arising from these edges interact. Thus, the objective, here, is to design a wedge model which accurately represents the above-mentioned geometrical features and gives the relevant asymptotic forms to obtain a comprehensive solution for representative contact problems.

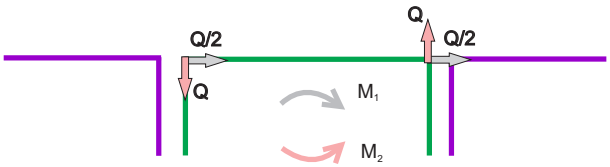
2.2 Description of problem set-up

As discussed previously in section 1.4, the contacts we intend to study are commonly observed in blade to disc interface components of dovetail, fir-tree assemblies present in gas turbine engines. For the initial phase of implementation, dovetail contact is considered and it has been idealised as a Trench geometry with a finite clearance adjacent to the edge of contact (refer Figure 2.2a). The following assumptions were done while idealising the contact geometry: (i) The contact edges are perfectly straight and sharp (ii) The internal angle of the dovetail approximated as a right angled contact (iii) The centrifugal loads and the engine vibrations are replaced by the normal and shear loads (applied statically along the interface). Before having a closer look at the particulars of idealised trench geometry, it is revealing to discuss the proposed semi-infinite geometry of the problem description given in an analogous way to that introduced in section 2.1.

Let us consider the classical case of a contact model where an elastic flat punch making contact with an elastically similar half-plane as shown in Figure 2.1. This kind of asymptotic form was conventionally used by the researchers in the past to model contact problems such as spline joints in shafts. The formulation for these models allows the flexibility of assuming that the wedge angle is equal to the internal angle found in an actual dovetail. However the disadvantage with this approach is that it does not consider the interaction between stress concentration effects occurring between the adjacent edges present in the region enclosing blade root tip and disc socket end. The proposed geometry representing the asymptotic form of the contact edge is shown in Figure 2.3, where a second wedge equivalent to a three-quarter plane makes contact with a quarter plane. This particular set up effectively models the geometry shown in Figure (2.2a). With this configuration, it includes the stress concentration effects from the socket end and therefore additionally includes the influence of the adjacent "wall" of



(a) Dovetail contact geometry and its idealised representation of an example finite model showing the finite clearance adjacent to the edge of contact



(b) Method of shear load application

Figure 2.2: Description of idealised finite contact model to represent the dovetail geometry with the following assumptions: (i) Edges are straight and sharp (ii) Internal angle taken to be $\pi/2$ radians

material.

From an analysis perspective, we are interested in obtaining the behaviour of contacts when the indenter is positioned at different length scales from the socket end. When the indenter is positioned at a distance remote from the socket, we are guaranteed to obtain a behaviour similar to the form shown in Figure 2.1, where the three-quarter plane solution is pertinent and a 270^o wedge solution applies. As the intender is brought closer to the socket end, the response changes due to the proximity of adjoining material and therefore needs an investigation of the resulting interaction between stress concentration effects.

The example problem we wish to study is shown in Figure 2.2a. It consists of a *square* block of size a pushed into a trench located in a elastically similar half-plane and forming slots on either side of the block. The depth of the trench is a and the width of the slot is d and

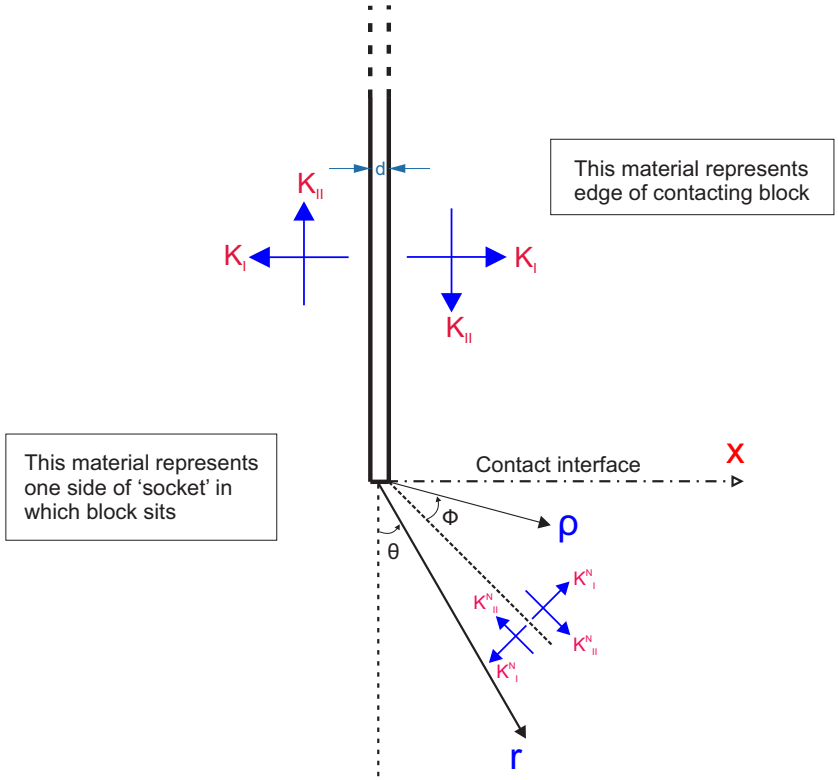


Figure 2.3: Semi-infinite description of a trench model with a finite separation adjacent to the contact

therefore the width of the trench itself is $a + 2d$, with the block being positioned centrally. The purpose of the slot is to simulate the effect of clearance between the blade root and the socket end of a practical geometry shown in Figure 2.2a. A normal load P is applied initially in order to establish contact. Then a shear force, Q is applied as concentrated loads on either ends of the block as shown in Figure 2.2b. This will, in-turn, produce a moment M_1 in the clockwise direction. So, in addition, vertical opposing forces are applied on the same nodes where the shear is applied, which creates an equal anti-clockwise moment M_2 and thereby balancing the moment induced earlier. This method enables the shear load to be applied in such a way as to make it statically equivalent to one passing through the interface with out the local imposition of external forces. Note that we focus our attention on the left hand side corner of the contact and predict the response for both positive and negative shear loads. Depending on the width of

the slot, we can categorise the problem differently and obtain an asymptotic solution employing different methodologies. As the width d is extremely negligible ($d \ll a$) or in other words as the clearance vanishes i.e., ($d \longrightarrow 0$), the narrow slit can be treated as a crack and a linear elastic fracture mechanics formulation can be applied to approximate the tractions close to the edge. For the other extreme case, where the width of the gap becomes very large i.e., ($d \gg a$), the edge region can be treated as a notch with an included angle of 270^o and William's solution for a wedge can be used to obtain the solution. Thus our overall intention in this context is to study the influence of material in the adjacent socket on the behaviour of contact and especially on the contact edge. If $d \ll a$ but is not negligible the form of a semi-infinite trench may help, which comprises of principles from semi-infinite wedge and crack formulations.

2.3 Introduction to linear elastic fracture mechanics

2.3.1 Motivation

The field of fracture mechanics gained momentum in the last two decades of the $20th$ century. Current research tends to result in incremental advances rather than major gain. The application of this technology to practical engineering problems is so persuasive that fracture mechanics is now considered an established engineering discipline.

The comparison of fracture mechanics approach and the traditional strength of materials approach to structural design and material selection is shown in Figure 2.4. A component is assumed to be structurally compliant if its strength is greater than the expected applied stress. Such an approach may attempt to guard against brittle fracture by imposing a factor of safety on stress. The fracture mechanics approach has three critical variables as compared to the two for the conventional strength approach. The additional structural variables flaw size and

fracture toughness replace yield strength as the relevant material property. Generally, the fracture mechanics approach intend to quantify the critical combinations of these three variables. There are two alternative approaches to fracture analysis, namely the energy criterion and the stress intensity approach. The energy approach states that crack propagation (i.e., fracture) occurs when the energy available for crack growth is sufficient to overcome the resistance of the material. The material resistance may include the surface energy, plastic work, or other types of energy dissipation associated with a propagating crack. The work carried out in this thesis is mainly focussed on the stress intensity approach, where we quantify the tractions using the stress intensifications arising at the "crack" tip region.

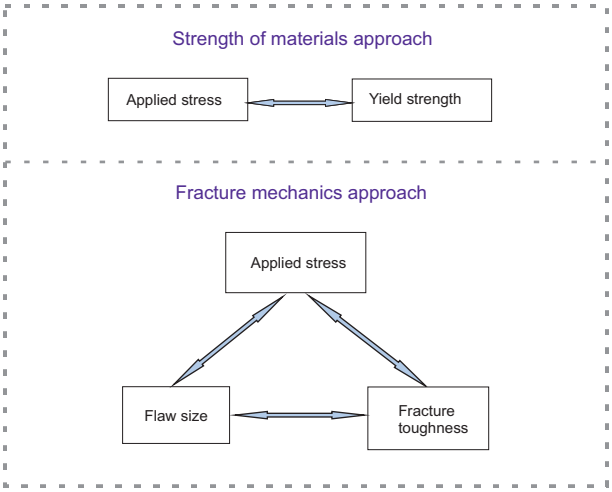


Figure 2.4: Comparison of Strength of materials/Fracture mechanics approach from a design perspective

The stress intensity approach

Figure 2.5 illustrates the schematic of a crack-tip in an elastic material, together with in-plane stresses on an element near the tip. The stress components arising near the crack-tip region are proportional to the single constant K_I. Once this constant is known, the entire stress distribution at the crack-tip can be computed. This constant is termed the stress intensity

factor, which quantifies the magnitude of stress intensification due to application of remote loads, and therefore characterizes the crack-tip conditions for a given linear elastic material. However it is to be noted here that the formulation is material dependent if the remote loads are applied through displacements. The alternate parameter K_{IC} called the critical stress intensity, is also termed the fracture toughness, and signifies the onset of fracture at a critical combination of stress and crack size. The stress intensity factor for an infinite body with a center crack of half length a is given below.

$$K_I = \sigma\sqrt{\pi a} \tag{2.1}$$

We could further state that fracture occurs at $K_I = K_{IC}$, where K_I is the driving force for fracture and K_{IC} is the measure of material resistance.

2.3.2 Linear elastic crack tip field

For certain cracked configurations subjected to external loads, it is possible to derive closed form expressions for the stresses in the body, assuming isotropic linear elastic material behaviour. Westergaard, Irwin, Sneddon, and Williams were among the first to publish such solutions. The key simplifying feature here is that the crack-tip in an un-stressed state is perfectly sharp and the crack faces remain traction free at all stages of loading. Assuming a polar coordinate system and the origin being centred on the tip, the crack-tip stress field in any linear elastic cracked body is given by Anderson [2005][74]

$$\sigma_{ij} = \left(\frac{k}{\sqrt{r}}\right) f_{ij}(\theta) + \sum_{m=0}^{\infty} A_m r^{\frac{m}{2}} g_{ij}^{m}(\theta) \tag{2.2}$$

Where,

σ_{ij} = Stress components

r,θ = radial and tangential coordinates

k = proportional constant

f_{ij} = Angular distribution of stresses

A_m represents the magnitude of the higher order terms and g_{ij}^m is a dimensionless term that signifies the angular distribution of stresses relevant to the m^{th} term. The importance of the higher order terms depend very much on the geometry and remote boundary conditions. The solution sequence for the leading terms usually exhibits a square root singular behaviour, i.e., the crack tip stresses are proportional to $1/\sqrt{r}$. Therefore, as we approach the root tip, the leading terms go to infinity and the rest of the terms either gives a finite value or may become negligible. Having said that, the leading terms nevertheless exhibits a geometry dependency through the parameter k and shows a $1/\sqrt{r}$ dependency, while the crack-tip displacements varies with $\sqrt{r}$. Thus Equation 2.2 can be termed as stress singularity in the context that the stresses are asymptotical at $r = 0$.

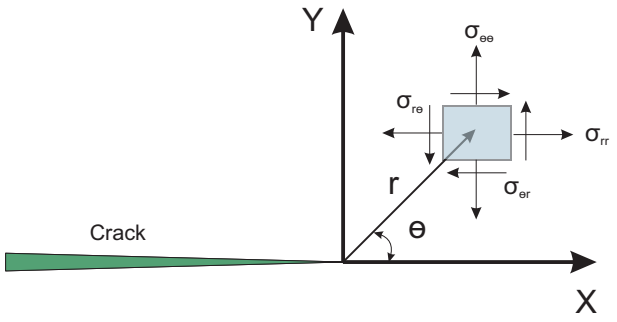
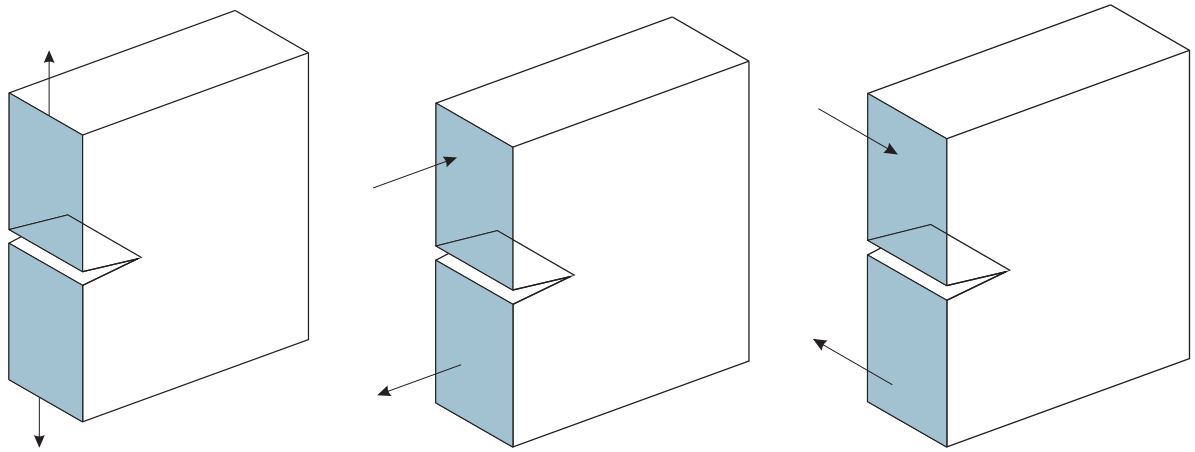


Figure 2.5: Crack tip stress field in an elastic material

Generally the crack-tip can be subjected to three standard modes of loading as shown in

Figure 2.6. The mode I loading is the most common type of loading, where the load is applied normal to the crack plane and opens up the crack. The mode II loading refers to in-plane shear loading, which tend to slide one crack face on the other. Mode III loading produces an out of plane shear, creating a twisting effect between the crack faces.



(a) Mode I **(b)** Mode II **(c)** Mode III

Figure 2.6: General modes of fracture: (a) Loads applied normal to crack plane (b) In-plane shear loading (c) Out-of plane shear loading

It is to be noted here that the proportionality constants k and f_{ij} depends on the mode of the loading. The term "k" is the multiplier used to collocate the outer tip solution in to the finite body. The latter term f_{ij} is the internal eigen vector and is a function of the spatial coordinates about the tip, representing the stress distribution of the field. We can now represent k in terms of *stress intensity factor* K, where $K = k\sqrt{2\pi}$. The crack tip stress field for an

isotropic linear elastic material can be defined for individual modes as follows

$$\sigma_{ij}^{I} = \lim_{r\to 0} \frac{K_I}{\sqrt{2\pi r}} f_{ij}^{I}(\theta), \tag{2.3a}$$

$$\sigma_{ij}^{II} = \lim_{r\to 0} \frac{K_{II}}{\sqrt{2\pi r}} f_{ij}^{II}(\theta), \tag{2.3b}$$

$$\sigma_{ij}^{III} = \lim_{r\to 0} \frac{K_{III}}{\sqrt{2\pi r}} f_{ij}^{III}(\theta). \tag{2.3c}$$

For a mixed mode problem, the total stress component can be interpreted as an addition of individual stress contributions from each mode, as defined by the principle of superposition.

$$\sigma_{ij}^{total} = \sigma_{ij}^{I} + \sigma_{ij}^{II} + \sigma_{ij}^{III} \tag{2.4}$$

The analytical expressions describing the singular state of stress and displacements near the crack tip for mode I and mode II loading are follows.

Mode I:

$$\begin{Bmatrix} \sigma_{rr} \\ \sigma_{\theta\theta} \\ \sigma_{r\theta} \end{Bmatrix} = \frac{K_I}{\sqrt{2\pi r}} \begin{Bmatrix} \cos\left(\frac{\theta}{2}\right)\left[1+\sin^2\left(\frac{\theta}{2}\right)\right] \\ \cos^3\left(\frac{\theta}{2}\right) \\ \sin\left(\frac{\theta}{2}\right)\cos^2\left(\frac{\theta}{2}\right) \end{Bmatrix}, \tag{2.5}$$

$$\begin{Bmatrix} u_r \\ u_\theta \end{Bmatrix} = \frac{K_I}{2E}\sqrt{\frac{r}{2\pi}} \begin{Bmatrix} (1+\upsilon)\left[(2\kappa-1)\cos\left(\frac{\theta}{2}\right) - \cos\left(\frac{3\theta}{2}\right)\right] \\ (1+\upsilon)\left[-(2\kappa+1)\sin\left(\frac{\theta}{2}\right) + \sin\left(\frac{3\theta}{2}\right)\right] \end{Bmatrix}, \tag{2.6}$$

Mode II:

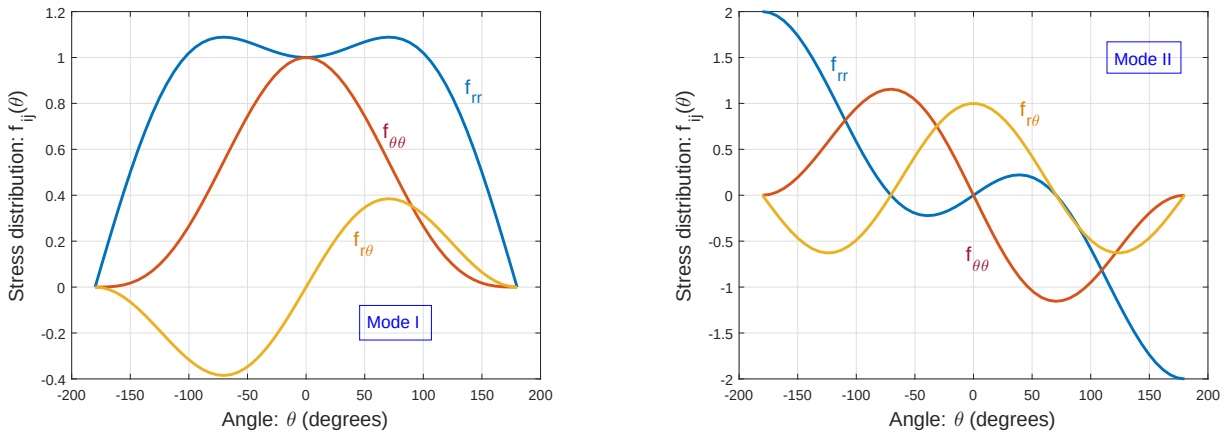
$$\begin{Bmatrix} \sigma_{rr} \\ \sigma_{\theta\theta} \\ \sigma_{r\theta} \end{Bmatrix} = \frac{K_{II}}{\sqrt{2\pi r}} \begin{Bmatrix} \sin\left(\frac{\theta}{2}\right)\left[1-3\sin^2\left(\frac{\theta}{2}\right)\right] \\ -3\sin\left(\frac{\theta}{2}\right)\cos^2\left(\frac{\theta}{2}\right) \\ \cos\left(\frac{\theta}{2}\right)\left[1-3\sin^2\left(\frac{\theta}{2}\right)\right] \end{Bmatrix}, \tag{2.7}$$

$$\begin{Bmatrix} u_r \\ u_\theta \end{Bmatrix} = \frac{K_{II}}{2E}\sqrt{\frac{r}{2\pi}} \begin{Bmatrix} (1+\upsilon)\left[-(2\kappa-1)\sin\left(\frac{\theta}{2}\right)+3\sin\left(\frac{3\theta}{2}\right)\right] \\ (1+\upsilon)\left[-(2\kappa+1)\cos\left(\frac{\theta}{2}\right)+3\cos\left(\frac{3\theta}{2}\right)\right] \end{Bmatrix}, \tag{2.8}$$

where $E \longrightarrow$ Young's modulus, $\upsilon \longrightarrow$ Poisson's ratio and $\kappa \longrightarrow$ Kolsov's constant ($\kappa = 3-4\upsilon$). The spatial variation of the distribution function f_{ij} is shown in Figure 2.7. The stress intensity factors K_I and K_{II} represents the magnitude of the stress singularity at the tip region due to applied loads. The crack-tip stresses defined in Equations 2.5 and 2.7 increase in proportion to the stress intensities. Therefore if the crack tip stress intensities are known, then it is possible to compute the components of stress, strain and displacement as a function of the spatial coordinates r and θ. Thus, it can be concluded that the single parameter description of crack tip conditions proves to be one of the most important concepts in fracture mechanics.

2.4 Governing asymptotic formulation and its application to representative contact problems

This section discuss mainly to the application of linear elastic fracture mechanics formulation (refer Section 2.3.2) to contact problems where the side clearance d becomes extremely small. A finite example problem of a block resting in a closely fitted trench is chosen for this purpose (refer Figure 2.2a). The formulation is then applied subsequently to derive the contact edge



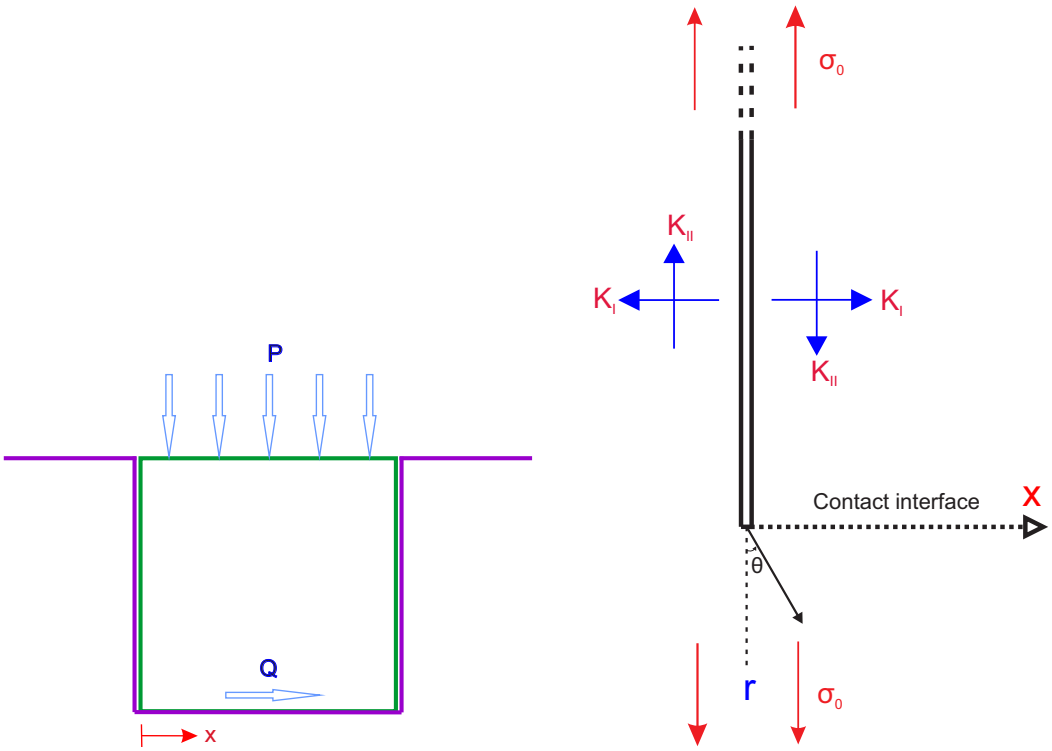
(a) Mode I distribution **(b)** Mode II distribution

Figure 2.7: Angular distribution of crack-tip stresses, representing the variation of eigen-vectors f_{rr}, $f_{\theta\theta}$ and $f_{r\theta}$ for various angles $[-200^o : 200^o]$ in the tangential direction

conditions namely the intimate contact (finite contact pressure) and minimum coefficient of friction needed for adhesion. An introduction to non-singular terms in the series expansion of the crack-tip stress state, so called T-stress ($m = 0$, Equation 2.2) is provided and its influence in the overall response of the contact with respect to certain loading conditions is discussed. An elaborate discussion of the impact of T-stress on the contact and the derivation of relevant displacement components is carried out in Chapter §3. For the purpose of demonstration, finite element results were computed alongside the analytical results and a quantitative comparison has been done.

2.4.1 Formulation for the block resting in a closely fitted trench

The contact we intend to solve is re-shown in Figure 2.8a, where the finite width d between the edge of the block and the trench wall is very small indeed, so that the ratio $d/a \to 0$. Under these conditions the side clearance is extremely narrow and resembles a crack. This enables us to apply the formulation based on a semi-infinite crack (as shown in Figure 2.8b), which forms



(a) Finite description of crack model at small d/a ratio

(b) Semi-infinite description of crack model

Figure 2.8: Realisation as crack model when the ratio $d/a \to 0$

the basis of fracture mechanics and which is subject to mode I and mode II loading, with the conventional nomenclature, and these quantities represent respectively the stress intensity factors scaling the opening and shear mode solutions, applied to the crack-tip. The crack-tip fields for this problem are very well known. A very simple and clear set of solutions for mode I and mode II loading of the crack-tip is defined in Lawn and Wilshaw [1975][75] and are given in Equations 2.5-2.8. As can be seen from Figure 2.8b, the sector defining the contact interface is located at an angle $\frac{\pi}{2}$ from the crack bisector for the left hand side crack and therefore the normal and shear stress components along this interface can be defined as follows for the case of mode I and mode II loadings.

Mode I:

$$\sigma_{\theta\theta} = \frac{K_I}{\sqrt{2\pi r}} \cos^3\left(\frac{\pi}{4}\right) \tag{2.9a}$$

$$\sigma_{r\theta} = \frac{K_I}{\sqrt{2\pi r}} \sin\left(\frac{\pi}{4}\right) \cos^2\left(\frac{\pi}{4}\right) \tag{2.9b}$$

The simplified version of Equation 2.9 can be represented as follows:

$$4\sqrt{\pi r}\sigma_{\theta\theta} = K_I \tag{2.10a}$$

$$4\sqrt{\pi r}\sigma_{r\theta} = K_I \tag{2.10b}$$

Mode II:

$$\sigma_{\theta\theta} = \frac{K_{II}}{\sqrt{2\pi r}} \left[-3 \sin\left(\frac{\pi}{4}\right) \cos^2\left(\frac{\pi}{4}\right)\right] \tag{2.11a}$$

$$\sigma_{r\theta} = \frac{K_{II}}{\sqrt{2\pi r}} \cos\left(\frac{\pi}{4}\right) \left[1 - 3\sin^2\left(\frac{\pi}{4}\right)\right] \tag{2.11b}$$

$$4\sqrt{\pi r}\sigma_{\theta\theta} = -3K_{II} \tag{2.12a}$$

$$4\sqrt{\pi r}\sigma_{r\theta} = -K_{II}. \tag{2.12b}$$

The total stresses adjacent to the crack tip can then be obtained as a summation of Equations

2.10 and 2.12 and given as follows.

$$4\sigma_{\theta\theta}\sqrt{\pi r} = K_I - 3K_{II} \tag{2.13a}$$

$$4\sigma_{r\theta}\sqrt{\pi r} = K_I - K_{II}. \tag{2.13b}$$

Calculation of closure conditions and friction requirements

The normal tractions $\sigma_{\theta\theta}$ along the interface obtained in Equation 2.13a, may be used to predict the state of opening or closure of the edge of contact. The ratio of tangential to normal tractions $\frac{\sigma_{r\theta}}{\sigma_{\theta\theta}}$ as obtained from Equations 2.13a and 2.13b enables computation of minimum coefficient of friction needed for ensuring stick conditions. The requirement that the contact remains closed is that the normal traction $\sigma_{\theta\theta}$ must be compressive i.e., $\sigma_{\theta\theta} < 0$. Applying this convention in Equation 2.13a reveals the following condition for closure of the contact.

$$K_{II}/K_I > \frac{1}{3} \tag{2.14}$$

Note that the above criterion has been derived without taking into account the signs of the individual stress intensity factors. A rigorous method would be to include the signs of K_I and K_{II}, before we compute the state of opening or closing of contact. An accurate representation of the closure conditions, with due attention to these sign conventions can be summarised as follows.

$$K_{II}/K_I > \frac{1}{3} \;\; \forall \;\; K_I > 0, K_{II} > 0 \tag{2.15a}$$

$$K_{II}/K_I < \frac{1}{3} \;\; \forall \;\; K_I < 0, K_{II} > 0 \tag{2.15b}$$

The traction ratio defined along the contact interface located at an angle $\frac{\pi}{2}$ from the crack

bisector is computed from Equation 2.13 and given as follows.

$$\frac{\left|\sigma_{r\theta}(\theta=\frac{\pi}{2})\right|}{-\sigma_{\theta\theta}(\theta=\frac{\pi}{2})}=\frac{\left|1-\frac{K_{II}}{K_I}\right|}{3\frac{K_{II}}{K_I}-1}. \tag{2.16}$$

The condition that the edge of contact remains in an adhered condition is that the coefficient of friction satisfies the inequality,

$$f>\frac{\left|1-\frac{K_{II}}{K_I}\right|}{3\frac{K_{II}}{K_I}-1}. \tag{2.17}$$

Analysis of crack-tip loading

We expect the crack-tip loading to be unusual in this case, as the crack-plane here is located parallel to the application of normal load. When this combination occurs, the conventional crack-tip stress intensity K_I may become negligible and the non-singular terms in the solution series may assume much greater significance in the stress state adjoining the crack-tip region. This becomes much clearer when we look at the loading condition shown in Figure 2.9 for the finite geometry considered. We focus our attention on the left hand side edge of the contact. Here we have maintained the depth of the block but made it infinitely wide and applied a normal load P_0 distributed over the right-hand half line of the upper surface of the block. By the principle of superposition, this condition can be split up in to symmetric and anti-symmetric components of loading as shown in Figure 2.9b,c. It is clear from Figure 2.9b that, the anti-symmetric loading excites a pure mode II condition but does not produce any mode I loading. While the symmetric loading on the other hand, generates the constant stress component $\sigma_{yy}=P_0$, everywhere along the crack plane and hence creates no stress intensification. The symmetric loading shown in Figure 2.9c contributes to the presence of

additional stress components in the form of 'T-stress'. This arises as a result of the influence of non-singular terms in the solution series expansion of the stress state at the crack-tip. As a consequence, the singular terms in the solution sequence may be expected to dominate the crack response at much restricted length scales, than is usually the case with conventional crack problems. Therefore, in addition to the conventional stress intensities K_I and K_{II}, the parameter σ_0 defining the intensification from T-stress need to be quantified at first, before we contemplate applying the same to characterize loading conditions for a realistic contact model. An elaborate discussion on the origin of T-stress and formulation for its displacement components are done in Chapter §3.

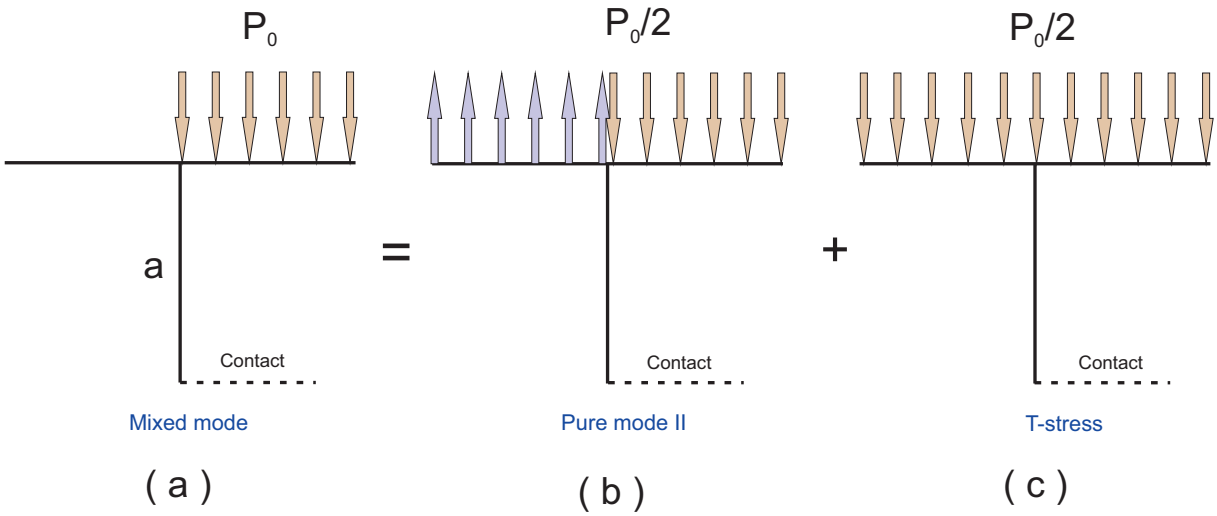


Figure 2.9: Interpretation of contact response near LHS edge subject to normal loads. Case(a): Actual loading condition which produces Mode II and T-stress components, Case(b): Anti-symmetric loading condition with pure mode II behaviour, Case(c): Symmetric loading condition that generates T-stress alone

2.4.2 Application to finite example contact problem

Applying the semi-infinite crack formulation and the contact criteria we have defined in Section 2.4.1, we can solve for the edge behaviour of representative contact problems of the type shown

in Figure 2.8a. In order to do this, first we have to compute the crack-tip stress intensities K_I, K_{II} and the T-stress component σ_0 for this model using a semi-analytical approach. It essentially requires the calculation of normal and shear tractions ($\sigma_{\theta\theta}$ and $\sigma_{r\theta}$) along the crack bisector region using a standard elastic finite element analysis of the model. These tractions when factored by $\sqrt{2\pi r}$ would reveal the stress intensities K_I and K_{II} arising at the edge. We maintain the assumption that the block/Trench interface is closed everywhere and fully adhered, so that the block together with the trench and half-plane can be modelled as a monolith in the finite element program.

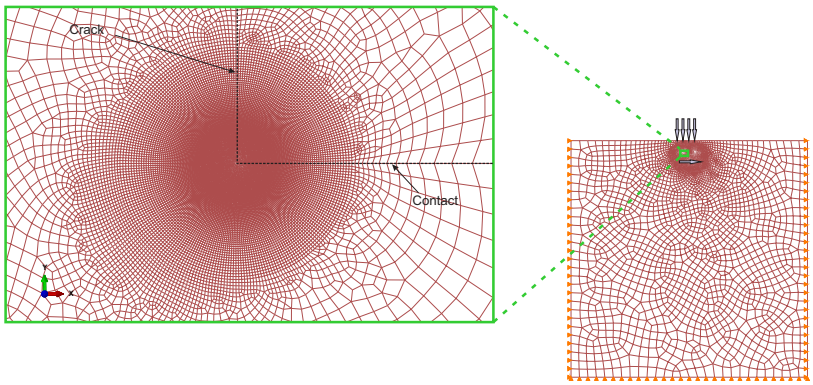


Figure 2.10: Mesh representation of the crack-tip region of finite crack model

The crack can be modelled as a quasi-static problem and solved using the ABAQUS contour integral estimates. A crack in a two-dimensional model can be idealised as a region containing edges that are free to move apart. The straightforward approach to perform a contour integral analysis involves creating the edges physically, which are assumed free to move apart as the crack separates. Here, in our approach, we have modelled the crack as a line embedded in a two-dimensional face called a "seam" (refer Figure 2.11) and performed contour integral analysis. Before starting the analysis, the crack front, crack-tip and crack propagation direction need to be selected in order to compute the estimates of stress intensity factors. When the model is meshed, overlapping nodes are created on the crack walls and these coincident nodes are free to

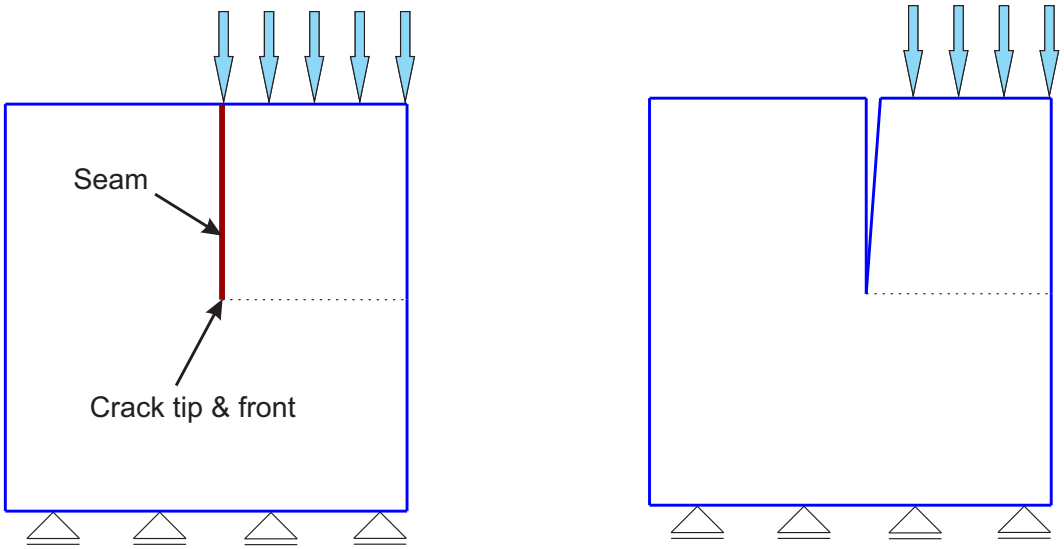
move apart as the crack separates. This implies that we do not include the possibility of contact between the crack edges and allow them to interpenetrate, upon loading in the opposite sense. The crack-tip singularity $(1/\sqrt{r})$ can be enforced by collapsing and moving the side nodes on the crack plane so as to create the necessary stress state adjoining the crack-tip region. A finely graded uniform mesh has been generated around the crack-tip (Figure 2.10) region to ensure a constant stress gradient across each element and thereby ensuring a better convergence of stress intensity parameters. The crack-tip stress intensities K_I, K_{II} and T-stress σ_0 are calculated using the tractions obtained along the crack bisector ($\theta = 0$) and are defined as follows.

$$K_I = \lim_{r\to 0} \sigma_{\theta\theta}(r,0)\sqrt{2\pi r} \tag{2.18a}$$

$$K_{II} = \lim_{r\to 0} \sigma_{r\theta}(r,0)\sqrt{2\pi r} \tag{2.18b}$$

$$\sigma_0 = \lim_{r\to 0} (\sigma_{rr}(r,0) - \sigma_{\theta\theta}(r,0)) \tag{2.18c}$$

To obtain converged stress intensity parameters, the quantities $\sigma_{\theta\theta}(r,0)\sqrt{2\pi r}$, $\sigma_{r\theta}(r,0)\sqrt{2\pi r}$ and $(\sigma_{rr}(r,0) - \sigma_{\theta\theta}(r,0))$ need to be plotted against the radial coordinates of the bisector as shown in Figure 2.12. Care should be taken to ensure that the quantities are measured at a distance very close to the crack tip region ($r \to 0$) and that the curve tends to stabilise or flatten out without fluctuations. Generally, it is advisable to skip the parameters measured at first few nodes, since the finite element results may not exactly capture the crack-tip singularity and therefore the results may not be accurate near this region. To ensure the correctness of the stress intensities, the semi-analytically obtained values are compared with the ABAQUS computed contour integral values for representative external loads and are shown in Figure 2.12d. The results matched very closely for mode II stress intensities. However differences were observed for mode I stress intensities with a maximum error tolerance of up to 5%. The error has been calculated as a fraction of the relative error between the two cases to that of the values



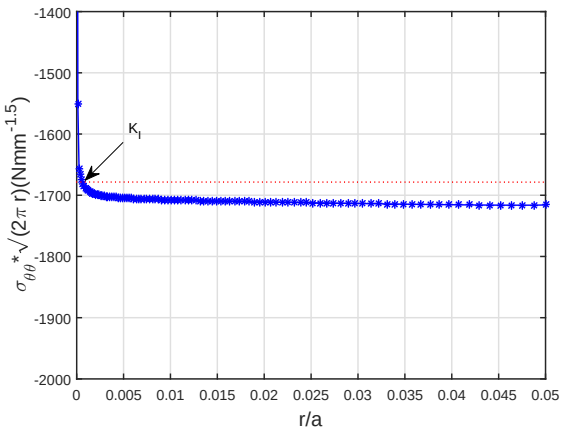
(a) Unloaded configuration (b) Loaded configuration

Figure 2.11: Finite Element modelling of crack using ABAQUS contour integral analysis

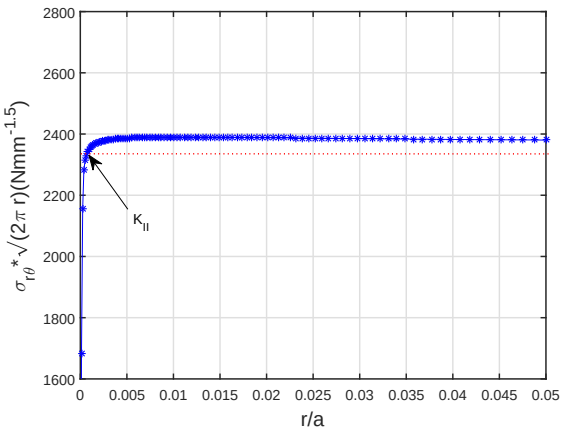
obtained by the semi-analytical method. The finite element calculation reveals the following calibrations for the stress intensity factors.

$$\begin{Bmatrix} \frac{K_I}{\sqrt{2\pi a}} \\ \frac{K_{II}}{\sqrt{2\pi a}} \\ \sigma_0 \end{Bmatrix} = \begin{bmatrix} -0.0974 & 0.3686 \\ 0.1441 & -0.0307 \\ -0.347 & -0.009 \end{bmatrix} \begin{Bmatrix} \frac{P}{a} \\ \frac{Q}{a} \end{Bmatrix}. \tag{2.19}$$

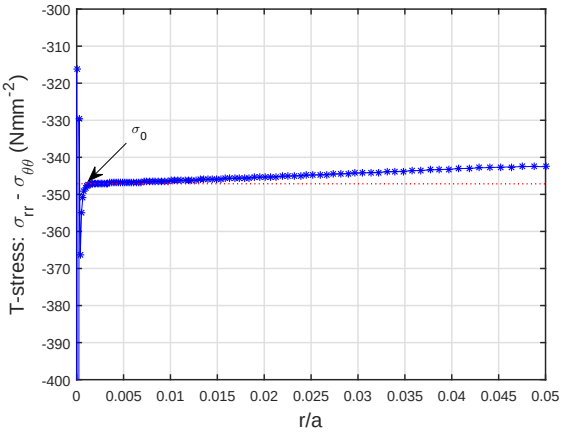
Figure 2.13 represents the predictions of separation and closure of contact for the left hand side crack in K_I-K_{II} space from the perspective of semi-infinite and finite descriptions. The key idea behind the plot is to show visually the variation of the stress intensities (in the form of vectors) for the range of loading sequence (Q/P's) considered until a separation of the edge is achieved. As can be seen from the plot, the closure condition varies depending on the signs of K_I and K_{II} in all the four quadrants. The first two quadrants where $K_I > 0, K_{II} > 0$ and $K_I < 0, K_{II} > 0$ represent the contact in a closed condition, whereas the remaining quadrants



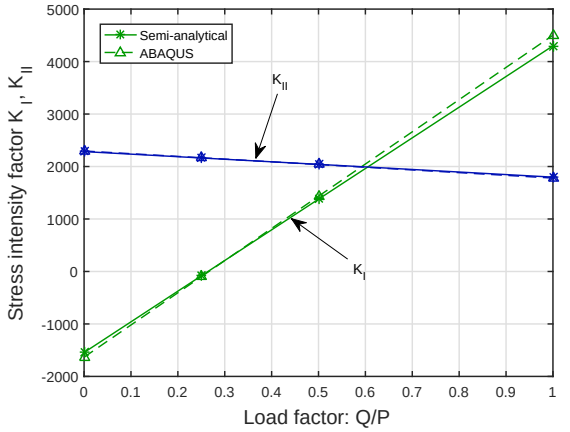
(a) K_I convergence



(b) K_{II} convergence



(c) σ_0 convergence



(d) Comparison of stress intensity factors calculated by the conventional semi-analytical method and ABAQUS contour integral analysis

Figure 2.12: Semi-analytical calculation of stress intensity parameters K_I, K_{II} and σ_0 for an example case where P alone was applied. The converged stress intensity parameters can be read as $K_I = -1656.6 Nmm^{-1.5}$, $K_{II} = 2284.6 Nmm^{-1.5}$ and $\sigma_0 = -346.99 Nmm^{-2}$

imply opening. Within the region of closure, the possibility of slip happening for characteristic coefficients of friction in the range $f = 0.3$ - 0.8 is given through the region enclosed by the gradients computed for the respective coefficients.

Further to the closure conditions given in Equation 2.15, we can compute, for the geometry

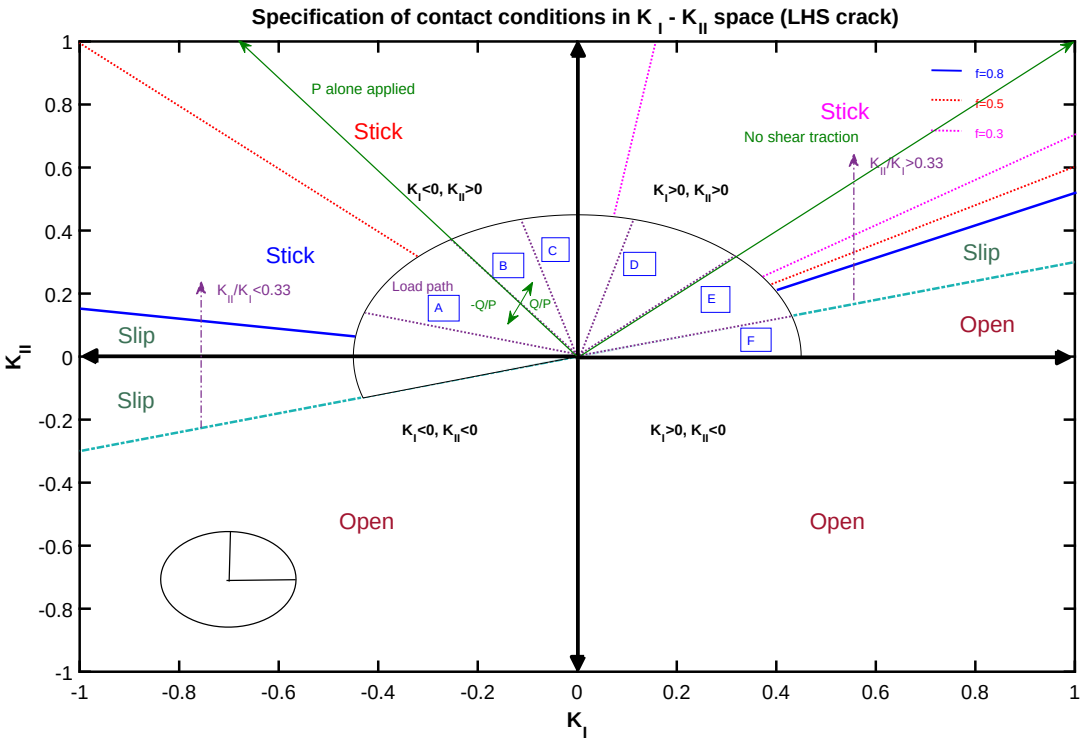


Figure 2.13: Specifications of contact conditions for LHS crack to illustrate the occurrence of separation and slip. The region outside the ellipse correlates the behaviour from a semi-infinite perspective, while that inside the ellipse tracks the response for the finite model portrayed in Figure 2.8a. The load paths $A - F$ corresponds to the response obtained at concerned $Q/P's$ referred from Figure 2.14

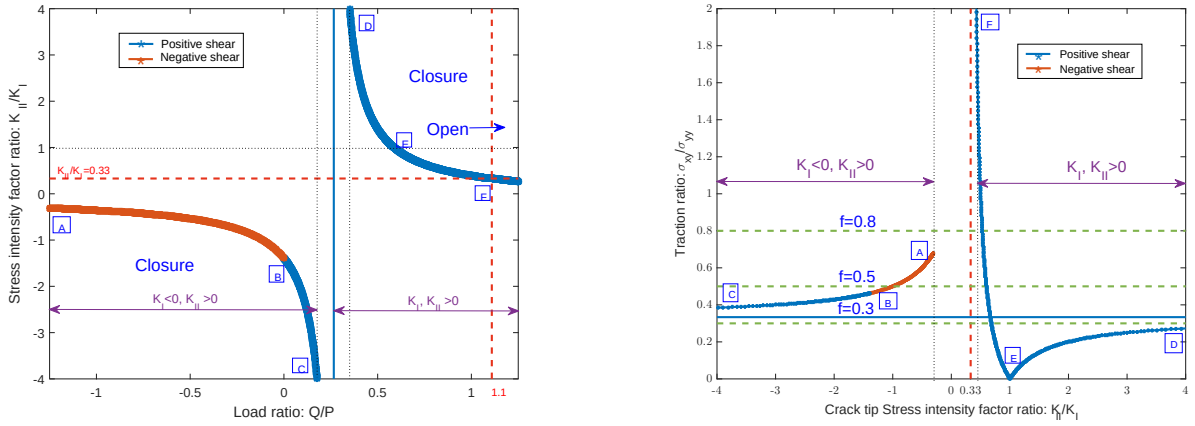
considered in Figure 2.8a, the condition for no separation in terms of the applied external loads as,

$$\frac{Q}{P} < 1.16. \tag{2.20}$$

For practical considerations, the ratio $|Q|/P \lesssim 1$ and that our initial assumption suggests that the contact is in fully adhered condition. This implies that for practical coefficient of frictions within unity, there will always be intimately adhered condition without any separation.

In order to infer the contact response from the plot, the gradient K_{II}/K_I needs to be computed first. The vector that defines the gradient inside the inner ellipse shows the edge behaviour when the load factor Q/P is varied nearly between -1 and 1, while that in the outer

region defines the conditions for closure and stick/slip criteria, as derived from the semi-infinite crack formulation.



(a) Response of stress intensity factors at various external loads

(b) Traction ratio behaviour at various stress intensity factors

Figure 2.14: Response of stress intensity factors and traction ratio for application of normal load P and shear load Q

When a normal load P alone is applied, the stress intensities $K_I < 0$ and $K_{II} > 0$ and the vector can be identified in the second quadrant. At this particular instance it creates a stress-intensity ratio $K_{II}/K_I = -1.48$. From equation 2.17 we compute that for this load, the minimum coefficient of friction needed to ensure stick condition is 0.46. When a positive shear is applied, the coefficient of friction needed decreases and the vector continues to move in the clockwise direction. With prolonged application, the stress intensities K_I and K_{II} become positive and the gradient vector now enters the first quadrant. When the ratio K_{II}/K_I reaches unity, the shear traction vanishes completely and this suggests that an infinitesimal amount of coefficient of friction is needed to maintain stick. A further increase in shear load Q causes the vector to rotate in the same direction and induces reverse slip for the maximum coefficient of friction considered ($f = 0.8$). When the shear is increased further, the coefficient of friction required to stick grows tremendously high, becoming asymptotically infinite as separation is

approached at a load ratio of $Q/P = 1.16$.

Conversely, when a negative shear is applied, the vector moves in the anti-clockwise direction and the traction ratio increases. The contact seems to be in a closed condition and the minimum coefficient of friction needed for stick is less than 0.8, until the loading vector reaches its practical limit of $Q/P = -1$. Figure (2.14a,2.14b) shows, for various applied loads (Q/P), the response of stress intensity factors and traction ratio computed for the left hand side tip, with specific reference to the example load vectors shown inside the ellipse. In terms of the applied loads, the condition for edge stick can be represented as follows.

$$f > \frac{1 - \left(\dfrac{1 - 0.21\dfrac{Q}{P}}{-0.676 + 2.56\dfrac{Q}{P}} \right)}{-1 + 3\left(\dfrac{1 - 0.21\dfrac{Q}{P}}{-0.676 + 2.56\dfrac{Q}{P}} \right)}. \tag{2.21}$$

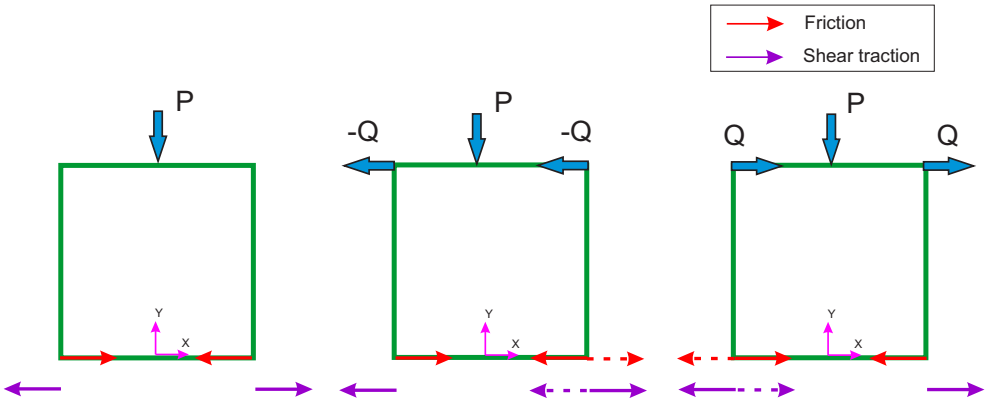


Figure 2.15: Free body representation of contact tractions for a finite true crack model

The coefficient of friction required for the left hand side edge to remain in an adhered condition for various external loads is shown in Figure 2.16. Figure 2.18 represents the finite element results for the normal and shear tractions computed along the whole of contact interface

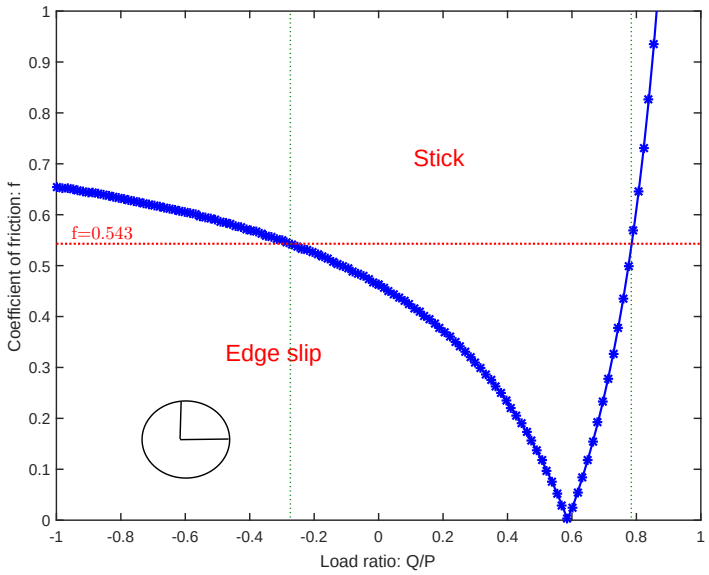


Figure 2.16: Analytical prediction of coefficient of friction at various load factors for the case $d/a = 0$ and Internal angle $\pi/2$ radians

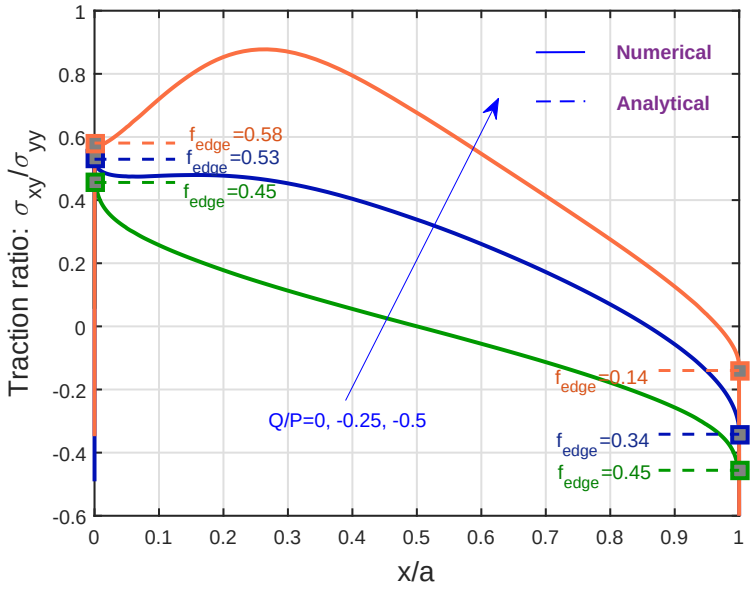
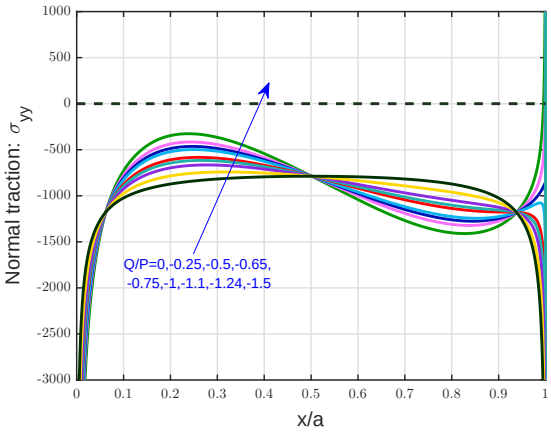


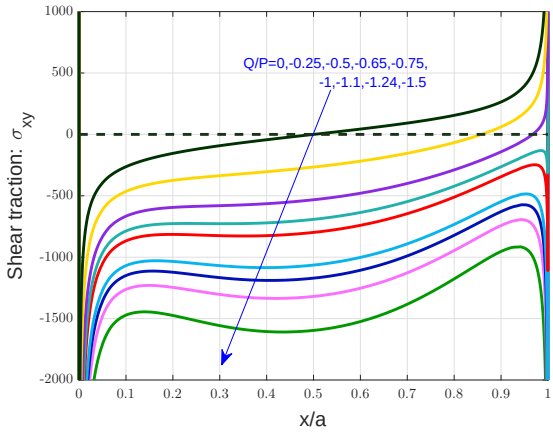
Figure 2.17: Comparison of edge traction ratio computed by the semi-infinite crack asymptotes against the numerical results for a true crack model with $d/a \to 0$

for various load factors. A free body representation of the contact kinematics is given in Figure 2.15 to show the direction vectors of friction and shear tractions for the application of normal and shear loads. As stated earlier, for a purely normal load, the coefficient of friction required to maintain the stick condition is 0.46. At this instant, the block tends to spread and the friction acts inwards on the block and the shear traction is directed towards the negative direction as evidenced in Figures 2.15 and 2.18b. When the shear force is applied in the negative direction i.e, towards the left, the coefficient of friction required for adhesion increases due to the implied increase in shear traction (Figure 2.16). The direction of shear traction nevertheless remains constant until the practical limit of the load ratio $Q/P = -1$. Figure 2.18b shows that for all negative shear loads, the shear traction is directed in the negative direction for the left hand side edge. When the shear force is applied towards the right, the friction continues to act inwards and the shear traction decreases gradually and vanishes at a load ratio $Q/P = 0.58$. A further increase in shear force in the same sense causes a reversal of the shear traction, and so friction acts outwards on the block (shown by dashed vectors in Figure 2.15). The shear traction continues to increase rapidly in the positive direction. The finite element calculation predicts similar results, where the sign reversal of shear traction happens between the load factors 0.5 and 0.65 (Figure 2.18d), which nearly coincides with the analytical prediction discussed above. From Figure 2.18c we see that the normal traction turns tensile at a load factor between 1.1 and 1.24, signifying the onset of separation. This can be matched with the analytical prediction for no separation as given in Equation 2.20.

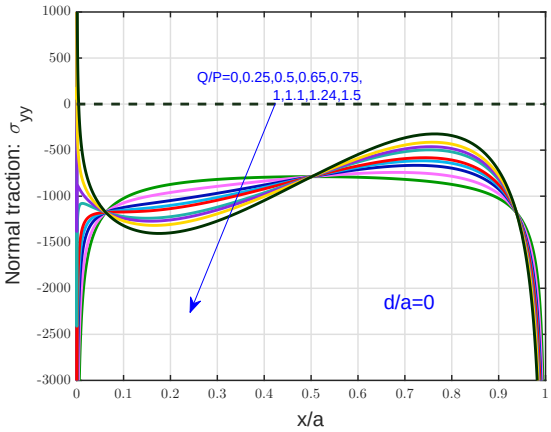
A further demonstration of the validity of the results can be shown in the form of matching the traction ratios along the full length of the interface with the analytical values computed for the edge. We see from Figure 2.17 that for $|Q|/P \lesssim 0.25$, the edge traction ratio $|\sigma_{xy}|/-\sigma_{yy}$ exceeds the traction ratio values computed for the interior section. This clearly suggests that coefficient of friction required for the edge is sufficient to ensure full stick conditions for the



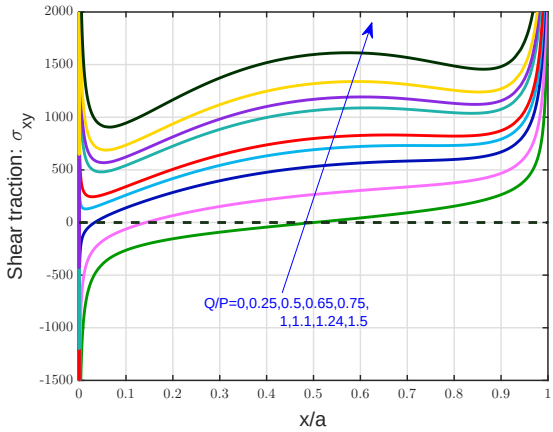
(a) Normal traction response at negative shear loads



(b) Shear traction response at negative shear loads



(c) Normal traction response at positive shear loads



(d) Shear traction response at positive shear loads

Figure 2.18: Traction behaviour along contact interface for various external loads for the case $d/a = 0$ and Internal angle $\pi/2$ radians

full length of interface. Note that we truncate the plot at $q(x)/p(x) \leq 1$, as there would be guaranteed slip at higher ratios. With further shear ($|Q|/P \gtrsim 0.25$), the interior traction ratio starts to increase and exceeds the value computed for edge region and this suggests that in case of any slip, it originates from the interior rather than the edge. From Figure 2.17 we see that the analytical traction ratios computed for both left and right hand side edges matched

with the finite element calculations with reasonably good accuracy. The results we have shown here are a good demonstration of how a contact problem controlled by the eigen-solution can be used to infer, in a very simple and general form, the condition for adhesion and intimate contact. A key aspect of the solution is that mode I and mode II eigen-solutions have the same strength of singularity and exert equal influence on the contact behaviour.

2.5 Conclusion

A general form of complete contact has been considered along with the presence of adjacent material near to the edge of contact and separated by a very small but finite clearance. Exploiting half-plane assumptions, material similarity and interfacial displacement continuity, the finite geometry under consideration has been formulated as a bonded semi-infinite wedge of included angle 360^o and therefore the stress state suffered in practice was established accurately. The proposed wedge model effectively models the dovetail geometry along with the socket end by considering the resulting interaction between the modes I, II stress concentration effects occurring near the sharp corners in the enclosed region. The focus of the current chapter is mainly for the case when the side clearance is negligible, thus enabling us to apply the linear elastic fracture mechanics formulation to obtain the tractions near the neighbourhood of the contact edge region. Problems of this class, when the interface is closed everywhere and adhered are amenable to asymptotic analysis and hence the asymptote corresponding to semi-infinite crack is used here. Conditions for edge closure and adhesion in terms of the semi-infinite crack asymptotes K_I and K_{II} has been formulated.

A finite example problem of a square block resting in an elastically similar rectangular trench is considered for our initial analysis, assuming the dovetail to be a right angled contact and with perfectly sharp edges. Application of normal load alone reveals additional components

of stress field in the form of T-stress, while the conventional stress intensities K_I and K_{II} becomes negligible. The solution however needs special treatment for T-stress, especially when the side clearance assumes a finite value, which will be covered in the next chapter. As a demonstration of validity of the results obtained by the crack asymptotes, the traction ratio values for the edge are matched with the equivalent numerical values with reasonably good accuracy. Furthermore the edge separation predicted by the asymptotes and FE seems to be in good agreement. For realistic coefficients of friction, the edge of contact is supposedly in intimately closed and adhered conditions.

Chapter 3

Semi-infinite Trench formulation and its application to contact problems with finite Edge Separation

3.1 Introduction

Chapter §2 discussed the solution to contact problems of the kind where the clearance between the blade root tip and the socket end nearly vanishes. The entire set up was then idealised as a crack problem and linear elastic fracture mechanics formulation was used to obtain the stress state adjoining the contact edge. When there is an appreciable finite gap beyond the edge of the contact, the behaviour changes considerably and therefore we need a comprehensive solution to characterize the tractions adjoining the edge. The aim of this chapter is to discuss the relevant methodology and asymptotic forms for obtaining a third solution for representative contact problems where the separation between the contact edge & any adjacent material is small but not negligible. Before looking at this, we intend to study the contact problem of a square block

resting in a half-plane (refer Section 3.2), idealised as a 270^o wedge, just to observe the behaviour when the finite width ratio $d/a \to \infty$. A brief description of T-stress occurring in certain modes of loading and the crack-tip stress state characterizing its behaviour has been provided. The displacement components for T-stress have been derived and included in the trench formulation along with the conventional stress intensities K_I and K_{II}. The trench solution is eventually applied to example finite width models. An estimate of stress intensification near the notch root tip has been done and compared with similar results obtained using the three quarter plane asymptotic method. Tractions along the line of interface are calculated using the notch intensities and compared with its finite element counterpart.

3.2 Asymptotics of a block resting on a free surface

Here we consider the opposite limit of edge separation of the problem considered in Section 2.4.1. The problem now can be treated as the case of a square block resting on a elastically similar half-plane (Figure 3.1), which has been studied before by Churchman [2006][20]. A cartesian coordinate set 'x' is defined to measure the contact characteristics along the interface. When the observation point moves very close to the edge of contact ($x/a \ll 1$), the three quarter plane solution applies, assuming the interface to be in intimately adhered and closed. In such a case we can use the solution prescribed by Williams [1952][54] (refer the book by Barber [1992][76]) for a semi-infinite wedge to infer the behaviour of the edge. The general form of a state of stress as defined by Williams is given as,

$$\sigma_{ij}\left(\rho,\phi\right) = K_I^N \rho^{\lambda_I - 1} f_{ij}^I\left(\phi\right) + K_{II}^N \rho^{\lambda_{II} - 1} f_{ij}^{II}\left(\phi\right), \tag{3.1}$$

Where the coordinate set (ρ, ϕ) is defined in Figure 2.1, describing asymptotically the con-

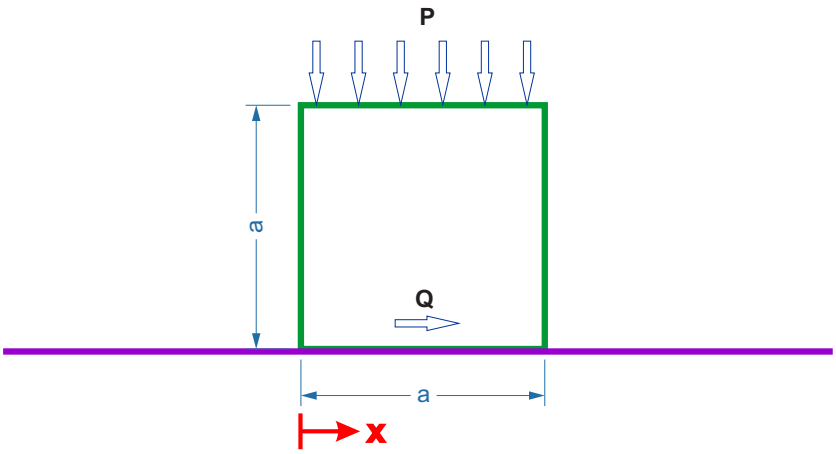


Figure 3.1: Finite example of a square punch in contact with a half-plane

tact of a block with a half-plane. The eigenvalues for this problem are given as $\lambda_I = 0.5445$, $\lambda_{II} = 0.9085$. Considering the fact that $\lambda_{II} > \lambda_I$, we can say that the mode I singularity is much stronger than mode II, as the edge is approached, i.e, as $x/a \to 0$. For observation points in the neighbourhood of the edge, the mode I stress intensity factor should be negative ($K_I^N < 0$) to maintain closure. The condition for no slip can then be calculated as $f > -\left|f^I_{\rho\phi}(\pi/4)\right| / f^I_{\phi\phi}(\pi/4)$. The expression on the right hand side can be obtained directly from the eigen-vectors for this problem and is 0.543 (Hills et al., [2004][77]). Before we take a look at the application of these results to the problem considered, it is worth bringing out further properties of Williams solution, as they will be referred to later. Although this was not appreciated at the time of Churchman's work [2006][20], the internal length scale within William's solution may profitably be brought out (Hills et al., [2011][78]) here. The internal length parameter d_0 may be defined as

$$d_0 = \left|\frac{K_{II}^N}{K_I^N}\right|^{\frac{1}{\lambda_I - \lambda_{II}}} . \tag{3.2}$$

By definition d_0 may be thought of as a parameter representing the distinction between the

mode I and mode II dominated zones in the neighbourhood of the notch tip. Thus we can say that, for observation points lie within the range $\rho < d_0$, it is the mode I singularity that controls the traction behaviour, as $\rho/d_0 \to 0$. On the other hand, when points lie outside this range, i.e, $\rho > d_0$, the tractions are governed by mode II singularity as $d_0/\rho \to 0$. Here, the condition for remote closure depends very much on the mode II stress intensity factor assuming a positive value ($K_{II}^N > 0$). The coefficient of friction needed to ensure remote stick is $f > -\left|f_{\rho\phi}^{II}(\pi/4)\right| / f_{\phi\phi}^{II}(\pi/4)$. The right hand side of the expression can be obtained directly from the eigen-vectors for this problem and is 0.219. We shall make a remark at this point that potential slip occurring in this region is directed in the opposite sense to that of the one happening in the mode I dominated region ($\rho < d_0$). The calibration of notch stress intensity factors for the left hand side edge in Figure 3.1 is given as follows

$$\left\{ \begin{array}{c} K_I^N (a)^{\lambda_I - 1} \\ K_{II}^N (a)^{\lambda_{II} - 1} \end{array} \right\} = \left[\begin{array}{cc} -0.30 & 0.353 \\ 0.216 & 0.466 \end{array} \right] \left\{ \begin{array}{c} P/a \\ Q/a \end{array} \right\}. \tag{3.3}$$

From Equation 3.3, we can deduce the condition for intimate closure as $Q/P < 0.85$. Finite element results predict nearly the same closure condition, which suggest that the normal tractions turns positive between the load factors $Q/P \sim 0.8 - 0.85$ as shown in Figure 3.2. Comparison with the 'closely fitting' solution (Equation 2.20) shows that the isolated block has a more stringent requirement for closure. And it shows a more stringent requirement for the coefficient of friction needed for edge stick conditions, provided the load factor lies in the range $-0.3 \lesssim Q/P \lesssim 0.8$ (see Figure 2.16).

The traction ratio results obtained by FE calculation for the whole length of the interface is shown in Figure 3.3. A magnification of the region near the LHS and RHS edges has been provided for clear vizualisation of asymptotic results. The dotted lines on both the corners

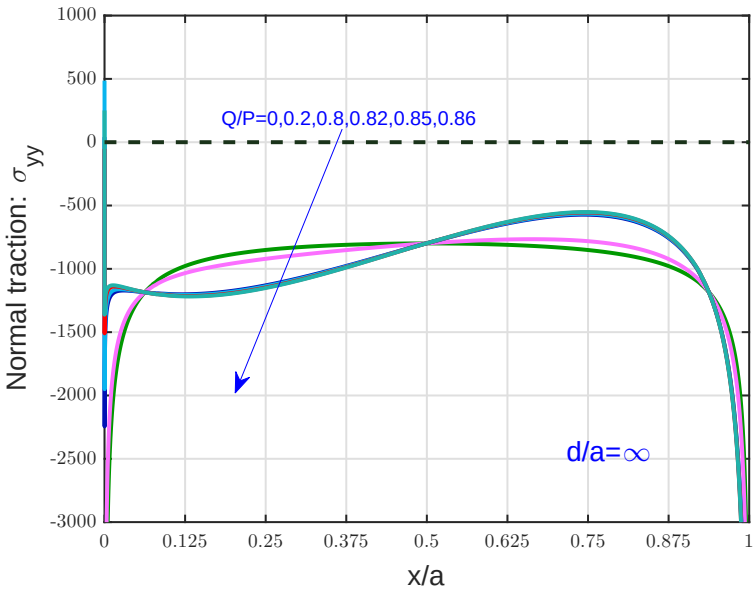


Figure 3.2: Response of Normal tractions σ_{yy} for the finite model with $d/a \longrightarrow \infty$ and Internal angle $\pi/2$ radians

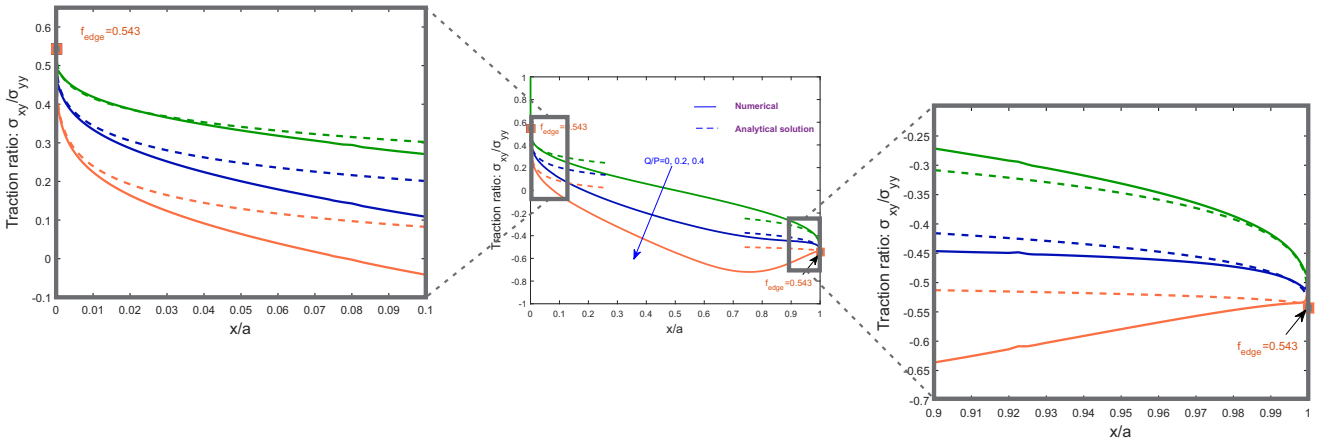


Figure 3.3: Traction ratio behaviour at different load factors Q/P for finite model with $d/a \longrightarrow \infty$ and Internal angle $\pi/2$ radians. The edges of the contact are zoomed-in for clear vizualisation of asymptotic results

shows the asymptotic representations of tractions computed by the Williams solution for a 270^o wedge. When a purely normal load is applied, the traction ratio response is anti-symmetric and reaches a value of 0.543 at the edges, as expected. When the shear force is increased, the

traction ratio remains constant at 0.543 at the edges and stick conditions prevail throughout the interface provided the coefficient of friction is at least this big. When the shear force exceeds about 40% of applied normal load, the internal maximum of the ratio of shear to direct traction exceeds that at the edges.

3.3 Solution methodology

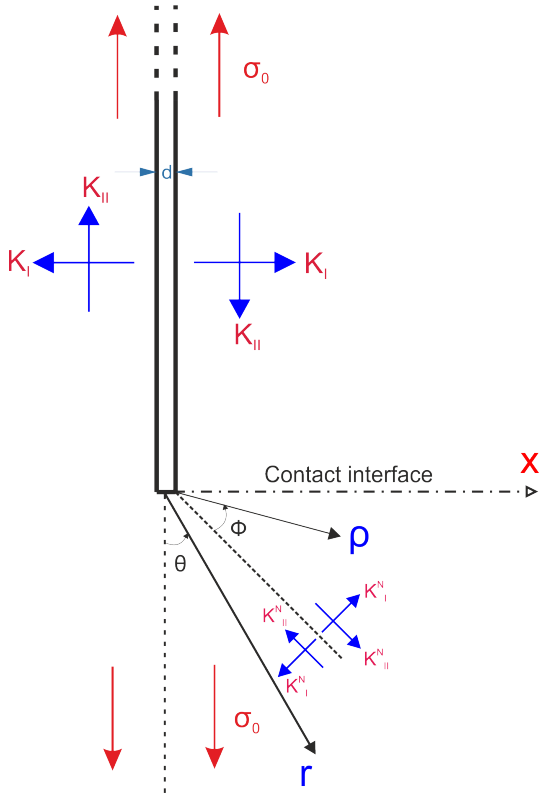


Figure 3.4: Semi-infinite description of a trench model with a finite separation adjacent to contact

We now have a fair idea as how the contact problem behaves at the limits of the ratio $d/a = 0$ and ∞ and these were discussed in Sections 2.4.1 and 3.2 respectively. The problem that we are now interested in solving is a contact with finite separation, which lies between these two extreme limits but where the d/a value is actually quite small ($d/a \ll 1$). The straightforward

approach is to make use of the notch calibrations K_I^N and K_{II}^N, that vary with each d/a. This does not seem to be an efficient method, as it needs a finite element model for each variation of the width ratio d/a, which is often a cumbersome process. The intention, therefore, is to formulate a solution which computes the notch intensities, with minimal effort in finite element modelling and subsequent semi-analytical calculations. Therefore we have looked at a further possibility, where we have a geometrical feature in the form of semi-infinite trench of width d in an infinite plane as shown in Figure 3.4 and try to obtain a response in the neighbourhood of the notch tip region. The presence of sharp corners adjoining the trench region induces the three quarter plane solution locally, i.e., as the observation point approaches notch tip ($\rho \ll d$). However, when the observation point exceeds a length scale equivalent to the finite width, i.e., as ($r \gg d$), we expect a crack-like behaviour, where the stress and displacement fields characterizing this region exhibits a square root singular response. This enables us to assign loading in the form of crack-tip stress intensity factors K_I and K_{II}, together with the second term in the series expansion of the state of crack-tip stress field called T-stress σ_0, which simulates the intended behaviour.

The primary output we intend to compute is the state of stress along the line of interface at an angle $\phi = \pi/4$ from the bisector. As discussed above, when the observation point is close to the notch tip region ($\rho/d \ll 1$), the wedge solution corresponding to a three quarter plane applies. Once we know this solution, we can infer what happens along the edge by collocating this solution (Figure 3.4) in to geometry of a true crack model (Figure 2.8a), we can solve for the finite width trench shown in Figure 2.2a, when d/a is small and finite. Alternatively, the term collocation here refers to the case where the stress state corresponding to a crack domain is imposed on the outer region of the semi-infinite contact model (with a finite width) in Figure 3.6a to enable the wedge solution to be computed for the edge. For a practical finite model, as the width of the gap increases, the effective area of the crack domain shrinks and therefore

the solution computed using this particular approach may no longer be accurate. This can be summarised in Figure 3.5.

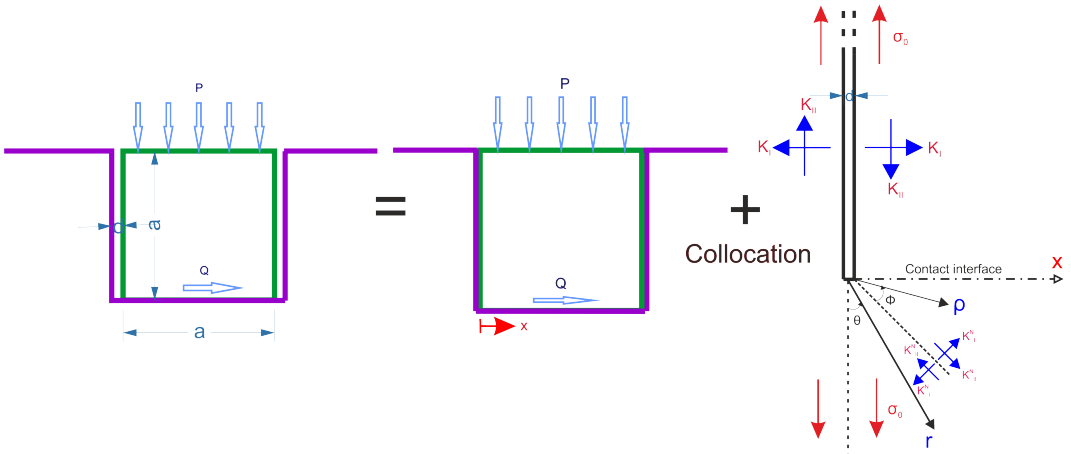
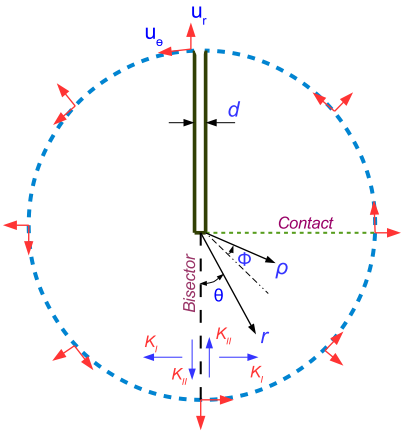
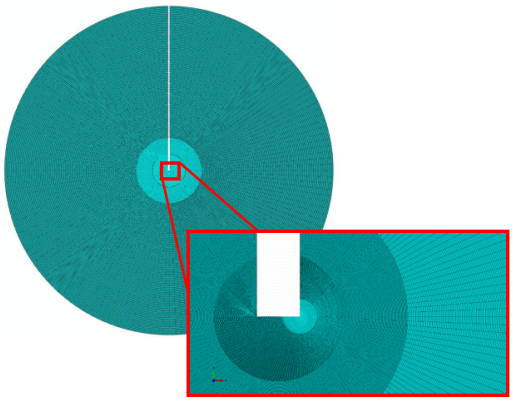


Figure 3.5: An overview of solution strategy for solving finite width models

3.4 Setting up of the asymptotic form



(a) Asymptotic representation of a finite width model



(b) Representation of FE model used to compute the trench solution

Figure 3.6: Trench solution

To formulate a solution for the trench problem described in Figure 3.4, a finite element model was developed in the commercial code ABAQUS. It is a circular type model with the outer boundary positioned at a distance $r = 100 * d$ from the notch tip region as shown in Figure 3.6a. A finely refined mesh was developed with elements in the radial direction graded to ensure a constant stress gradient across each element so as to achieve a good convergence. The loading was applied through imposed boundary displacements, instead of the conventional traction conditions, so as to obtain a stable and controlled solution. These displacement components are given by the classical semi-infinite crack solution as defined by Irwin [1975][75] (or specializing Williams solution defined for a notch of included angle 2π radians) for mode I loading as follows

$$\left\{ \begin{array}{c} u_r \\ u_\theta \end{array} \right\} = \frac{K_I}{2E}\sqrt{\frac{r}{2\pi}} \left\{ \begin{array}{c} (1+\nu)\left[(2\kappa-1)\cos(\theta/2) - \cos(3\theta/2)\right] \\ (1+\nu)\left[-(2\kappa+1)\sin(\theta/2) + \sin(3\theta/2)\right] \end{array} \right\}, \tag{3.4}$$

where E is Young's modulus, ν is Poisson's ratio and κ is Kolosov's constant. From Equation 3.4 it is evident that the form of the solution is dependent on Poisson's ratio and this was chosen in our finite element calculations to be 0.3. We assume plane strain conditions and hence Kolsov's constant is $\kappa = 3 - 4\nu$. The terms corresponding to mode II loading are,

$$\left\{ \begin{array}{c} u_r \\ u_\theta \end{array} \right\} = \frac{K_{II}}{2E}\sqrt{\frac{r}{2\pi}} \left\{ \begin{array}{c} (1+\nu)\left[-(2\kappa-1)\sin(\theta/2) + 3\sin(3\theta/2)\right] \\ (1+\nu)\left[-(2\kappa+1)\cos(\theta/2) + 3\cos(3\theta/2)\right] \end{array} \right\}. \tag{3.5}$$

It is to be noted, here, that the solutions incorporate the factor $\sqrt{2\pi}$ in the expressions, and hence the stress intensity factors are consistent with fracture mechanics, that is they are defined as,

$$K_I = \lim_{r \to 0} \sqrt{2\pi r}\sigma_{\theta\theta}(r, 0), \tag{3.6}$$

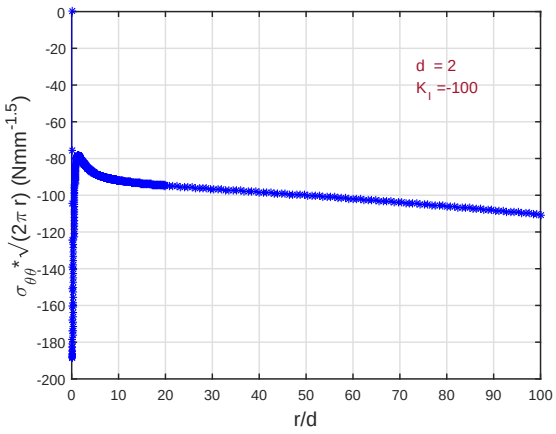
$$K_{II} = \lim_{r \to 0} \sqrt{2\pi r}\sigma_{r\theta}(r, 0). \tag{3.7}$$

The generalised stress intensity factors quantifying the symmetric and anti-symmetric eigen solutions for a three quarter plane wedge along the trench root are denoted by K_I^N and K_{II}^N respectively. These quantities does not include the arbitrary factor $\sqrt{2\pi}$, and therefore the stress intensity factors are defined by,

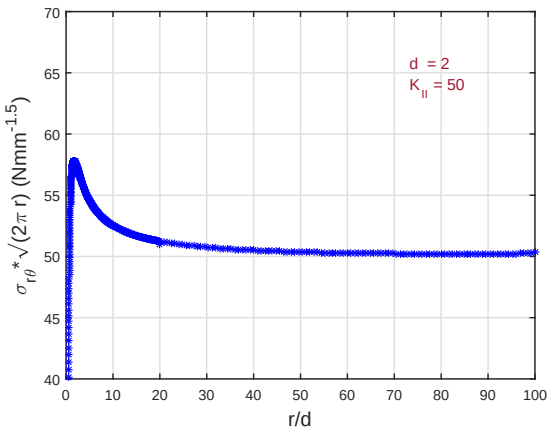
$$K_I^N = \lim_{\rho \to 0} \rho^{(1-\lambda_I)}\sigma_{\phi\phi}(\rho, 0), \tag{3.8}$$

$$K_{II}^N = \lim_{\rho \to 0} \rho^{(1-\lambda_{II})}\sigma_{\rho\phi}(\rho, 0). \tag{3.9}$$

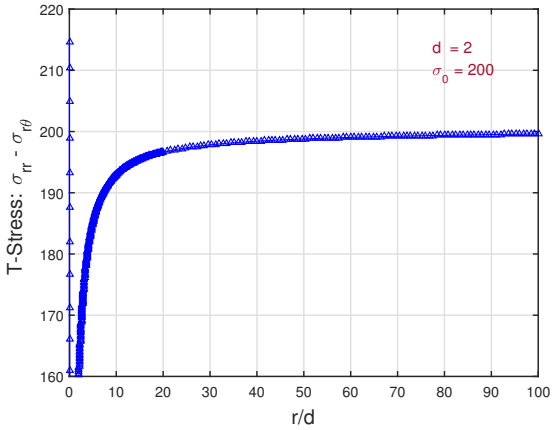
Here the quantities λ_I and λ_{II} represent the mode I and mode II eigenvalues, emerge from Williams solution, and signify the order of singularity. As stated above a finely refined mesh was generated close to the trench root and in the neighbourhood region, to obtain a converged solution. Loading was applied in the form of imposed displacements through the components defined in Equations 3.4 and 3.5. Additional loading in the form of T-stress was also assigned. A generic formulation for displacement components for T-stress would be discussed in the subsequent sections. An ABAQUS user subroutine called 'DISP' (refer Appendix A) was developed, which assigns the displacements corresponding to each eigensolution to the nodes present in the outer boundary of the finite element model. This creates the necessary stress and displacement fields consistent with the semi-infinite crack formulation, in the far regions of the model. The functionality of the user routine is recognised through the converged parameters K_I, K_{II} and σ_0 that are measurable along the outer boundary and consistent with the input displacements (refer Figure 3.7). Finite element output reveals the tractions $\sigma_{\phi\phi}$ and $\sigma_{\rho\phi}$ along the trench root bisector (refer Figure 3.6a), measured at an angle $\pi/4$ radians from the interface. The stress intensity factors K_I^N and K_{II}^N are calculated from Equations 3.8 and



(a) K_I convergence



(b) K_{II} convergence



(c) σ_0 convergence

Figure 3.7: Convergence behaviour of stress intensity parameters for the semi-infinite model in Figure 3.6a. These results were plotted separately for the crack intensity inputs $K_I = -100$, $K_{II} = 50$ and $\sigma_0 = 200$ which are measurable at the intersection of the outer boundary and the centreline i.e., at $r/d = 100$

3.9, after obtaining a converged solution near the notch tip region and the matrix of coefficients denoting the generalised stress intensity factors are then computed for the right hand side edge

as follows.

$$\left\{ \begin{array}{c} K_I^N d^{(\lambda_I - 1)} \\ K_{II}^N d^{(\lambda_{II} - 1)} \end{array} \right\} = \left[\begin{array}{ccc} 0.802 & -1.102 & 0.257 \\ 0.384 & +0.51 & -0.569 \end{array} \right] \left\{ \begin{array}{c} \frac{K_I}{\sqrt{2\pi d}} \\ \frac{K_{II}}{\sqrt{2\pi d}} \\ \sigma_0 \end{array} \right\} \tag{3.10}$$

As stated earlier, in Section 3.2, the requirement that the interface adjacent to the edge remains closed is that $K_I^N < 0$. We can then re-write the same in terms of the crack-tip stress intensity factors K_I and K_{II} as,

$$K_{II}/K_I > 0.73 \ \forall \ K_I > 0, K_{II} > 0 \tag{3.11a}$$

$$K_{II}/K_I < 0.73 \ \forall \ K_I < 0, K_{II} > 0 \tag{3.11b}$$

Figure 3.8 shows the ratio of tractions along the line of interface measured at an angle $\pi/2$ radians from the crack bisector. These were plotted for different ratios of crack-tip stress intensity factors ranging from -2 to 0.75. It is clear from the plot that the edge traction ratios for most of the values of K_{II}/K_I converge to the characteristic ratio of 0.543 near the notch tip region, suggesting the presence of three quarter plane mode I solution. As we move interior along the contact region, the traction ratio may either increase or decrease depending on the mode mixity of K_{II} and K_I prevailing throughout the region. We note that when $K_{II}/K_I = 0$, a pure mode I crack eigen-solution exists throughout the far region of the contact. Homogeneous conditions exist for the entire interface, when K_{II}/K_I reaches a value of -0.75, with the traction ratio remaining constant at 0.543. When $K_{II}/K_I < -0.75$, condition for adhesion is more stringent for the interior region than that for the edge region. When $K_{II}/K_I > -0.75$, the interior traction ratio is less than the edge values and therefore a coefficient of friction equivalent to 0.543 is sufficient to ensure stick conditions throughout the interface. Mode II eigen-solution exist all along the interface, when the ratio K_{II}/K_I reaches a value of 0.75 and the coefficient

of friction needed for stick conditions remains at 0.218. Another interesting property of the

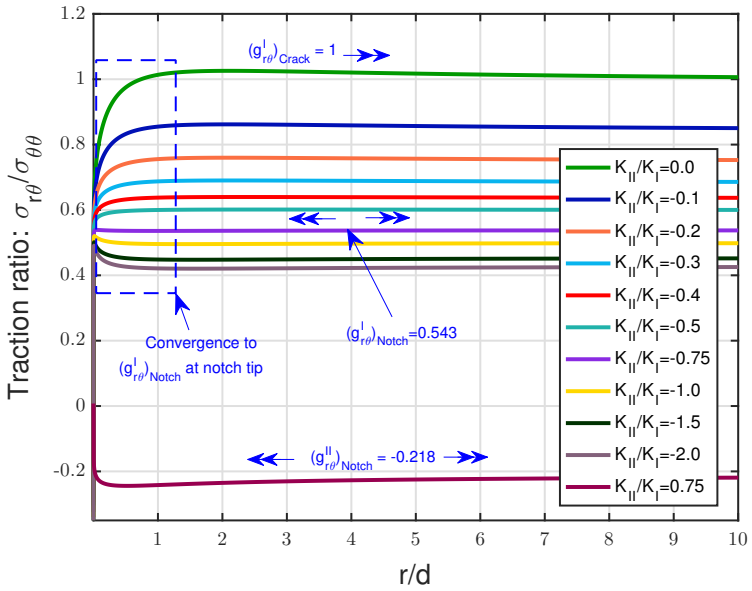


Figure 3.8: Traction ratio response of asymptotic model at mixed mode conditions for Internal angle $\pi/2$ radians

trench solution is that it can be applied to compute the internal length parameter d_0, which distinguishes the regimes that corresponds to symmetric and anti-symmetric eigen-solutions close to the notch tip region. The main advantage here is that we can directly compute the parameter from the crack-tip stress intensity factors without having to calculate the notch intensities. Recall from Equation 3.2 the definition for the internal length parameter,

$$d_0 = \left| \frac{K_{II}^N}{K_I^N} \right|^{\frac{1}{\lambda_I - \lambda_{II}}} . \tag{3.12}$$

From Equation 3.10, we can then re-write the notch intensities K_I^N and K_{II}^N in terms of crack-tip

stress intensity factors K_I and K_{II} as,

$$K_I^N = \frac{d^{(0.5-\lambda_I)}}{\sqrt{2\pi}} (0.802K_I - 1.102K_{II}) \tag{3.13a}$$

$$K_{II}^N = \frac{d^{(0.5-\lambda_{II})}}{\sqrt{2\pi}} (0.384K_I + 0.51K_{II}) \tag{3.13b}$$

Substituting Equation 3.13 in 3.12, we find the expression for d_0 in terms of the finite width d, K_I and K_{II} as,

$$\frac{d_0}{d} = \left[\frac{0.384 + 0.51\frac{K_{II}}{K_I}}{0.802 - 1.102\frac{K_{II}}{K_I}}\right] \left(\frac{1}{\lambda_I - \lambda_{II}}\right) \tag{3.14}$$

Figure 3.9 illustrates the response of the internal length parameter ratio d_0/d as a function of crack-tip stress intensity factor ratio K_{II}/K_I, when the latter is varied within the interval $[-4, 1]$. When $K_{II}/K_I \simeq 0.75$, the ratio $d_0/d \longrightarrow 0$ and this suggests the existence of pure mode II conditions in the region adjoining notch tip. As the ratio K_{II}/K_I increases in the negative range, we tend to observe mixed mode conditions, with the mode I eigen-solution dominating the near-tip region. When K_{II}/K_I reaches a value equivalent to -0.75, d_0/d increases rapidly and reaches infinitely high values ($\sim 1E06$) and thus pure mode I conditions exits throughout the interface. These results may be matched with the finite element results presented in Figure 3.8, where it reaches the characteristic mode I and mode II traction ratio's of 0.543 and -0.218 at the respective stress intensity ratio's discussed above. From Figure 2.14a, we see that the contact looks more stable and intimately closed at negative shear loads, where the stress intensity ratio K_{II}/K_I varies between approximately -0.5 and -2. We observe from Figure 3.9 that, mode I conditions dominate over this interval of K_{II}/K_I and that the contact experiences compressive behaviour and is intimately closed.

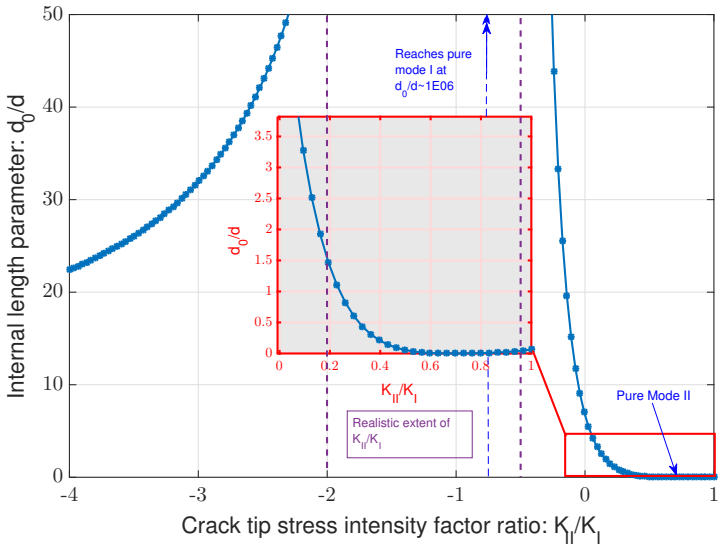


Figure 3.9: Response of internal length parameter (d_0/d) at various stress intensity factor ratio's K_{II}/K_I

3.5 Influence of non-singular terms (T-stress) on the behaviour of the contact

The linear elastic stresses around the crack-tip, generally contain the symmetric and anti-symmetric components, usually referred in the literature as mode I and mode II singular stress fields. However, for specific loading scenarios, the non-singular (higher order) terms in the solution series expansion assume more significance than the conventional singular terms. The crack-tip stress state including just the next term as given by Jeong et al., [2003][79] can

be represented as follows

$$\sigma_{rr} = \frac{1}{\sqrt{2\pi r}} \left\{ K_I \cos\frac{\theta}{2}\left[1 - \sin\frac{\theta}{2}\sin\frac{3\theta}{2}\right] + K_{II}\sin\frac{\theta}{2}\left[1 - 3\sin^2\frac{\theta}{2}\right]\right\} + \sigma_0 \cos^2\theta \tag{3.15a}$$

$$\sigma_{\theta\theta} = \frac{1}{\sqrt{2\pi r}} \left\{ \cos\frac{\theta}{2}\left[K_I \cos^2\frac{\theta}{2} - 3K_{II}\sin\frac{\theta}{2}\cos\frac{\theta}{2}\right]\right\} + \sigma_0 \sin^2\theta \tag{3.15b}$$

$$\sigma_{r\theta} = \frac{1}{\sqrt{2\pi r}} \left\{ \cos\frac{\theta}{2}\left[K_I \sin\frac{\theta}{2}\cos\frac{\theta}{2} + K_{II}\left(1 - 3\sin^2\frac{\theta}{2}\right)\right]\right\} - \sigma_0 \sin\theta\cos\theta. \tag{3.15c}$$

Here r and θ are the polar coordinates centered at the crack-tip, and K_I and K_{II} are the stress intensities representing the symmetric and anti-symmetric components, and σ_0 being the non-singular term, widely known as T-stress in the literature. The T-stress can generally be recognised as a measure of constraint around the crack-tip and is often used in the literature to predict crack path stability. The T-stress acts in a direction parallel to the crack plane, and is important where there are remote loads applied in the same direction as the crack plane itself (refer Figure 3.10). If there are only remote stresses parallel with the crack it is only the T-stress which characterize the stress field, while all singular terms in Equation 3.15 vanish. Various methods have been developed over the last 25 years to compute the magnitude of T-stress in cracked components and most of them are restricted to either simple geometries or need special numerical techniques. The standard approach is to perform a linear elastic finite element analysis, which can be applied to any complex geometries and loading configurations. The T-stress can be obtained using the expression below after finding the normal and radial tractions ($\sigma_{\theta\theta}$ and σ_{rr}) along the line corresponding to the bisector ($\theta = 0$), (Ayatollahi [1998][80])

$$\sigma_0 = \lim_{r\to 0}\left[\sigma_{rr}(r,0) - \sigma_{\theta\theta}(r,0)\right] \tag{3.16}$$

An investigation was done to check for the occurrence of T-stress in different loading config-

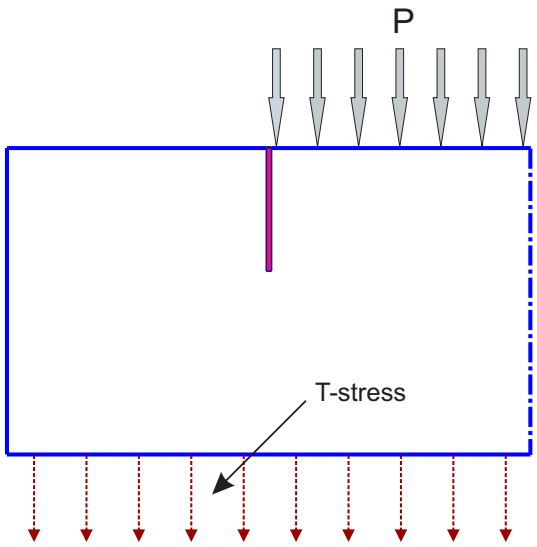


Figure 3.10: Illustration of occurrence of T-stress where the applied loads and crack plane are at parallel

urations using the geometry shown in Figure 3.10, that simulates the finite true crack model we discussed earlier (refer Figure 2.8a). As stated before, in Section 2.4.1, the configuration shown in Figure 3.11a can be split in to symmetric and anti-symmetric components of loading and are shown in Figures 3.11b and 3.11c respectively. For the configurations in Figure 3.11a-c, normal load alone is applied in the vertical direction. The bottom face is assigned symmetric boundary condition, restraining it in the normal direction. Finite element output reveals no mode I and mode II stress intensities for Figure 3.11b, but with considerable amount of T-stress, meaning that the entire stress state is governed by components corresponding to T-stress. The anti-symmetric loading in configuration 3.11c, exhibits a pure mode II behaviour and does not produce any T-stress components. However it shows an infinitesimal K_I value, which is expected to vanish as the size of the model 'b' is increased relative to the crack length 'a'. Thus the original model shown in Figure 3.11a is a superposed version of (b) and (c) exciting mode II and T-stress behaviour respectively. Now consider the case of configuration 3.11d, where the loading is applied in a direction normal to the plane of the crack. This exhibits a pure mode I behaviour, with no K_{II} or σ_0 components. Thus we can conclude by saying that T-stress

components only occur for the case where loading is applied in a direction parallel to the plane of crack. It does not occur for pure mode II conditions and for the case where the loading being applied perpendicular to the crack plane.

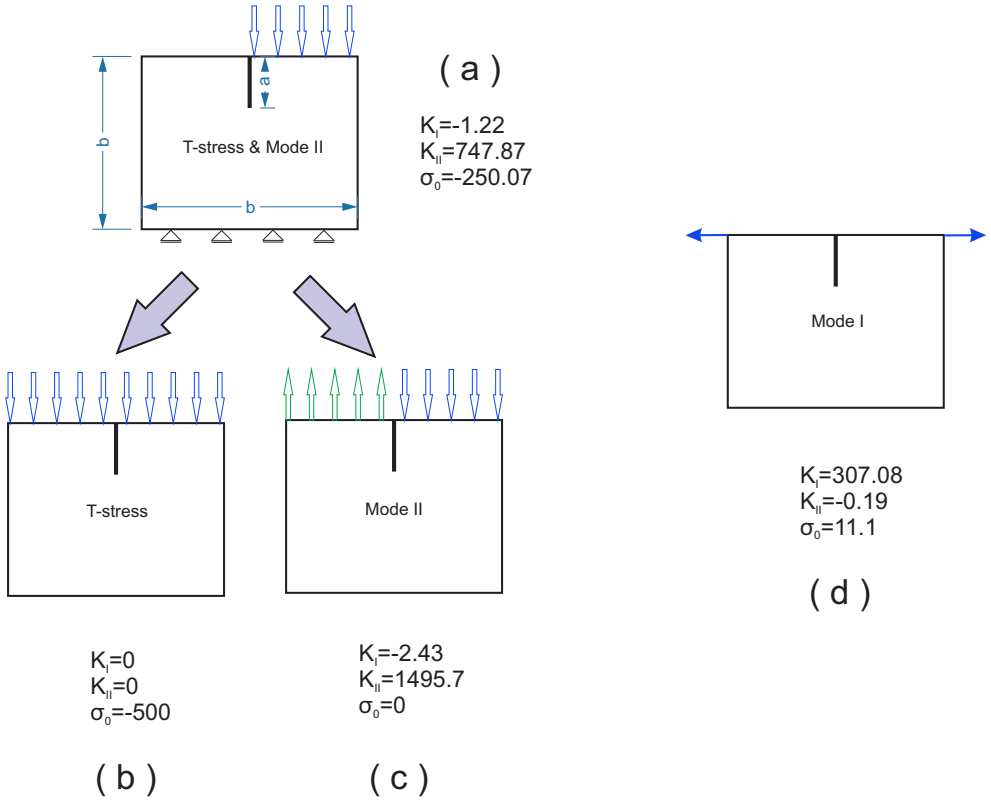


Figure 3.11: T-stress investigation at various loading configurations. Loading is applied parallel to the crack plane in Case (a) which can be represented as a combination of symmetric and anti-symmetric loads (case (b) and (c)) generating pure T-stress and mode II response respectively. Case (d) is subjected to loads perpendicular to the plane of crack and generates a pure mode I response

3.6 Displacement component formulation for T-stress

From Section §3.4 we know that the loading for asymptotic model is done by imposing displacements around, the outer boundary, and comprising the singular components of stress intensities K_I and K_{II} and the non-singular component σ_0. The displacement components for the singular

terms are defined by the semi-infinite crack solution as given in Equations 3.4 and 3.5 respectively. However the displacement components corresponding to the T-stress are not available yet in the literature. In order to simulate exactly the stress state due to practical loading conditions in the trench model defined in Figure 3.4, the displacement field resulting from a T-stress needs to be appended to the fields due to the singular components K_I and K_{II}. This enables us to predict accurately the notch intensities K_I^N, K_{II}^N for any given finite model and consequently compute the resulting tractions along the line of interface. For these practical reasons, a formulation for displacement components corresponding to T-stress is necessary for inclusion in the trench solution discussed in Equation 3.10. The following sections discuss briefly the derivation of the radial (u_r) and tangential (u_θ) displacement components resulting from the occurrence of T-stress in the near tip region.

3.6.1 Derivation of radial displacements u_r

Recall from Equation 3.15, the expressions defining the crack-tip stress components in the radial and tangential direction,

$$\sigma_{rr} = \frac{1}{\sqrt{2\pi r}} \left\{ K_I \cos\frac{\theta}{2}\left[1 - \sin\frac{\theta}{2}\sin\frac{3\theta}{2}\right] + K_{II}\sin\frac{\theta}{2}\left[1 - 3\sin^2\frac{\theta}{2}\right]\right\} + \sigma_0 \cos^2\theta, \tag{3.17a}$$

$$\sigma_{\theta\theta} = \frac{1}{\sqrt{2\pi r}} \left\{ \cos\frac{\theta}{2}\left[K_I \cos^2\frac{\theta}{2} - 3K_{II}\sin\frac{\theta}{2}\cos\frac{\theta}{2}\right]\right\} + \sigma_0 \sin^2\theta. \tag{3.17b}$$

In order to simplify the algebraic calculations, the terms corresponding to T-stress alone is considered for the formulation. Assuming plane strain conditions, we can recall from linear elasticity theory, the definition of stress-strain relationship,

$$\varepsilon_{rr} = \frac{1+\upsilon}{E}\left[(1-\upsilon)\,\sigma_{rr} - \upsilon\sigma_{\theta\theta}\right]. \tag{3.18}$$

The definition of strain-displacement components can be written as,

$$\varepsilon_{rr} = \frac{\partial u_r}{\partial r}. \tag{3.19}$$

Substituting the terms corresponding to T-stress in Equations 3.17a and 3.17b in the stress-strain Equation 3.18 gives,

$$\varepsilon_{rr} = \frac{(1+\upsilon)\sigma_0}{E}\left[(1-\upsilon)\cos^2\theta - \upsilon\sin^2\theta\right]. \tag{3.20}$$

Integrating the strains with respect to r yields the radial displacements u_r,

$$u_r = \int \varepsilon_{rr} dr. \tag{3.21}$$

Substituting Equation 3.20 in the above integral in Equation 3.21 gives,

$$u_r = \frac{\sigma_0(1+\upsilon)}{E}\int \left[(1-\upsilon)\cos^2\theta - \upsilon\sin^2\theta\right] dr. \tag{3.22}$$

Recall the definition of the integrals,

$$\int \sin^2\theta d\theta = \frac{1}{2}\left(\theta - \sin\theta\cos\theta\right), \tag{3.23a}$$

$$\int \cos^2\theta d\theta = \frac{1}{2}\left(\theta + \sin\theta\cos\theta\right). \tag{3.23b}$$

Integrating Equation 3.22 using Equation 3.23 and further simplification gives,

$$u_r = \frac{r\sigma_0(1+\upsilon)}{E}\left[\cos^2\theta - \upsilon\cos^2\theta - \upsilon\sin^2\theta\right]. \tag{3.24}$$

The final equation after simplification can be written down in the following form

$$\boxed{u_r = \frac{r\sigma_0(1+\upsilon)}{E}\left[\cos^2\theta - \upsilon\right].} \tag{3.25}$$

3.6.2 Derivation of tangential displacements u_θ

Again assuming plane strain conditions, we define from linear elasticity theory the stress-strain relationship,

$$\varepsilon_{\theta\theta} = \frac{1+\upsilon}{E}\left[-\upsilon\sigma_{rr} + (1-\upsilon)\,\sigma_{\theta\theta}\right]. \tag{3.26}$$

We can then define the strain-displacement components as follows,

$$\varepsilon_{\theta\theta} = \frac{1}{r}\frac{\partial u_\theta}{\partial\theta} + \frac{u_r}{r}. \tag{3.27}$$

Re-writing the same in terms of tangential displacements u_θ gives,

$$r\varepsilon_{\theta\theta} - u_r = \frac{1}{r}\frac{\partial u_\theta}{\partial\theta}, \tag{3.28a}$$

$$u_\theta = \int (r\varepsilon_{\theta\theta} - u_r)\,d\theta, \tag{3.28b}$$

$$u_\theta = r\int \varepsilon_{\theta\theta}d\theta - \int u_r d\theta. \tag{3.28c}$$

Evaluating the integral $\int \varepsilon_{\theta\theta}d\theta$ in Equation 3.28c yields,

$$\int \varepsilon_{\theta\theta}d\theta = \int \frac{1+\upsilon}{E}\left[-\upsilon\sigma_{rr} + (1-\upsilon)\,\sigma_{\theta\theta}\right]d\theta. \tag{3.29}$$

Substituting the relevant expressions for the stress components σ_{rr} and $\sigma_{\theta\theta}$ from Equations

3.17a and 3.17b gives,

$$\int \varepsilon_{\theta\theta} d\theta = \frac{1+\upsilon}{E} \int \left[-\upsilon \sigma_0 \cos^2\theta + (1-\upsilon)\,\sigma_0 \sin^2\theta \right] d\theta. \tag{3.30}$$

Applying the integrals defined in Equation 3.23 and evaluating further gives,

$$\int \varepsilon_{\theta\theta} d\theta = \frac{\sigma_0(1+\upsilon)}{2E} \left[-\upsilon(\theta + \sin\theta\cos\theta) + (1-\upsilon)\,(\theta - \sin\theta\cos\theta) \right] d\theta, \tag{3.31a}$$

$$= \frac{\sigma_0(1+\upsilon)}{2E} \left[\theta\,(1-2\upsilon) - \sin\theta\cos\theta \right]. \tag{3.31b}$$

Substituting $\int \varepsilon_{\theta\theta} d\theta$ and u_r from Equations 3.31b and 3.25 in expression 3.28c gives,

$$u_\theta = \frac{r\sigma_0\,(1+\upsilon)}{2E} \left[\theta\,(1-2\upsilon) - \sin\theta\cos\theta \right] - \frac{r\sigma_0\,(1+\upsilon)}{E} \left[\frac{1}{2}\,(\theta + \sin\theta\cos\theta) - \upsilon\theta \right]. \tag{3.32}$$

Further simplification results in final equation of the form,

$$\boxed{u_\theta = \frac{r\sigma_0\,(1+\upsilon)}{E}\,(-\sin\theta\cos\theta)} \tag{3.33}$$

3.7 Application to finite models

We already have looked in Sections 2.4.1 and 3.2, at the behaviour of contact when the width ratio $d/a \longrightarrow 0$ and ∞. This section discusses mainly the response of contacts with a finite separation adjacent to the edge, such as that shown in Figure 3.12. It is clear from the calibration Equation 3.10 that the main output of trench solution are the notch intensities K_I^N and K_{II}^N, found along the notch bisector at an angle of $\pi/4$ radians from the interface. We expect these results to match very closely with the reference solution calculated using the three quarter plane method as long as the separation is finite and small. Therefore the initial task was to try and

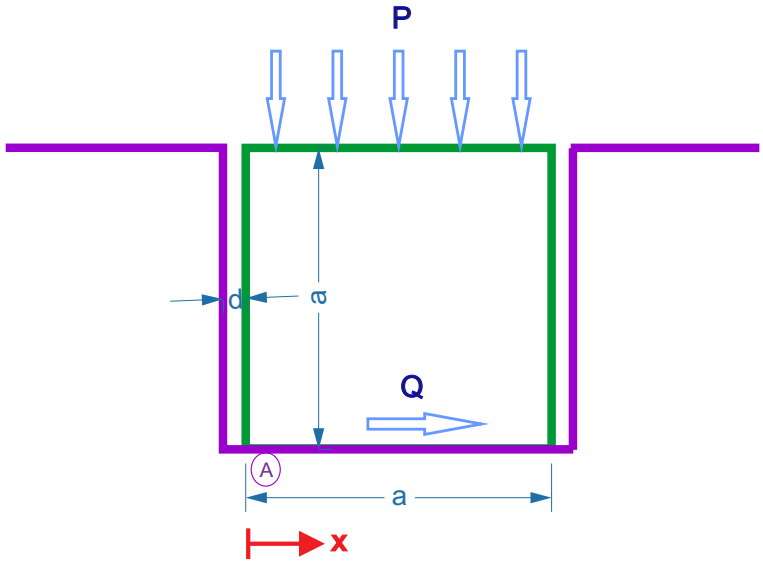
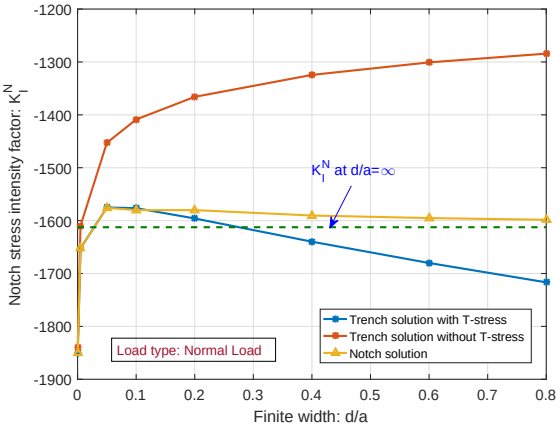


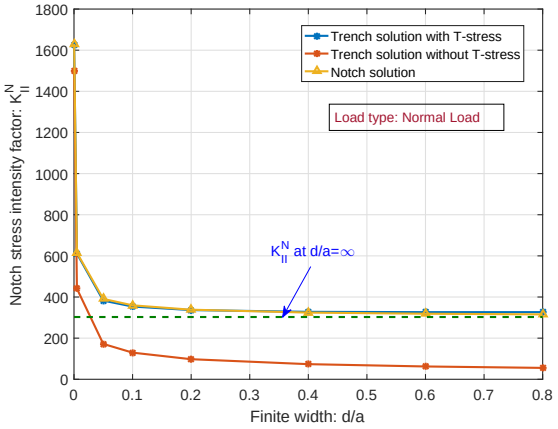
Figure 3.12: Representation of an example finite width geometry

compare the notch intensities computed by both methods and make sure the output of trench solution is consistent with three quarter plane method as the finite separation is reduced. This can be evidenced in Figures 3.13 and 3.14, for separate cases of application of normal and shear loads. Three set of values of notch intensities are plotted based on the mode of calculation, namely the *'Trench solution with T-stress'*, *'Trench solution without T-stress'* and the *'Notch solution'* (computed using three quarter plane method). Here the first one refers to the case where the effects of T-stress are considered in the formulation 3.15, while for the next case only the singular terms are considered. The dotted line represents the reference values of notch intensities when the block is positioned at a remote distance from the side wall of the trench, ie., when $d/a \longrightarrow \infty$. Hence as the finite width d/a is increased, the notch solution converge asymptotically to this reference value. When normal load alone is applied, we observe from Figure 3.13 that Trench solution with T-stress converge smoothly to the notch solution as d/a is reduced. On the other hand, the Trench solution without T-stress shows huge discrepancy with the reference solution. This shows that, for normal loads, stress intensification due to

T-stress need to be included in the solution, in order to establish better the correct stress state in the neighbourhood of the notch tip region.



(a) Response of K_I^N when normal load alone is applied

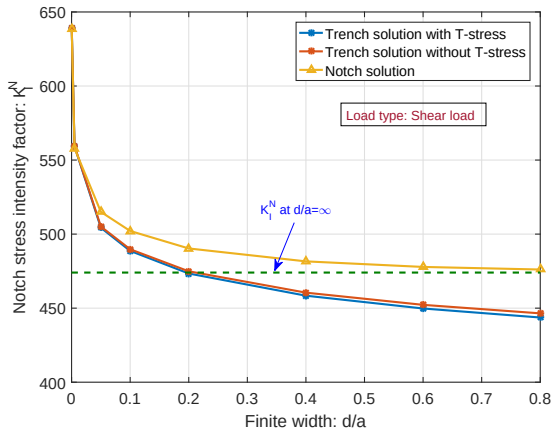


(b) Response of K_{II}^N when normal load alone is applied

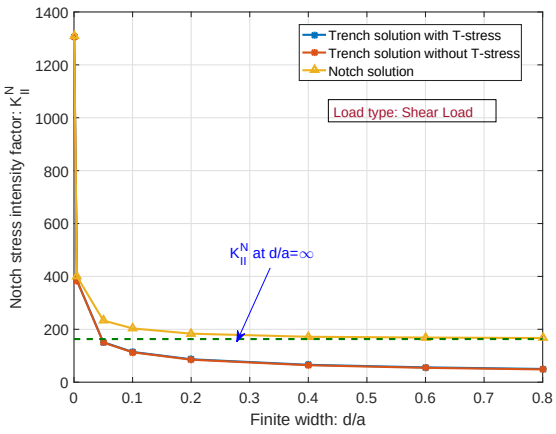
Figure 3.13: Variation of notch intensities K_I^N and K_{II}^N at various finite widths d/a, when normal load alone is applied. The dotted line in the plot refers to the reference values of notch intensities when $d/a \longrightarrow \infty$

Figure 3.14 shows the response of the notch intensities when a shear load alone is applied. This corresponds to the case where the external loads are applied in a direction perpendicular to the plane of crack. We have noted earlier in Section §3.5 that, for such a scenario, the effect of the T-stress would be negligible, and as a consequence the curves for the Trench solution with and without a T-stress overlay each other (refer Figure 3.14a). Further, it converges accurately towards the notch solution at reduced widths, as it did for the case of normal loads.

Now that we have confidence that the notch intensities computed by the Trench solution are accurate, we proceed to the next stage where the normal and shear loads are applied together on a finite true crack model shown in Figure 2.8a and compute the crack-tip stress intensity factors K_I, K_{II} and the T-stress component σ_0 using the calibrations given in Equation 2.19. The notch intensities K_I^N and K_{II}^N, can then be calculated using these input parameters and the



(a) Response of K_I^N and K_{II}^N when shear load alone is applied



(b) Response of K_I^N and K_{II}^N when shear load alone is applied

Figure 3.14: Variation of notch intensities K_I^N and K_{II}^N at various finite widths d/a, when shear load alone is applied. The dotted line in the plot refers to the reference values of notch intensities when $d/a \longrightarrow \infty$

solution defined in Equation 3.10. Williams series solution then defines the tractions ($\sigma_{\phi\phi}$ and $\sigma_{\rho\phi}$) along any particular angular direction within the asymptotic region. The traction ratio $\dfrac{\sigma_{\rho\phi}}{\sigma_{\phi\phi}}$ along the line of the interface can be subsequently found, which determines the coefficient of friction needed for adhered conditions. This calculation is summarised here, where we first define the generic state of stress near the tip of the notch,

$$\sigma_{\phi\phi}(\rho,\phi) = K_I^N \rho^{\lambda_I - 1} f_{\phi\phi}^I(\phi) + K_{II}^N \rho^{\lambda_{II} - 1} f_{\phi\phi}^{II}(\phi), \tag{3.34a}$$

$$\sigma_{\rho\phi}(\rho,\phi) = K_I^N \rho^{\lambda_I - 1} f_{\rho\phi}^I(\phi) + K_{II}^N \rho^{\lambda_{II} - 1} f_{\rho\phi}^{II}(\phi). \tag{3.34b}$$

Then, the traction ratio $\dfrac{\sigma_{\rho\phi}(\rho,\phi)}{\sigma_{\phi\phi}(\rho,\phi)}$ can be defined as,

$$\frac{\sigma_{\rho\phi}(\rho,\phi)}{\sigma_{\phi\phi}(\rho,\phi)} = \frac{K_I^N \rho^{\lambda_I - 1} f_{\rho\phi}^I(\phi) + K_{II}^N \rho^{\lambda_{II} - 1} f_{\rho\phi}^{II}(\phi)}{K_I^N \rho^{\lambda_I - 1} f_{\phi\phi}^I(\phi) + K_{II}^N \rho^{\lambda_{II} - 1} f_{\phi\phi}^{II}(\phi)} \tag{3.35}$$

After further algebraic manipulations, we have the final form of the expression as follows,

$$\frac{\sigma_{\rho\phi}(\rho,\phi)}{\sigma_{\phi\phi}(\rho,\phi)} = \frac{f^I_{\rho\phi}(\phi) + \dfrac{K^N_{II}}{K^N_I}\rho^{\lambda_{II}-\lambda_I} f^{II}_{\rho\phi}(\phi)}{f^I_{\phi\phi}(\phi) + \dfrac{K^N_{II}}{K^N_I}\rho^{\lambda_{II}-\lambda_I} f^{II}_{\phi\phi}(\phi)}, \tag{3.36}$$

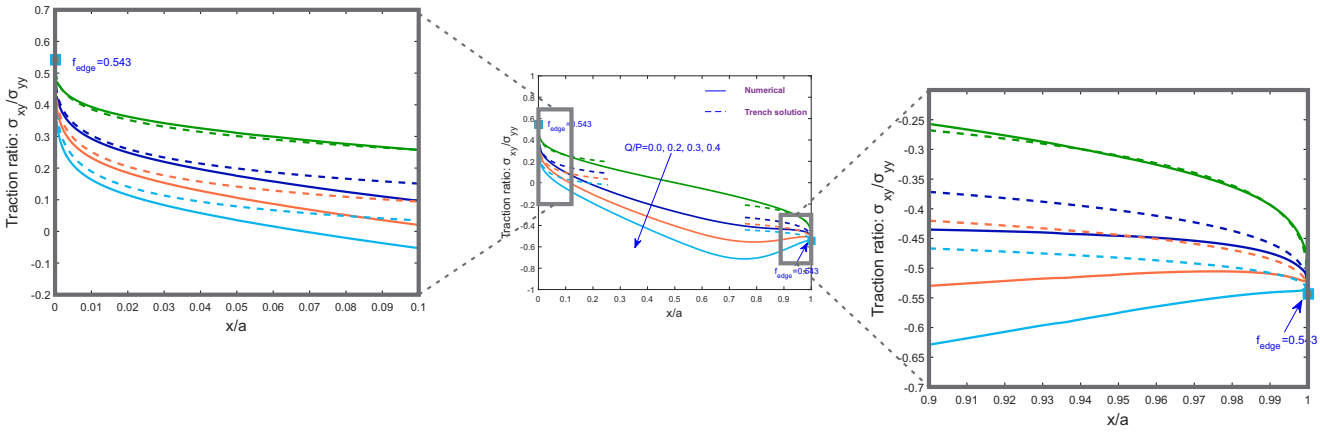


Figure 3.15: Traction ratio response at various Q/P for finite width model, when $d/a = 0.05$. The results are magnified near the LHS and RHS edges for clear vizualisation

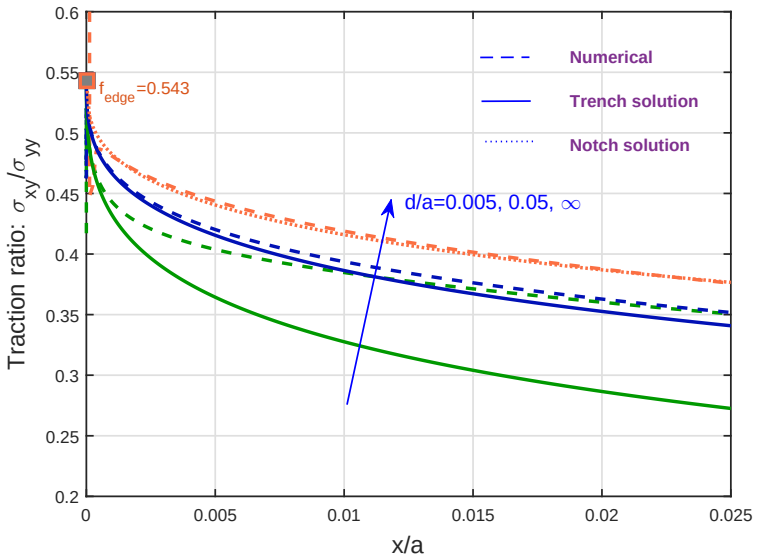


Figure 3.16: Traction ratio response at finite width's $d/a = 0.005, 0.05$ and ∞ for the case where normal load alone is applied

where we note the relevent eigen-functions are $[f_{\rho\phi}(\pi/4)]^{I,II} = [0.3966, 0.238]$ and $[f_{\phi\phi}(\pi/4)]^{I,II} = [0.7303, -1.087]$ and $\lambda_I = 0.544$ and $\lambda_{II} = 0.908$ calculated respectively for a wedge angle corresponding to $3\pi/2$ radians. Now we consider the case when the finite separation is equivalent to a width ratio $d/a = 0.05$. The ratio of shear to direct tractions obtained along the interface is plotted in Figure **??** for all the contact nodes and for $Q/P = 0, 0.2, 0.3, 0.4$. The dotted lines at either end of the interface represents the traction ratio computed using Trench solution, following the procedure mentioned above. Note that the range of relevance of these solutions is expected to be more than that of the Williams solution, which is accurate until a distance equivalent to the width of the finite separation itself ($r \ll d$). The full Trench solution, on the other hand, is valid up to distance r in the interface, where it is relatively large compared to the width d but must be less than the next nearest length dimension, a. Therefore at distances extremely close to the edge, Williams solution will apply and the traction ratio is pinned at ± 0.543. At slightly greater distances from the edge, full Trench solution will be more appropriate. As observed earlier, for the case of $d/a = \infty$, when the shear load reaches 40% of the normal load, slip tends to start from the interior section.

Figure 3.16 illustrates the traction ratio behaviour at different finite widths $d/a = 0.005, 0.05, \infty$ for normal load alone. It is evident from the plot that the traction ratio does not vary significantly between the cases where the separation resembles a crack ($d/a = 0.005$) and the problem where it becomes infinitely wide ($d/a = \infty$). A coefficient of friction equivalent to 0.543 is sufficient to maintain entire interface in adhered conditions. This suggests that the tractions adjoining the contact edge are not very much sensitive to the presence of adjacent socket, when normal loads are applied.

3.8 Conclusion

A comprehensive solution has been obtained to characterise the stress state adjacent to the edge of contact, when a finite clearance is introduced between the block and the trench wall. Before looking at this problem, the contact problem of a square block resting on a half-plane, formulated as a 270^o asymptote has been studied, just to observe the behaviour when the finite width ratio $d/a \longrightarrow \infty$. Comparison with the 'closely fitting' solution reveals that, the isolated block exhibits more stringent requirement for closure condition (full edge contact). A Trench solution has been formulated for finite width problems, which comprises of principles from semi-infinite crack solution in the far field and notch solution in the near tip region. The presence of T-stress components indeed under normal loading conditions, prompted us to derive the corresponding displacement components, which in turn are included in the semi-infinite solution in the form of boundary conditions. The closure condition has been derived in terms of the far field stress intensities K_I and K_{II}. The eigen-vectors for the wedge of included angle 270^o, determine the coefficient of friction ($f > 0.543$) needed for the edge to remain adhered. A study of characteristic traction ratios along the radial direction at various levels of mode mixities has been done.

Again a model very similar to the type square block resting in a trench is considered, but this time with an appreciable but still small side clearance. Initial testing was done to check the consistency of the notch intensity results obtained from trench solution and the reference wedge solution. Normal and shear loads were applied separately and we observed that, for each case, the trench solution converges accurately towards the reference solution at reduced finite widths. In the next phase, the loads were applied together and the notch intensities computed using the trench method were subsequently used to work out the interfacial traction ratio. The results were compared with finite element computed values for the entire interface.

Comparison reveals that the trench solution is extremely accurate near the edge and continue the trend until a distance greater than the width of the clearance and less that the next nearest length dimension. Further, we note that the tractions adjoining the edge of contact are not very sensitive to the presence of adjacent wall, when normal loads are applied.

Chapter 4

Analysis of complete contacts with inclined sides in the form of a trapezium

4.1 Motivation

The vast majority of contact formulations available in the literature focus on incomplete (convex) contacts, and are generally solved using half-plane theory. Recently some progress has been made on the complete contact analysis, where the body not defining the size of the contact is idealised as a half-plane and the components forming the contact are made from the same material. This proves to be a complete and accurate approach to study the edge of contact problems, assuming initially that the near edge is adhered. Williams wedge analysis is used to obtain the tractions in the neighbourhood. The wedge angle chosen is the sum of the angle that the edges defining the contact makes and the angle of the half-plane itself (i.e., an additional π radians)(Flicek et al., [2015][81]). The eigen-vector for the problem reveals the ratio of shear

to direct tractions along the line of interface, so that provided the coefficient of friction f is equivalent to this ratio, the contact interface will be adhered.

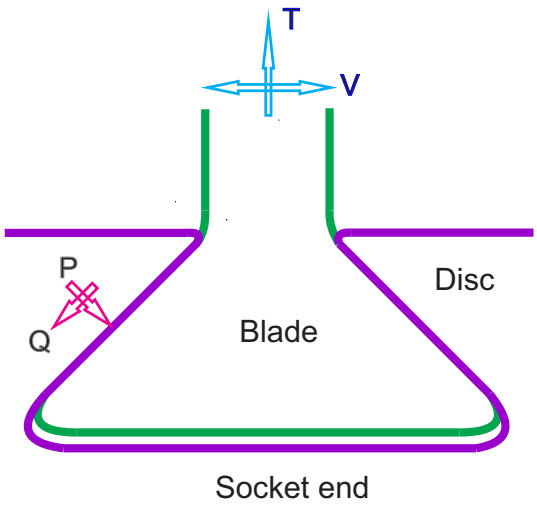


Figure 4.1: Dovetail contact geometry

Recently Arun et al., [2017][82] we looked at a different type of complete contacts, where a square block sits in a trench of approximately the same height as that of the block, but slightly wider than itself, and this has been discussed in Chapters §2 and §3. Contact problems of this kind generate much interest, due to their relevance to practical engineering applications. Typically they are observed in gas turbine engines, where the turbine blades fit into sockets, which conform to the majority of a fir-tree profile. Therefore, a 'wall' of material is located adjacent to the edge of contact, in addition to the half-plane and this markedly affects the response of the contact. A geometrically simpler example of the same kind of contact is observed in fan blade dovetails (refer Figure 4.1), when the root of the blade is located close to the socket end. In contacts with acute corners like this, the edge would invariably slip, because of an unrealistically high coefficient of friction needed to achieve adhered conditions. However this is not the case when the edges defining the contact make a right angle or an obtuse angle.

We have already looked at the case where the contact edge forms a right angle and studied

its behaviour, because that seemed to be the more obvious case to study first. However, we observed an unusual behaviour when the contact edge clearance is very small and which can be treated as a crack when normal loads are applied. Under these conditions, the conventional stress intensities (K_I and K_{II}) due to singular state of stress are negligible and so, unusually, it is the non-singular term in a series solution, the so called *T-stress* governs the behaviour.

In this chapter we study the problem of a trapezium shaped block with the internal edges defining the contact are of angle $\pi/4$ and $3\pi/4$ radians and which again sits in a trench with a depth equivalent to the height of the block itself and slightly wider. The width of the block and its height are both a and that of the clearance either side of the block are d. As with the earlier case of a right angled contact, we assume throughout that (a) the base of the trapezium body is in intimate contact along the entire length of the interface and that the contact normal tractions σ_N are compressive and negative everywhere, and (b) the interface is stuck everywhere and the shear tractions throughout the contact are less than the limiting friction i.e., $|\tau| < -f\sigma_N$. The limitations of these assumptions are probed, so that the conditions under which fretting may be avoided are determined. The asymptotic forms for these internal angles which are applicable near the edges are discussed in the following sections. The procedure needed to develop the framework, follow the same lines as used in the previous case by Arun et al., [2017][82].

4.2 Response of contacts with internal angle $\pi/4$ radians

In order to analyse the response of contacts typically found in a fan blade dovetail, as shown in Figure 4.1, a contact geometry that mimics this configuration was chosen (refer Figure 4.2). The contact defining body is in the form of a trapezium shaped block, with the internal edges defining the contact at an angle of $\pi/4$ radians, and again positioned in a slightly wider trench. We start by considering the case where the edge gaps are negligible and can be idealised as

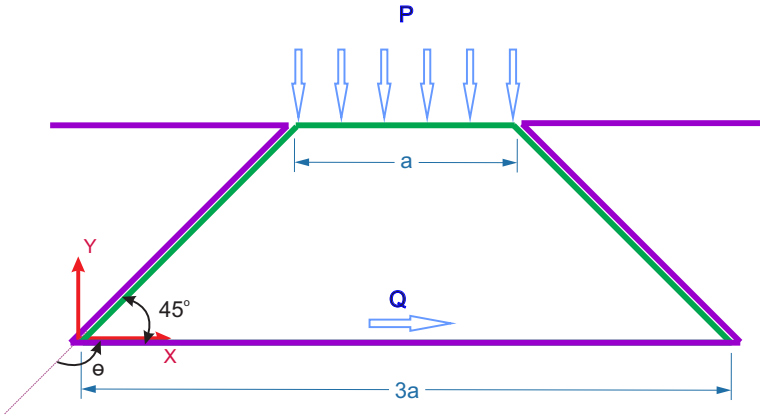


Figure 4.2: Finite description of true crack model with $\pi/4$ radians inclination

cracks. The crack-tip stress field for this problem are well known (Lawn and Wilshaw [1975][75]) and we note that the tractions along the line of interface measured at an angle $3\pi/4$ radians to the crack centreline are,

$$\sigma_{\theta\theta}\sqrt{2\pi r} = \cos^2\left(\frac{3\pi}{8}\right)\left[K_I\cos\left(\frac{3\pi}{8}\right) - 3K_{II}\sin\left(\frac{3\pi}{8}\right)\right] \tag{4.1a}$$

$$\sigma_{r\theta}\sqrt{2\pi r} = \cos\left(\frac{3\pi}{8}\right)\left[K_I\sin\left(\frac{3\pi}{8}\right)\cos\left(\frac{3\pi}{8}\right) + K_{II}\left(1 - 3\sin^2\left(\frac{3\pi}{8}\right)\right)\right]. \tag{4.1b}$$

The traction ratio implied along the interface, adjacent to left hand side edge, is given by,

$$\frac{|\sigma_{r\theta}|}{-\sigma_{\theta\theta}} = \frac{\left|K_I\sin\left(\frac{3\pi}{8}\right)\cos\left(\frac{3\pi}{8}\right) + K_{II}\left(1 - 3\sin^2\left(\frac{3\pi}{8}\right)\right)\right|}{-\cos\left(\frac{3\pi}{8}\right)\left[K_I\cos\left(\frac{3\pi}{8}\right) - 3K_{II}\sin\left(\frac{3\pi}{8}\right)\right]}. \tag{4.2}$$

When the coefficient of friction f is larger than this ratio, the contact will be intimately adhered. Therefore, we can further represent Equation 4.2 in terms of the coefficient of friction f as,

$$f > \frac{\left[1 - 4.41\frac{K_{II}}{K_I}\right]2.42}{7.24\frac{K_{II}}{K_I} - 1}. \tag{4.3}$$

To infer more about the friction requirements, a calibration of the stress intensity factors K_I, K_{II} and σ_0, in terms of the externally applied loads P and Q was done using the commercial finite element program ABAQUS and the relevant results are given here for the left hand side edge,

$$\begin{Bmatrix} \frac{K_I}{\sqrt{2\pi a}} \\ \frac{K_{II}}{\sqrt{2\pi a}} \\ \sigma_0 \end{Bmatrix} = \begin{bmatrix} -0.0027 & 0.0384 \\ 0.0212 & 0.025 \\ -0.156 & -0.0028 \end{bmatrix} \begin{Bmatrix} \frac{P}{a} \\ \frac{Q}{a} \end{Bmatrix}. \tag{4.4}$$

The stress intensity factor ratio K_{II}/K_I can be written in terms of Q/P as follows,

$$\frac{K_{II}}{K_I} = \frac{7.85 + 9.26\frac{Q}{P}}{-1 + 14.22\frac{Q}{P}}. \tag{4.5}$$

Further we can now re-write Equation 4.3, in terms of applied loads as follows,

$$f > \frac{\left[1 - 4.41\left(\frac{7.85 + 9.26\frac{Q}{P}}{-1 + 14.22\frac{Q}{P}}\right)\right] 2.42}{7.24\left(\frac{7.85 + 9.26\frac{Q}{P}}{-1 + 14.22\frac{Q}{P}}\right) - 1}. \tag{4.6}$$

This is plotted in Figure 4.3, where we note that, for realistic coefficients of friction in the range $[0, 1]$, the edge would invariably slip for all load factors between -1 and 1. This clearly violates our initial assumption that the contact remains in intimately adhered and closed conditions.

When the block is placed on an elastically similar half-plane, i.e., when the side clearance is

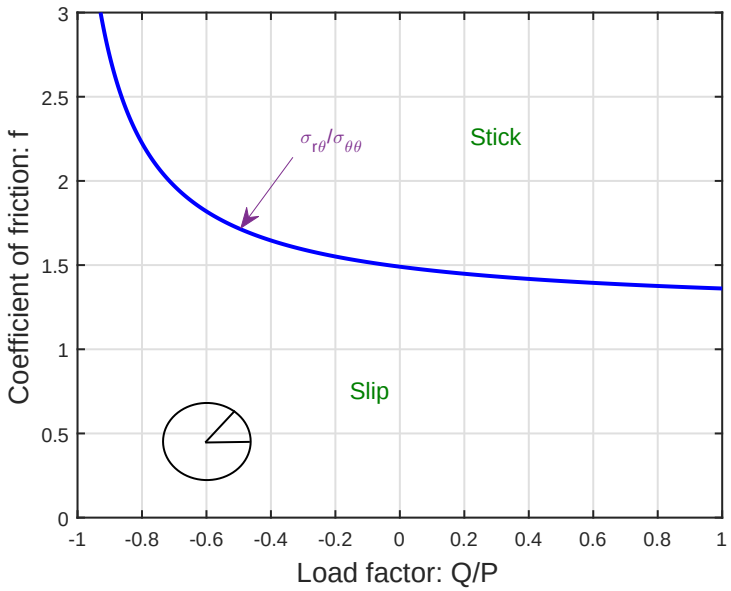


Figure 4.3: Requirement of Coefficient of friction for LHS edge at various external loads for the contact with internal angle $\pi/4$ radians

extremely large, the eigen vectors corresponding to the semi-infinite wedge with included angle 225^o, define the characteristic traction ratio required to maintain the edge in an adhered condition. This can be calculated as 1.34, which nearly coincides with the traction ratio predicted for the closely conforming case (Figure 4.3) but, of course, is still un-realistically high. With the solutions for these extreme cases (negligible clearance and free surface) of geometries violating the initial assumptions, the response for the finite width geometry is nevertheless expected on the same lines and therefore, because it is of little practical value, it has not been pursued with respect to this particular contact angle.

4.3 Response of contacts with internal angle $3\pi/4$ radians

As discussed before in Section 4.1, here we intend to look at the problem of a trapezium shaped body where the internal edges defining the contact makes a much wider angle, $3\pi/4$ radians,

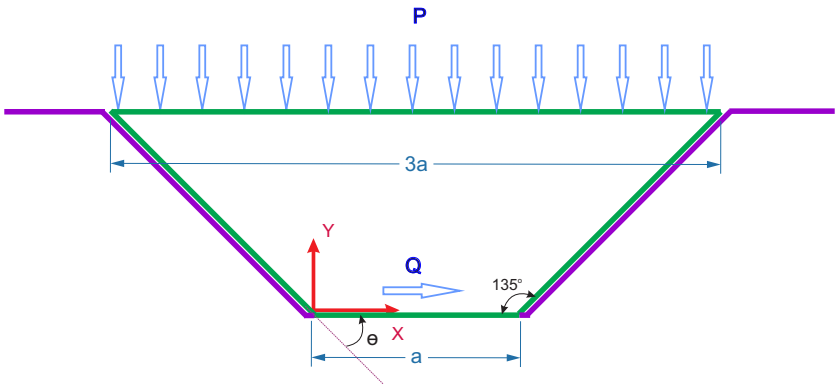


Figure 4.4: Finite description of true crack model with $3\pi/4$ radians inclination

as illustrated in Figure 4.4. We will again be studying the problem for the cases where the edge clearance ratio $d/a \longrightarrow 0, \infty$ and a finite value and explore the conditions that lead to a violation of initial assumptions.

4.3.1 Asymptotic structure: Very small edge clearance

As discussed earlier for the case of right angled contacts (Arun et al., [2017][82]), we start by looking at the case where the width ratio d/a is negligible and the edge gaps may be idealised as cracks, with the flat ends connecting the edges of the block and trench may be ignored. With the origin of the polar coordinate system positioned on the root of the crack-tip, the tractions forming along the line of interface measured at an angle ($\theta = \pi/4$) are,

$$\sigma_N \equiv \sigma_{\theta\theta} = \frac{1}{\sqrt{2\pi r}} \cos^2 \frac{\pi}{8} \left[K_I \cos \frac{\pi}{8} - 3K_{II} \sin \frac{\pi}{8} \right], \tag{4.7}$$

$$\tau \equiv \sigma_{r\theta} = \frac{1}{\sqrt{2\pi r}} \cos \frac{\pi}{8} \left[K_I \sin \frac{\pi}{8} \cos \frac{\pi}{8} + K_{II} \left(1 - 3 \sin^2 \frac{\pi}{8} \right) \right]. \tag{4.8}$$

Before making any general inferences, we obtain the calibrations for the crack-tip stress intensity factors K_I, K_{II} and the T-stress component σ_0 in terms of the applied loads P and Q. These were obtained by the finite element method and are given for the left hand side crack

as,

$$\begin{Bmatrix} \frac{K_I}{\sqrt{2\pi a}} \\ \frac{K_{II}}{\sqrt{2\pi a}} \\ \sigma_0 \end{Bmatrix} = \begin{bmatrix} -0.3991 & 0.5509 \\ 0.2733 & 0.3467 \\ -0.9952 & -0.0716 \end{bmatrix} \begin{Bmatrix} \frac{P}{a} \\ \frac{Q}{a} \end{Bmatrix}. \tag{4.9}$$

The requirement that the edge of contact remains closed is that the normal tractions σ_N remains compressive i.e., $\sigma_N < 0$. The state of closure of the contact is mentioned in a compact notation in the $K_I - K_{II}$ space in Figure 4.5, after taking into account the individual signs of the stress intensity factors. The first two quadrants represents the combination of the stress intensities K_I and K_{II} that lead to the closure of the contact, while the remaining ones imply an open condition and this can be summarised as follows,

$$K_{II}/K_I > 0.804 \ \forall \ K_I > 0, K_{II} > 0 \tag{4.10a}$$

$$K_{II}/K_I < 0.804 \ \forall \ K_I < 0, K_{II} > 0. \tag{4.10b}$$

From the calibrations we note that the application of a normal load alone induces a negative value of K_I, with the ratio $K_{II}/K_I = -0.685$. The vector corresponding to this gradient is shown in Figure 4.5. It is clear from the plot that application of positive shear force, Q, tends to rotate the radial vector clockwise and that it moves from quadrant II to I, with K_I turning positive. Separation is expected to occur when the normal tractions $\sigma_N > 0$, i.e., when the ratio K_{II}/K_I is less than the ratio 0.8 (while both stress intensities are positive). This occurs in practice for the particular geometry shown in Figure 4.4 when the load factor $Q/P > 6.19$. As a consequence, we see that, for realistic coefficient of friction in the interval [0,1], corner separation does not occur. However, the application of negative shear tends to rotate the vector in the anti-clockwise direction and separation is expected to occur when the ratio K_{II}/K_I is again greater than 0.8, when both stress intensities are separately negative. In practice, the

edge separation never occurs, since the application of negative shear will, in turn, make the interface more compressive and the edge of contact will always be closed.

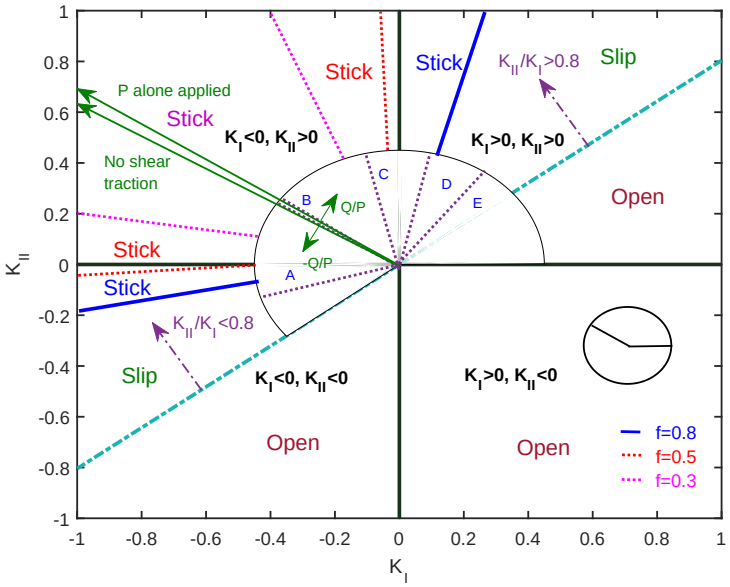


Figure 4.5: Specification of contact conditions for the LHS edge in $K_I - K_{II}$ space to represent the slip/separation behaviour

We have remarked earlier that, separation must be preceded by slip. The point of first slip might occur at any point along the interface. The traction ratio implied along the line of interface for the left hand side edge, which forms the basis for the no slip condition is given by,

$$\frac{\tau(x)}{p(x)} \equiv -\frac{|\sigma_{r\theta}|}{\sigma_{\theta\theta}} = \frac{\left|K_I \sin\frac{\pi}{8}\cos\frac{\pi}{8} + K_{II}\left(1 - 3\sin^2\frac{\pi}{8}\right)\right|}{-\cos\frac{\pi}{8}\left[K_I\cos\frac{\pi}{8} - 3K_{II}\sin\frac{\pi}{8}\right]}, \tag{4.11}$$

which may be further written as,

$$\frac{\tau(x)}{p(x)} = \frac{\left(1 + 1.59\frac{K_{II}}{K_I}\right)0.421}{\left(-1 + 1.244\frac{K_{II}}{K_I}\right)}. \tag{4.12}$$

Provided that the coefficient of friction is as big as this ratio $\frac{\tau(x)}{p(x)}$, the edge will certainly be adhered. This is given in Figure 4.5, where the coefficients of friction needed for adhered conditions are given as a function of K_{II}/K_I, within the region of the plot corresponding to contacts in the fully closed condition. When a normal load, P, alone is applied, a very small coefficient of friction equivalent to 0.02 is sufficient to ensure adhered conditions along the edge. When a positive shear is applied, the vector K_{II}/K_I starts from the second quadrant and the coefficient of friction required increases and lies in the interval [0.3,0.5]. We expect that as the separation condition is approached, the traction ratio increases very much and is because the contact pressure is reducing in magnitude. With a further increase in the load the vector now moves to the first quadrant, with the coefficient of friction needed to ensure adhesion increasing to a magnitude of 0.8 and eventually achieves separation when $K_{II}/K_I < 0.8$ after a momentary slip. When the shear force is increased in a negative sense, the coefficient of friction required decreases initially, with the shear tractions vanishing completely at a K_{II}/K_I ratio of -0.63. The shear tractions reverse direction, as the applied loads are increased further and the coefficient of friction required for adhered conditions increases continuously until the practical limit of the load factor -1.

Now consider the finite contact problem defined in Figure 4.4. The stress intensities caused by the applied external loads are known through the calibration, so the immediate objective here is to formulate an expression for the coefficient of friction in terms of the applied loads Q and P. This can be obtained by substituting the stress intensity ratio K_{II}/K_I calculated from Equations 4.9 in 4.12, to obtain the relevant form which represents the coefficient of friction

needed for stick conditions and is,

$$f > 0.421 \left[\frac{1 + 1.59 \left(\dfrac{1 + 1.259\frac{Q}{P}}{-1.4497 + 2.001\frac{Q}{P}} \right)}{-1 + 1.244 \left(\dfrac{1 + 1.259\frac{Q}{P}}{-1.4497 + 2.001\frac{Q}{P}} \right)} \right]. \tag{4.13}$$

This response is shown in Figure 4.6, where the traction ratio is plotted as a function of the

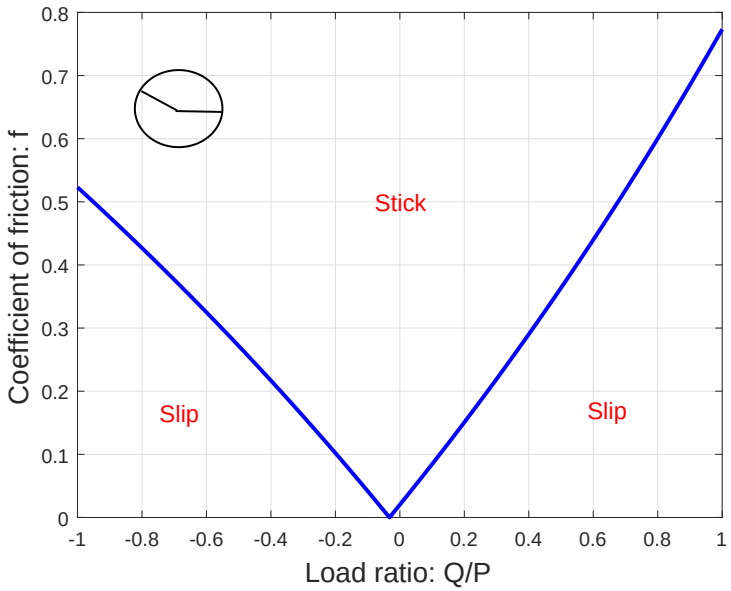


Figure 4.6: Variation of coefficient of friction at different external load for the LHS edge with Internal angle $3\pi/4$ radians

load factor Q/P. When a normal load alone is applied i.e., $Q/P = 0$, a coefficient of friction of at least 0.02 is needed for adhered conditions. At this instant the friction tends to act outwards on the block with the shear traction acting in the positive direction, as illustrated in the free body representation of the contact tractions in Figure 4.7. When the shear force is applied in the positive direction, the shear traction increases and therefore the minimum coefficient of friction needed for stick conditions increases. On the other hand, when the shear force is

applied in the negative direction, the coefficient of friction decreases initially, and reaches zero at a load factor $Q/P = -0.03$. Further increase in shear force causes the shear traction and the frictional force to change direction with eventual increase in coefficient of friction. The complete kinematics defined above can be inferred in the plot of the traction response for the entire length of the contact interface as given in Figure 4.8.

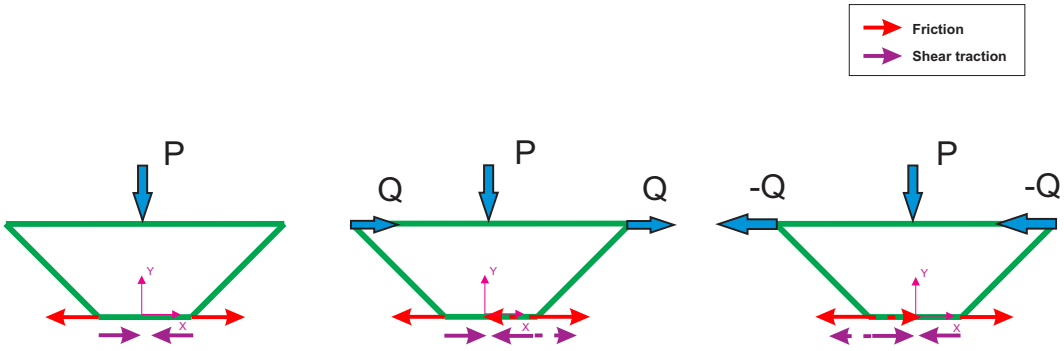
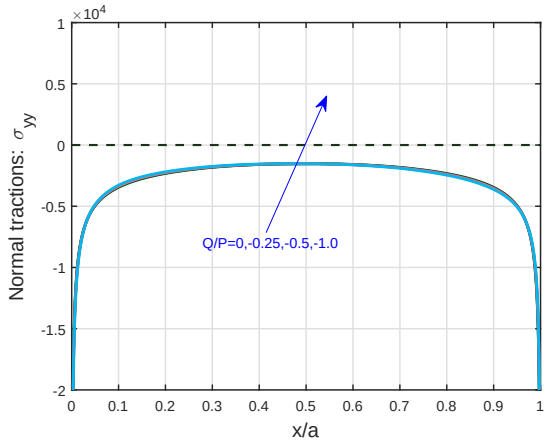


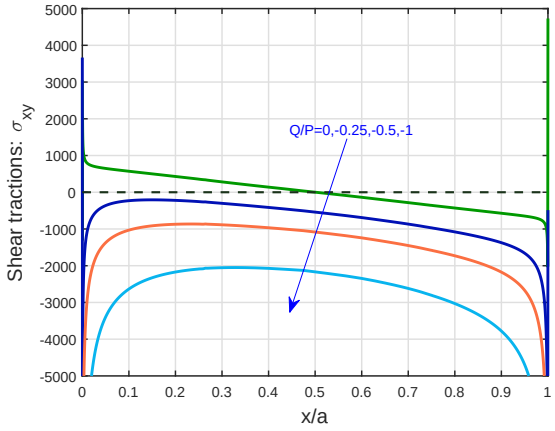
Figure 4.7: Free body representation of contact tractions for a finite true crack model with Internal angle $3\pi/4$ radians

4.3.2 Asymptotic structure: Very large edge clearance

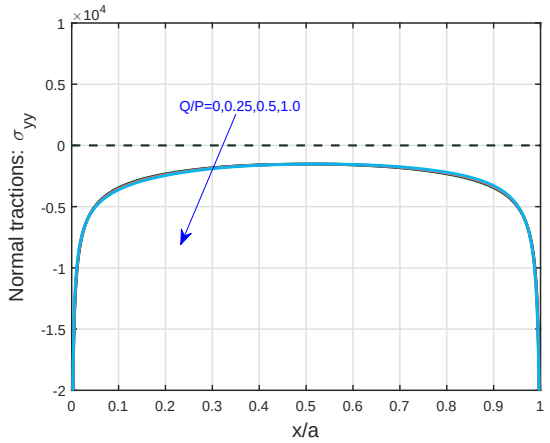
Section §4.3.1 described the behaviour of the edge of contacts where the side clearance is very small i.e., the width ratio $d/a \longrightarrow 0$. When these circumstances occur, the separations either side of the block can be considered as a crack and the semi-infinite crack eigen-solution can be used to describe the tractions adjoining the edge region. This implies that the characteristic solution depends equally on the symmetric and anti-symmetric solutions, each of which is square root singular. When the side clearance is not negligible and assumes some finite value, a new mode of calculation is required, especially when the observation point is very close to the edge, compared to the actual width of the separation d. As defined earlier in Arun et al., [2017][82], the semi-infinite wedge solution developed by Williams [1952][54] can be used to define the stress state adjoining the corner for an included angle 2α, which for this particular



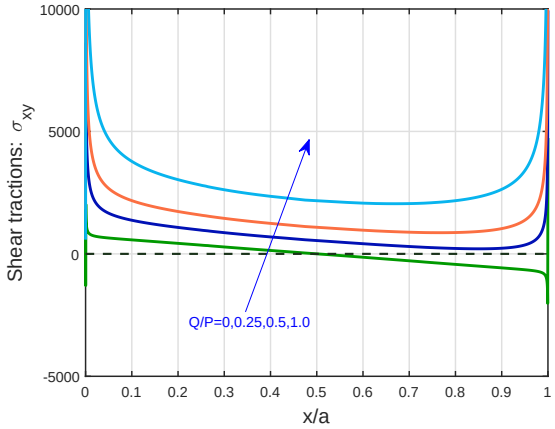
(a) Normal traction response at negative shear loads



(b) Shear traction response at negative shear loads



(c) Normal traction response at positive shear loads



(d) Shear traction response at positive shear loads

Figure 4.8: Finite element simulation of contact tractions for the geometry with Internal angle=$3\pi/4$ radians and $d/a \longrightarrow 0$

case of contact (refer Figure 4.4) given by $\pi + 3\pi/4 = 7\pi/4$ radians. Note that this solution continues to apply when the finite separation is increased and so it is pertinent to look at the extreme opposite case when the block is positioned at a remote location, i.e., when the ratio $d/a \longrightarrow \infty$. When this occurs, the problem can be treated as the case where a trapezium block is simply pressed on to a surface of an elastically similar half-plane and is shown in Figure 4.9.

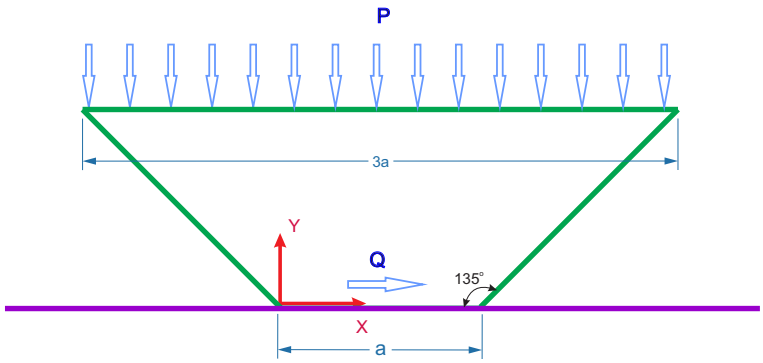


Figure 4.9: Representation of a trapezium block in contact with a half-plane when the ratio $d/a \longrightarrow \infty$

Recall from Equation 3.1, the state of stress in the near vicinity of the edge as defined by the semi-infinite wedge solution,

$$\sigma_{ij}\left(\rho,\phi\right) = K_I^N \rho^{\lambda_I - 1} f_{ij}^I\left(\phi\right) + K_{II}^N \rho^{\lambda_{II} - 1} f_{ij}^{II}\left(\phi\right), \tag{4.14}$$

where the first term in the series corresponds to the symmetric part of the solution and the second term represents the anti-symmetric part. The eigen-values λ_I and λ_{II} for this particular case of included angle $7\pi/4$ radians are 0.505 and 0.659 respectively. If we choose an observation point very close to the corner, we expect the dominant term to be the symmetric solution. The eigen-vector for the symmetric solution then defines the characteristic traction ratio needed to maintain the edge in adhered conditions and is given by,

$$\frac{\tau(x)}{p(x)} \equiv -\frac{|\sigma_{\rho\phi}|}{\sigma_{\phi\phi}} = -\frac{f_{\rho\phi}^I\left(\phi\right)}{f_{\phi\phi}^I\left(\phi\right)} = 0.213 \tag{4.15}$$

Further, we note the calibrations for the notch stress intensity factors K_I^N and K_{II}^N in terms of

the applied loads P and Q for this case can be given as,

$$\left\{ \begin{array}{c} K_I^N(a)^{\lambda_I - 1} \\ K_{II}^N(a)^{\lambda_{II} - 1} \end{array} \right\} = \left[\begin{array}{cc} -0.572 & 0.307 \\ 0.341 & 0.910 \end{array} \right] \left\{ \begin{array}{c} P/a \\ Q/a \end{array} \right\}. \tag{4.16}$$

The condition for edge closure requires that $K_I^N < 0$ and from **??** we can represent the same in terms of the applied loads P and Q as,

$$Q/P < 1.87, \tag{4.17}$$

so that slip must precede separation. A quick comparison with the closely fitting solution defined in Section §4.3.1 (for the case of d/a=0) reveals that the isolated block is more resistant to avoiding edge separation and so slip will still occur for realistic coefficients of friction. Similarly, within the limit load factors $-0.4 \lesssim Q/P \lesssim 0.3$, the coefficient of friction required to avoid slip for the isolated block (i.e., 0.213), exceeds the respective magnitude for the other case, where there is a negligible clearance adjacent to the contact. Note that, all the above analytical calculations are performed exclusively for the LHS edge of the contact.

4.3.3 Asymptotic structure: Small edge clearance

As discussed before for the case of the right angled contact (Arun et al., [2017][82]), we now have a geometry where the side clearance is small, but finite, and the intention here is to predict what happens at observation points moderately close to the edge. In order to obtain a solution, we again consider the problem of a semi-infinite trench located in an infinite space as shown in Figure 4.10. The root of trench is positioned obliquely at an angle $3\pi/4$ radians with the contact interface, so that it corresponds exactly to the geometry of the bottom of

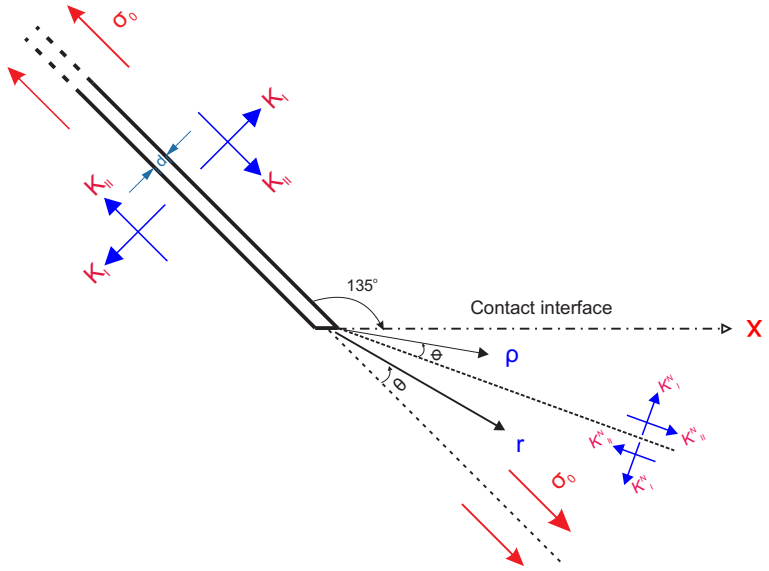


Figure 4.10: Semi-infinite description of a trench model with a finite separation for the contact with Internal angle $3\pi/4$ radians

the side clearance slots shown in Figure 4.11. The inner solution is described by the semi-infinite wedge solution when the observation point is very close to the edges, i.e., located within a distance equivalent to the finite width d and characterized by the notch intensities $K_I^N$and K_{II}^N measurable along the bisector (short dashed line) of the wedge asymptotic region with total included angle $7\pi/4$ radians. The remote (outer) solution is that experienced by the semi-infinite crack and consistent with a square root singular response. The input to the model is realised in terms of the crack-tip eigen solutions, with the stress intensities K_I and K_{II} contributing to the singular terms and T-stress σ_0 representing the non-singular term. These parameters in-turn can be measured along the centre line (long dashed line) of the crack asymptotic region in the outer boundary.

The asymptotic model was constructed in the commercial finite element program ABAQUS, so as to obtain a solution for the representative problems shown in Figure 4.10. As illustrated in Figure 4.12a, a circular type model was created with the outer boundary located at a distance $R = 100d$ from the trench root region. A finely refined mesh was generated near the vicinity of

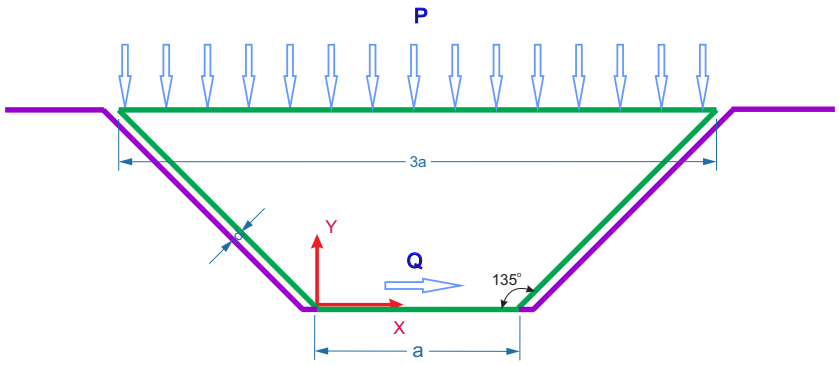


Figure 4.11: Finite description of a contact model with a finite edge clearance d/a for the Internal angle $3\pi/4$ radians

the tip region, so as to achieve an uniform stress gradient across the elements to ensure a good convergence of the stress intensity parameters. The crack-tip loading is realised in the form of imposed displacements along the outer boundary, so as to obtain a controlled solution, with the corresponding displacement fields defined in Section §3.4.

The notch stress intensity factors are calculated using Equations 3.8 and 3.9 and the matrix of coefficients denoting the generalised stress intensity factors are calculated for the right hand corner as,

$$\left\{ \begin{array}{c} K_I^N d^{\lambda_I - 1} \\ K_{II}^N d^{\lambda_{II} - 1} \end{array} \right\} = \left[\begin{array}{ccc} 0.938 & -0.547 & 0.0616 \\ 0.211 & 0.932 & -0.308 \end{array} \right] \left\{ \begin{array}{c} \dfrac{K_I}{\sqrt{2\pi d}} \\ \dfrac{K_{II}}{\sqrt{2\pi d}} \\ \sigma_0 \end{array} \right\}. \tag{4.18}$$

We noted, earlier, that the requirement for closure conditions at the edge of contact is $K_I^N < 0$, and therefore we can represent the same in terms of the crack-tip stress intensity factors K_I and K_{II} as,

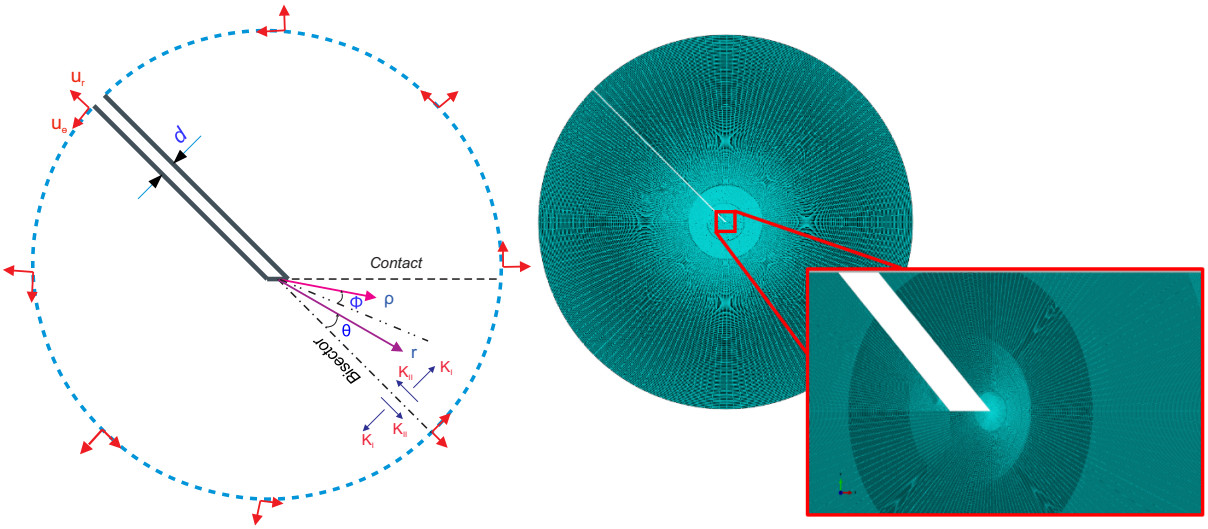
$$K_{II}/K_I > 1.71 \ \forall \ K_I > 0, K_{II} > 0 \tag{4.19a}$$

$$K_{II}/K_I < 1.71 \ \forall \ K_I < 0, K_{II} > 0 \tag{4.19b}$$

Collocating this solution with the geometry for a finite true crack model represented in Figure 4.4, we obtain the condition for no separation in terms of the applied loads Q and P, as,

$$Q/P < 1.6. \tag{4.20}$$

The characteristic behaviour of the ratio of tractions along the line of interface for observation points which are located at varying distances from the edge and measured at an angle $\pi/4$ radians from the crack bisector is given in Figure 4.13. Here, we are interested in the traction ratio for the semi-infinite geometry shown in Figure 4.10. Further, we note that when the



(a) Asymptotic representation of a finite width model

(b) Representation of FE model used to compute the trench solution

Figure 4.12: Trench solution for the contact with Internal angle $3\pi/4$ radians

observation point is located at a distance such that $r/d \gg 1$, we expect to recover the solution for a semi-infinite crack and this can be observed in Figure 4.13, where the remote traction ratios for stress intensity ratios $K_{II}/K_I = 0$ and 0.1 reach the characteristic pure mode I and mode II values of 0.421 and 0.538 respectively. The traction ratio at these remote locations are given in Figure 4.14, and are dependent on the ratio K_{II}/K_I. As the edge is approached i.e., when the

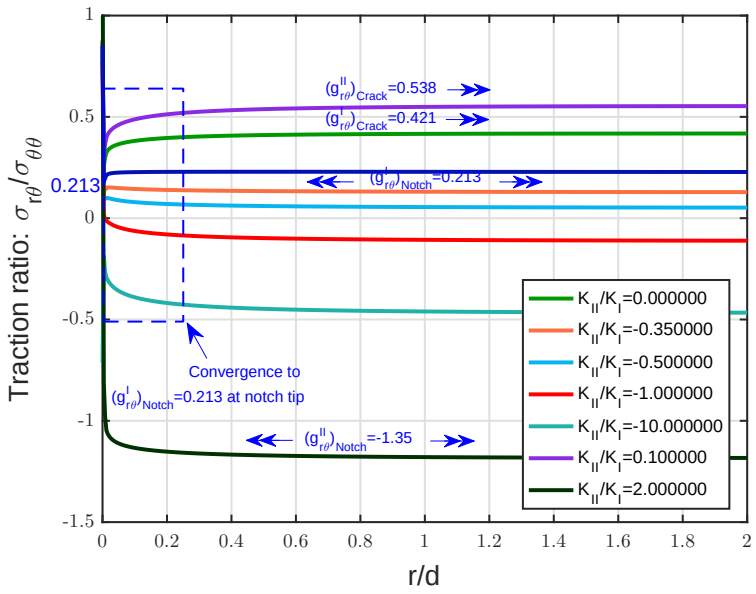


Figure 4.13: Traction ratio response for the semi-infinite geometry at mixed mode conditions for the Internal angle $3\pi/4$ radians

observation point is close to the notch tip $r/d \ll 1$, wedge solution corresponding to an internal angle $3\pi/4$ radians applies and the traction ratio converges to the characteristic value 0.213. It is clear from the plot that for most of the stress intensity ratios, the condition for adhesion is more stringent in the remote region than it is for the edge region. When $K_{II}/K_I = -0.35$, uniform mode I conditions are observed throughout the interface, with a coefficient of friction of 0.213 is sufficient for adhered conditions at all the nodes along the interface. Further, we note that, when $K_{II}/K_I = 2$, mode II conditions are observed throughout the interface with the coefficient of friction required for adhered conditions being 1.35.

Figure 4.15 shows the response of the internal length parameter d_0/d as a function of the ratio K_{II}/K_I, when it is varied within the interval $[-4, 2]$. The calculation of d_0/d is carried out in a manner similar to what has been done for the case of right angled contact and can be

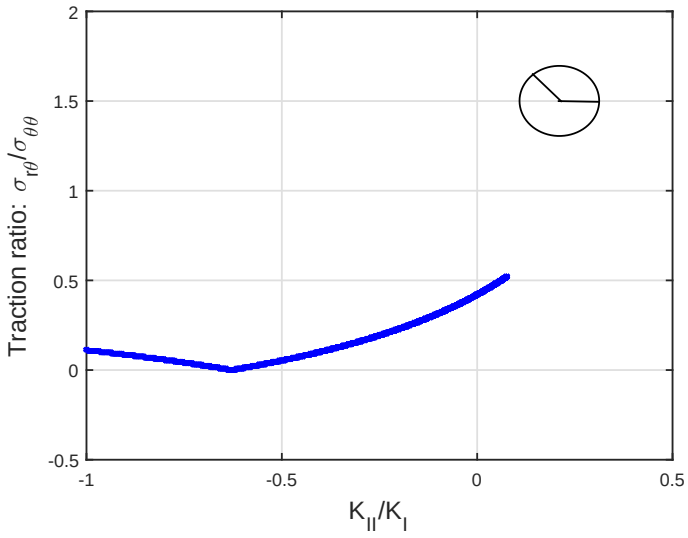


Figure 4.14: Traction ratio response for a semi-infinite crack at different ratio's of K_{II}/K_I

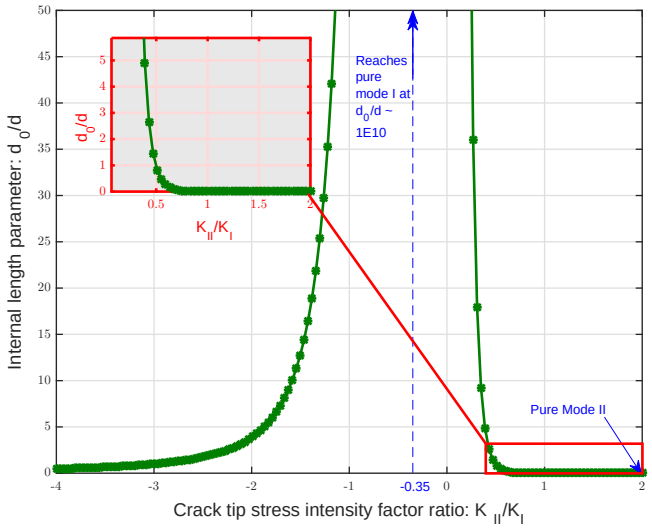


Figure 4.15: Response of internal length parameter d_0 at different stress intensity ratio's of K_{II}/K_I

given as,

$$\frac{d_0}{d} = \left[\frac{0.211 + 0.932\frac{K_{II}}{K_I}}{0.939 - 0.547\frac{K_{II}}{K_I}}\right]\left(\frac{1}{\lambda_I - \lambda_{II}}\right). \tag{4.21}$$

From the plot it is clear that pure mode I and mode II conditions can be obtained at the stress

intensity ratios $K_{II}/K_I = -0.35$ and 2, when the internal length parameter ratio d_0/d reaches ∞ and 0 respectively. The finite element results shown in Figure 4.13 predicts similar results, where it reaches the characteristic mode I and mode II traction ratio's 0.213 and 1.35, at the respective stress intensity ratios.

4.4 Initial observations of overall contact behaviour

The three punch geometries with internal angles $\pi/2$, $3\pi/4$ and $\pi/4$ radians, along with the contacting solids in which they sit, either a half-plane or a nearly conforming socket is illustrated in Figure 4.16. The asymptotic procedures described in Sections §2.4.1, §3.2, §4.2 and §4.3 for these geometries are applied to the edge of contact and results were generated. An initial analysis was performed to assess the sensitivity of the results with respect to the following criteria: (1) shape of the punch (2) proximity of the adjacent material (3) applied external loads (4) spatial coordinates along the interface, and the results obtained are articulated in the following sections.

4.4.1 Motivation

In every case, the contacting pair was modelled as a monolith using the finite element program ABAQUS, incorporating the displacement continuity along the interface, i.e., the material is continuous across the contacting interface. The side flanks are maintained traction free, so that the possibility of side contact is positively excluded. The cases where the side clearance is negligible has been modelled as a crack with the computations performed mainly through the ABAQUS contour integral analysis. A uniform pressure with a total force P, is applied along the upper face of the punch, followed by a shear force Q. The shear force was applied to the upper edge of the punch together with a moment rendering it statically equivalent to one

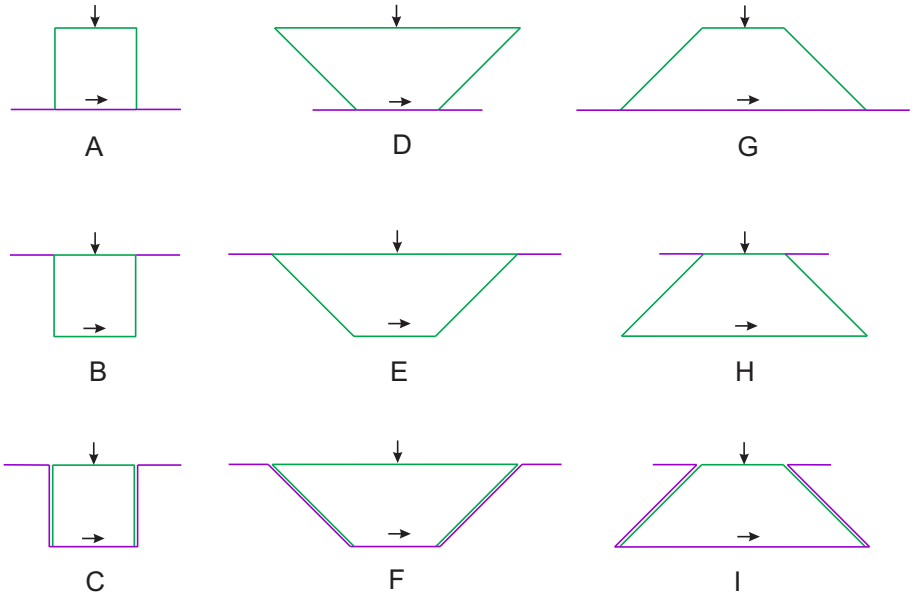


Figure 4.16: Representation of different configurations of contact with Internal angles $\pi/2$, $3\pi/4$ and $\pi/4$ radians respectively

exerted at the plane of contact.

The punch is symmetrical with respect to the vertical axis and therefore it produces a symmetrical contact pressure and anti-symmetric shear traction distribution, under application of normal load P. Similarly, the application of a shear load Q along the plane of interface produces symmetrical shear tractions and an anti-symmetric normal contact pressure.

4.4.2 Analysis of contact behaviour for extreme geometries

The traction ratio behaviour for punches with internal angles of $3\pi/4$, $\pi/2$, and $\pi/4$ radians are given in Figures 4.17, 4.18 and 4.19 respectively. Two extreme cases of edge separation has been considered for the initial observations. The punch which is isolated and in contact with a half-plane i.e., when $d/a \longrightarrow \infty$ is shown in dotted lines, while the other extreme case when the punch is present in a closely conforming socket ($d/a \longrightarrow 0$) is shown in continuous lines. These sets of plots reveals several interesting features. In each case, we note that, except

for the regions close to the edges, the traction ratios across the entire length of the interface are remarkably independent of the adjacent material, especially under a normal load alone, and the additional divergence in the presence of a shear force is quite modest. On the other hand, the internal angles of the contacting edges seems to have a significant effect on the overall behaviour of the tractions, as the general characteristics of the plot are quiet different.

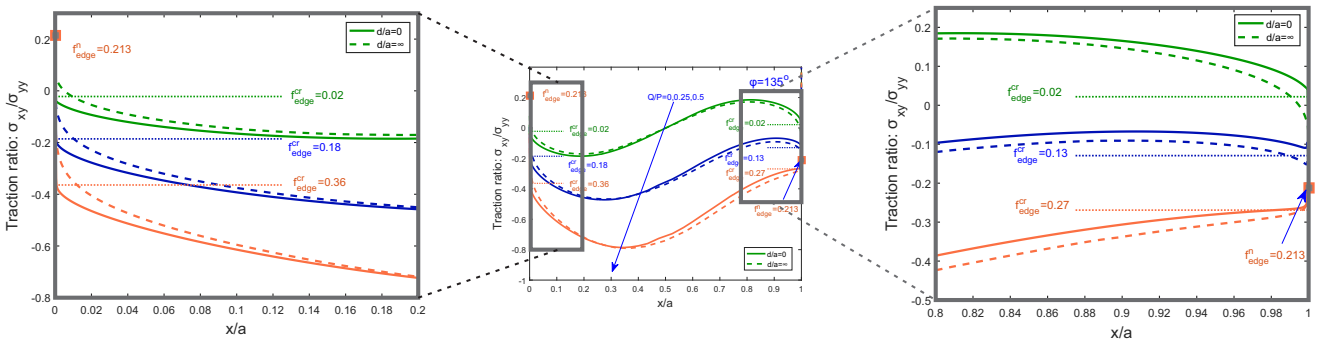


Figure 4.17: Plot of traction ratio behaviour for the extreme geometries ($d/a = 0$ and ∞) of contact with Internal angle $3\pi/4$ radians

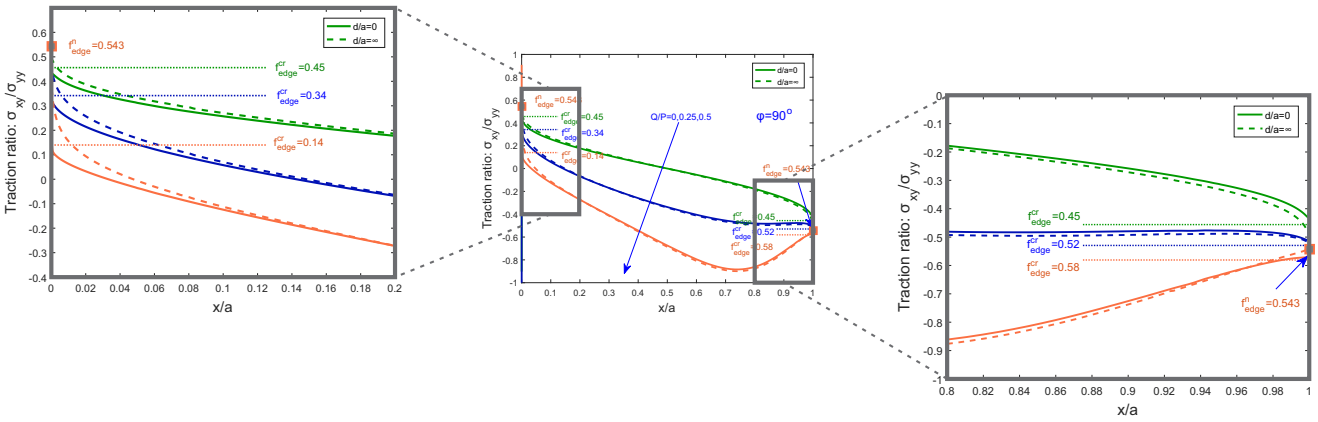


Figure 4.18: Plot of traction ratio behaviour for the extreme geometries ($d/a = 0$ and ∞) of contact with Internal angle $\pi/2$ radians

Now consider the case when the internal angle is obtuse ($3\pi/4$ radians) and the block is located on a half-plane ($d/a \longrightarrow \infty$). From Figure 4.17, we note that a very small coefficient

of friction is needed to ensure adhered conditions at the edges (only 0.213 as obtained from Williams solution for a semi-infinite wedge of internal angle $7\pi/4$) and consequently found that the internal maxima in the traction ratios are very close to this under a normal load alone. The application of even a modest shear force causes an internal maximum to exceed the edge values and may give rise to interior slip. The traction gradients close to the edges are extremely steep, so that at negligible distances from the edge the block tends to 'spread' and as soon as the observation point reaches a distance of say $a/50$, the shearing tractions reverse sign. On the other hand, when the side clearance is extremely small ($d/a \longrightarrow 0$), the crack model applies and only tiny shearing tractions are present at the contact edges under a normal load alone, requiring a coefficient of friction of 0.02 for stick conditions.

When the punch edge forms a right angle, the closeness between the solutions of the extreme cases is even more apparent (refer Figure 4.18). However unlike the previous case, here there is no turning point in the traction ratio at normal loads. From Williams asymptotics the coefficient of friction needed to maintain adhered conditions is calculated as 0.543 and this is a sufficient requirement until Q/P exceeds a value of 0.25. We note that for the other extreme of the confinement i.e., when $d/a \longrightarrow 0$, the coefficient of friction needed to prevent slipping, as calculated from the crack asymptotics is about 0.52, for the same magnitude of load factor say $Q/P = 0.25$.

Finally we consider the case when the internal punch angle is $\pi/4$ radians (refer Figure 4.19). Unlike the previous cases, we observe approximately a linear variation of the traction ratio across the whole of the contact interface. The effect of the presence of adjacent material, though, has a negligible effect. From Figure 4.3, we note that the traction ratio for this case of internal angle is un-realistically high to prevent edge slip (1.34 for remote block case and higher still with adjacent material present). Further, we observe that, as the edge of contact is approached the normal traction falls away quickly. Separation of the edge occurs at a very small

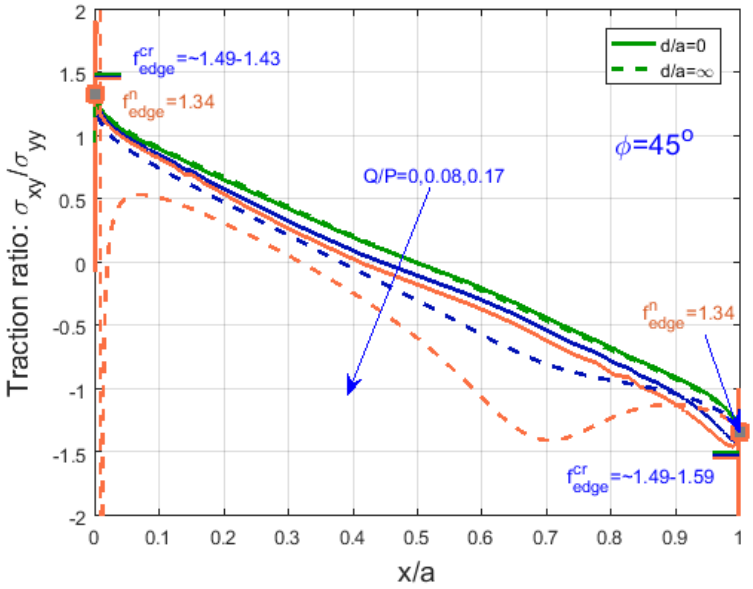


Figure 4.19: Plot of traction ratio behaviour for the extreme geometries ($d/a = 0$ and ∞) of contact with Internal angle $\pi/4$ radians

value of shear force, $Q/P > 0.138$, in the case of a punch on a half-plane, and $|Q|/P > 1.09$ in the case of a small side clearance problem, even if all slip is somehow averted.

The description above reveals the general trends observed in representative problems in Figure 4.16. It seems obvious that the tractions away from the edges are controlled very much by the overall shape of the punch and the applied load distribution. But, nevertheless, it is notable that the very different domain shapes of the contacting bodies do not have the sort of influence on the tractions which one might anticipate.

4.5 Discussion of results

The traction ratio results for the punch with an obtuse internal angle ($3\pi/4$ radians) have been discussed in Section 4.4.2 for geometries with extreme limits ($d/a \longrightarrow 0$ and ∞) of edge separation. We have further noted that the results relative to interior of the contact are not

very sensitive to the presence of adjacent material, with any variation occurring mainly near the neighbourhood of the edge, although to a lesser extent. In fact, this behaviour is applicable to geometries with all three internal angles under consideration. It would be interesting to see how the results for a finite width problem varies between these extreme limits and how relevant the trench method is in characterising the behaviour of the contact.

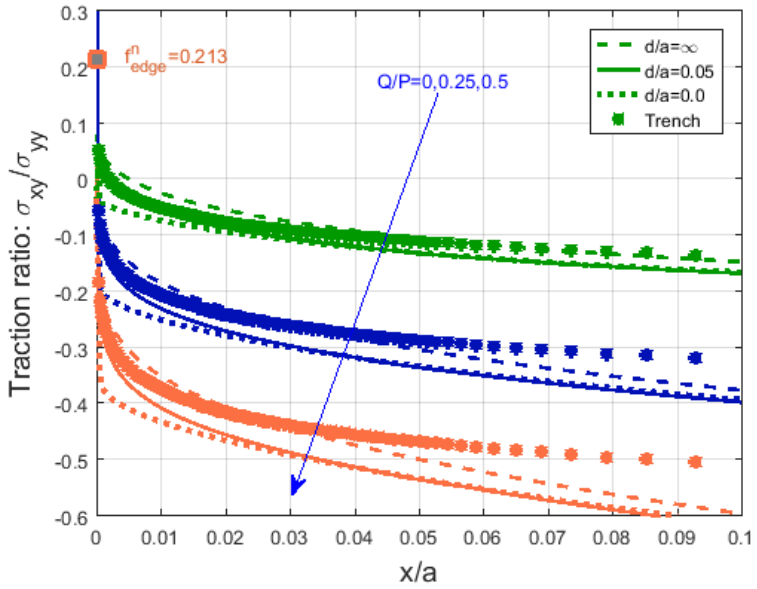
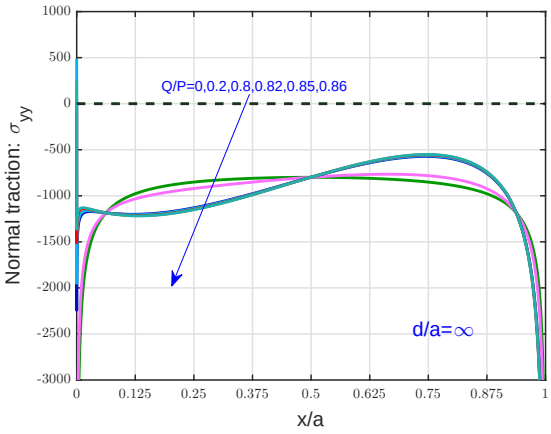
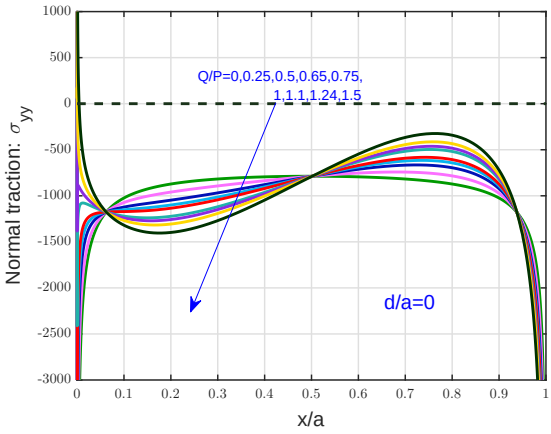


Figure 4.20: Traction ratio results magnified near LHS edge, to reveal the variation of Trench results (for $d/a = 0.05$) compared to the extreme geometry results. Internal angle considered: $3\pi/4$ radians

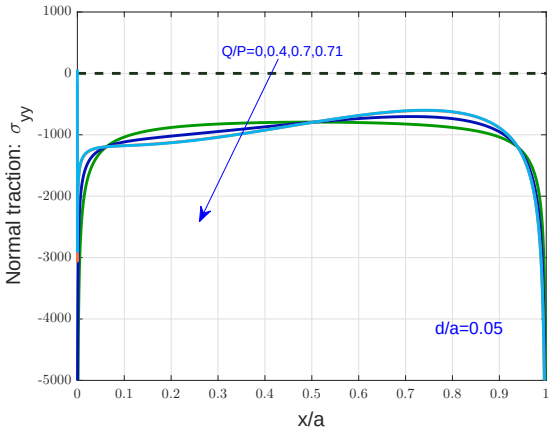
Figure 4.20 reveals a three way comparison of the traction ratio results along the entire length of the interface of monolithic finite element model with width ratio $d/a = \infty, 0.05$ and 0.0. At the edge the traction ratio for the finite width model remains pinned at a value of 0.213, and coincides with the results for $d/a = 0$ in the interior region. We note that the trench method gives an accurate prediction of the stresses along the transition region when $x/a \sim 0.05$, especially for the normal load alone case, although with marginal difference at shear loads. This clearly is different from the remote block model, which still can be used to solve a finite width problem, but with poorer accuracy in the transition region.



(a) Edge width ratio $d/a = \infty$. Edge separation occurs at Q/P(Analytical,FE)=(0.85,0.86)



(b) Edge width ratio $d/a = 0$. Edge separation occurs at Q/P(Analytical,FE)=(1.16,1.1)



(c) Edge width ratio $d/a = 0.05$. Edge separation occurs at Q/P(Trench,FE)=(0.71,0.71)

Figure 4.21: Normal traction behaviour for finite model at various edge widths $d/a = \infty, 0$ and 0.05 for punch angle $\pi/2$ radians

Another valuable piece of information that can be obtained from the trench solution is the edge closure condition, which for this case can be given as $Q/P < 1.6$. The closure condition for the geometries with edge separation $d/a = 0$ and ∞ can be recalled as $Q/P < 6.19$ and $Q/P < 1.87$ respectively. This shows that the narrow edge gap model separates at lower shear

loads than other models. It is further evident that for realistic coefficients of friction, the edge would always be in intimately closed and adhered conditions.

The contact with right angled punch follows the same separation trend as the current one, but nevertheless might suffer some slip before achieving separation at realistic coefficient of frictions. The closure criteria for these contacts can be referred from the configurations A', 'B' and 'C' respectively in Table 4.1. The normal tractions generated by the finite element analysis predict similar results (refer Figure 4.21) and confirms the closure criteria calculated by all three asymptotes namely the semi-infinite wedge, semi-infinite crack and the semi-infinite trench to a good degree of accuracy.

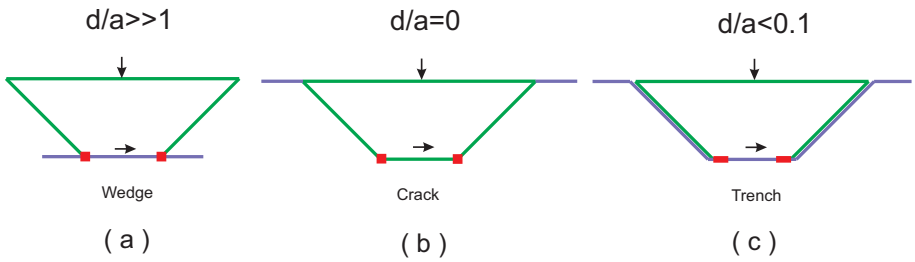


Figure 4.22: Contact models with $3\pi/4$ radians inclination, showing the region of relevance for the wedge, crack and trench asymptotes

4.6 Conclusion

Asymptotic forms for contact geometries with internal angle $\pi/4$ radians had been discussed, partially for the cases of negligible and infinite side clearances. Eigen solutions for the edges reveal a requirement of un-realistic high coefficient of friction for adhered conditions and edge slip is therefore unavoidable for geometries incorporating this inclination. On the other hand, an elaborate discussion of asymptotic forms, along with the related procedure, has been done for geometries with internal angle $3\pi/4$, for all three categories of edge clearances. For all the cases, the minimum coefficient of friction needed for the edge to remain in adhesion and

Model	No slip criteria		Closure criteria	
	Edge	**Interior**	**Edge**	**Interior**
A	$g^I_{r\theta} = 0.543$ $f > abs(g^I_{r\theta})$	$g^{II}_{r\theta} = -0.218$ $f > abs(g^{II}_{r\theta})$	$K^I_N < 0$ $Q/P < 0.85$	No interior separation
B	$f > \frac{\left\lvert 1-\frac{K_{II}}{K_I}\right\rvert}{3\frac{K_{II}}{K_I}-1}$	$f = fn(K_{II}/K_I)$	$K_{II}/K_I > 0.33$[1] $K_{II}/K_I < 0.33$[2] $Q/P < 1.16$	No interior separation
C	$g^I_{r\theta} = 0.543$ $f > abs(g^I_{r\theta})$	$f = fn(K_{II}/K_I)$	$K_{II}/K_I > 0.74$[1] $K_{II}/K_I < 0.74$[2] $Q/P < 0.71$	No interior separation
D	$g^I_{r\theta} = 0.213$ $f > abs(g^I_{r\theta})$	$g^{II}_{r\theta} = -1.36$ $f > abs(g^{II}_{r\theta})$	$K^I_N < 0$ $Q/P < 1.87$	No interior separation
E	$f > \frac{\left[1+1.59\frac{K_{II}}{K_I}\right]0.421}{\left[-1+1.244\frac{K_{II}}{K_I}\right]}$	$f = fn(K_{II}/K_I)$	$K_{II}/K_I > 0.8$[1] $K_{II}/K_I < 0.8$[2] $Q/P < 6.19$	No interior separation
F	$g^I_{r\theta} = 0.213$ $f > abs(g^I_{r\theta})$	$f = fn(K_{II}/K_I)$	$K_{II}/K_I > 1.71$[1] $K_{II}/K_I < 1.71$[2] $Q/P < 1.6$	No interior separation
G	$g^I_{r\theta} = 1.34$ $f > abs(g^I_{r\theta})$	$g^{II}_{r\theta} = 0.674$ $f > abs(g^{II}_{r\theta})$	$K^I_N < 0$ $Q/P < 0.138$	$\sigma_{yy} > 0$
H	$f > \frac{\left[1-4.41\frac{K_{II}}{K_I}\right]2.42}{\left[-1+7.24\frac{K_{II}}{K_I}\right]}$	$f = fn(K_{II}/K_I)$	$K_{II}/K_I > 0.138$[1] $K_{II}/K_I < 0.138$[2] $Q/P < -1.09$	$\sigma_{yy} > 0$
I	$g^I_{r\theta} = 1.34$ $f > abs(g^I_{r\theta})$	$f = fn(K_{II}/K_I)$	$K_{II}/K_I > 0.337$[1] $K_{II}/K_I < 0.337$[2] $Q/P > -1.83$	$\sigma_{yy} > 0$

Table 4.1: Summary of contact requirements for various configurations in Figure 4.16

[1] $\forall\ K_I > 0,\ K_{II} > 0$
[2] $\forall\ K_I < 0,\ K_{II} > 0$

the edge in full contact were established. The traction ratio response for various mixed mode conditions has been obtained for the semi-infinite geometry with a finite edge separation.

As an initial observation, we looked at three punch geometries along with the contacting solids (Figure 4.16) and studied the traction ratios along the entire length of the interface for the two extreme cases of separation, i.e., when $d/a \longrightarrow \infty$ and 0. The comparison reveals that the tractions interior to the contact are substantially independent of the presence of the adjacent material, except for the very near-edge region. Further comparison of results with finite slot width geometry ($d/a = 0.05$) was done to check how relevant the trench method is in characterising the behaviour of class of contacts. This reveals that the trench method is extremely accurate in predicting the tractions close to the contact edge. To summarise, we chose three asymptotes namely, (a) the semi-infinite wedge, (b) semi-infinite crack and (c) semi-infinite trench, with all of them providing valuable information relating to the intended region close to the edge (refer Figure 4.22). The first one gives an accurate description of the edge response, when the distance between the block and trench is extremely large, $d/a \gg 1$. The second one can be used when the side clearance is negligible and gives an unique edge solution that depends on the mode mixity prevailing in the region. The third one provides a good description of the near edge region, up to a length equivalent to $\sim 5\%$ of the total width of the contact from the edge and is more accurate for the finite widths $d/a \lesssim 0.1$, so that all practical values of this parameter are covered.

Chapter 5

Frictional shakedown and self-wedging

5.1 Introduction

Frictional contact problems arise in several engineering systems and these are often subjected to substantial static and time varying cyclic loads. Typical examples are the contact interfaces present in the blade root assemblies (dovetail and fir-tree joints) in an aero engine, which are subjected to constant loads due to centrifugal action, and also experience cyclic load due to vibration and turbulence in gas flow (Murthy *et al.* [2004][83]). Apart from this, similar problems are observed in other areas such as bolted joints (Bercynski and Gutowski [2006][84]; Law *et al.*, [2006][85];), spline couplings (Limmer *et al.*, [2001][86]; Banerjee and Hills [2006][87];) and contact bodies with rough surfaces (Walsh [2006][88]) etc. Under the influence of cyclic loading, contact interfaces experience micro-slip or partial slip in restricted smaller zones. The effect of micro-slip eventually leads to the well known damage phenomenon called *fretting fatigue*, which significantly reduces the service life of the components. On the positive side, the slip in the system provides a source of damping, which is beneficial for the overall performance of the system.

Many earlier studies of micro-slip and fretting fatigue have focused on *incomplete* contacts, which are characterised by smooth edges and a bounded pressure distribution. As a consequence of this, a zone of micro-slip will invariably arise at the edge of incomplete contacts subjected to cyclic loads. The existence of closed form solutions and relevance to practical engineering applications motivated more research activity in this area.

Complete contacts on the other hand feature sharp edges with contact area independent of the externally applied load. Because of sharp features, stress concentration effects near the vicinity of the contact edges become inevitable, and therefore complete contacts are commonly avoided during design and manufacturing stages. However these contacts do arise in some engineering applications and so we need methods to study the response of the contact subjected to different loading histories. Also, as will become clear, initially complete contacts can often recede.

5.1.1 Shakedown

Numerical analysis of complete contacts subjected to cyclic loads sometimes predicts that the contact *shakes down*, meaning that the frictional slip that occurs during the first few cycles of loading might set up a state of favourable residual stress that inhibits or reduces slip displacement in the subsequent cycles. This behaviour clearly has some similarities to cyclic plasticity problems, which raises the speculation as to whether *Melan's theorem* (Melan, [1936][89]) for classical plasticity might apply to a frictional contact problem in order to predict shakedown. However the proof of Melan's theorem for plasticity depends on the plastic flow rule being associative, whereas in the case of frictional law the behaviour is non-associative. Klarbring et al., 2007[90] have proved for two and three dimensional discrete systems that Melan's theorem can be applied to frictional elastic systems with Coulomb friction contact conditions if and only if

there is *no coupling* between the tangential (slip) displacements and normal contact reactions. Primarily they identified a class of two-dimensional systems with a degeneracy in the stiffness matrix, for which the shakedown theorem could be established if the friction coefficient is less than a certain critical value. A similar result was established for continuous systems by Barber *et al.*, (2008)[91]. However for *coupled* systems, the attainment of final steady state response depends heavily upon the initial displacement conditions.

5.1.2 Critical coefficient of friction

The critical coefficient of friction f_c plays a pivotal role in determining the generic behaviour of the frictional systems. It was shown in Klarbring *et al.,* [2007][90] that Melan's theorem is applicable if and only if $f < f_c$. Also the system is capable of becoming *'wedged'* if and only if $f > f_c$, meaning that it can sustain a deformed configuration in the absence of external loads. On the other hand, if $f < f_c$, the contact will always return to the undeformed configuration when the external loads are removed. It is to be noted that the critical coefficient of friction, f_c, is geometry dependent and can be computed from the friction angle specific to the component. The friction angle, by definition, provides the maximum inclination such that a simple contact such as a block resting on a slope maintains its position without sliding, in the absence of external forces.

Let us consider a full but very idealised model of the dovetail contact (as shown in Figure 5.1) found in the fan blade root of a jet engine. Our intention is to predict what loading conditions will make the system experience this long term behaviour, i.e., to remain stuck.

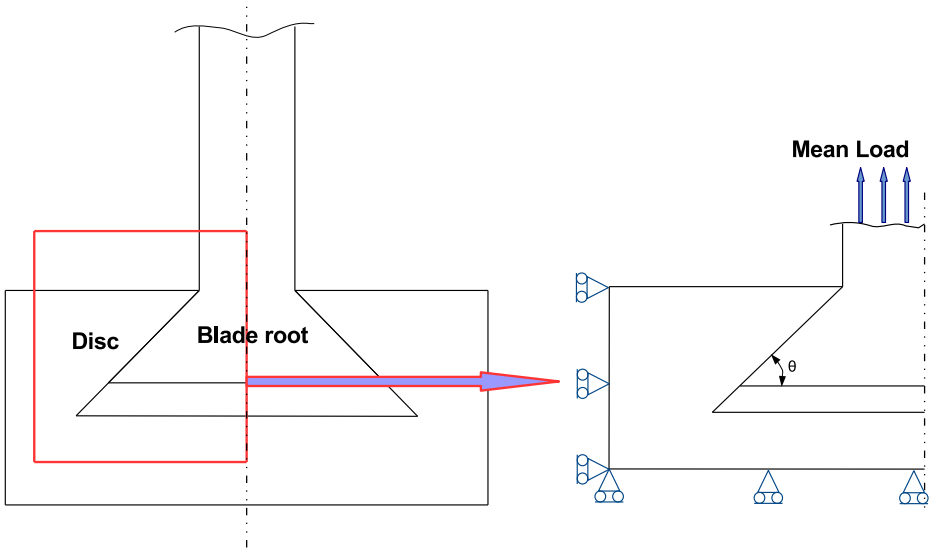


Figure 5.1: Schematic of model used to analyse the wedging response of complete contacts observed in a dovetail geometry subjected to cyclic loads. The inclination θ refers to the internal angle of the blade component, which determines the wedging behaviour of contacts and are referred throughout the Chapter §5

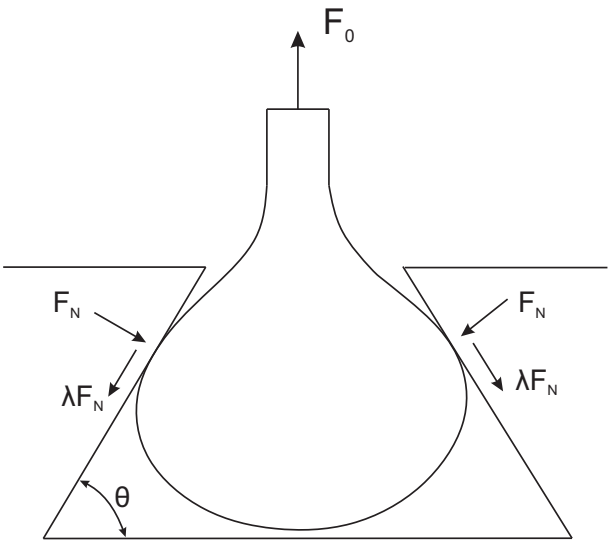


Figure 5.2: Illustration of idealised blade root with force equilibrium considerations to evaluate the wedging condition

5.2 Simple Force Resultant Considerations

The critical coefficient of friction for the component (refer Figure 5.1) to be studied is obtained by considering the force equilibrium, which results in an expression, guiding the behaviour of wedging. The real problem involves a complicated conformal contact with attendant traction distributions which vary along the length of the contact flanks. But certain aspects of this problem can be appreciated by looking at the force resultants alone, rather than the detailed distributions and, furthermore, some aspects of the problem are statically determinate. In Figure 5.2, we show an idealised blade end flared out into the form of a 'bulb', and fitting in a socket with the angle θ defined as shown. The external force applied to the blade is F_0, and the normal reactions on each blade flank are F_N, with shear forces λF_N, as shown. When the blade is being pulled outwards by a monotonically increasing force ($\dot{F}_0 > 0$), equilibrium tells us that

$$\frac{1}{2}F_0 = F_N(cos\theta + \lambda sin\theta), \tag{5.1}$$

and initially this is *not* statically determinate, because the contact will actually be in partial slip, but we expect both F_N and λ to increase positively until the latter reaches the limiting value of the coefficient of friction, f, and then the value of F_N becomes known.

Suppose that the external force is now reduced ($\dot{F}_0 < 0$), so that, although the equilibrium condition remains the same, the sign of the friction force is reversed ($F_N > 0 > \lambda \geq -f$). And the blade will remain held in contact with the socket while ever the last condition remains a strict inequality; when the equality is achieved it means that the blade is released from contact with the flanks of the socket. For example, if we ask what the condition is for retention of the

blade when the applied load is removed completely, this is clearly that

$$cos\theta - fsin\theta > 0 \tag{5.2}$$

or more generally,

$$f > \frac{1}{tan\theta}. \tag{5.3}$$

If we initially load the blade up until it slides, F_0^S,

$$\frac{1}{2}F_0^S = F_N(cos\theta + fsin\theta), \tag{5.4}$$

and the load at which it slides back out of contact, F_o^U is

$$\frac{1}{2}F_0^U = F_N(cos\theta - fsin\theta), \tag{5.5}$$

so that

$$\frac{F_0^U}{F_0^S} = \frac{1 - ftan\theta}{1 + ftan\theta}. \tag{5.6}$$

This factor $\frac{F_0^U}{F_0^S}$ is the ratio of the load at which the contact is released to that needed to form the contact. This ratio is plotted in Figure 5.3b as a function of the internal angle θ and it reveals that the contact release loads required increases as the internal angle gets wider.

Figure 5.3a displays the wedging condition (Equation (5.3)) for components with various internal angles in the interval $[30^o, 80^o]$. For combination of contact angle and coefficients of friction maintained above this curve, the contact is in partial slip and wedging is guaranteed to occur. When the coefficient of friction corresponds to the region below the curve, the contact interfaces slides, either on unloading or complete removal of load. From the plot it is clear that wedging occurs at relatively lower coefficients of friction as the internal angle is increased. It is

further noted that for realistic coefficients of friction, occurrence of wedging is more pronounced for the contacts with internal angles between $[45^o, 80^o]$. For a practical blade to disk contact, such as that shown in Figure 5.1 the blade internal angle is usually maintained at 45^o and the critical coefficient of friction that defines the wedging behaviour is $f_c = 1$. The contacts spend most of their loading cycle in partial slip conditions, when the coefficient of friction is maintained in excess of the limit value f_c and hence have serious implications on the fretting fatigue behaviour of the components. When the coefficient of friction is marginally less than f_c, in addition to partial slip response, we tend to observe rigid body sliding of the contacting components, especially during the load removal stage and thus contributing to the effect of fretting wear. For very less coefficient of friction i.e., when $f \ll f_c$, sliding starts very early during the unloading stage and hence increases the risk of failure (due to fretting wear), with persistent application of further load cycles.

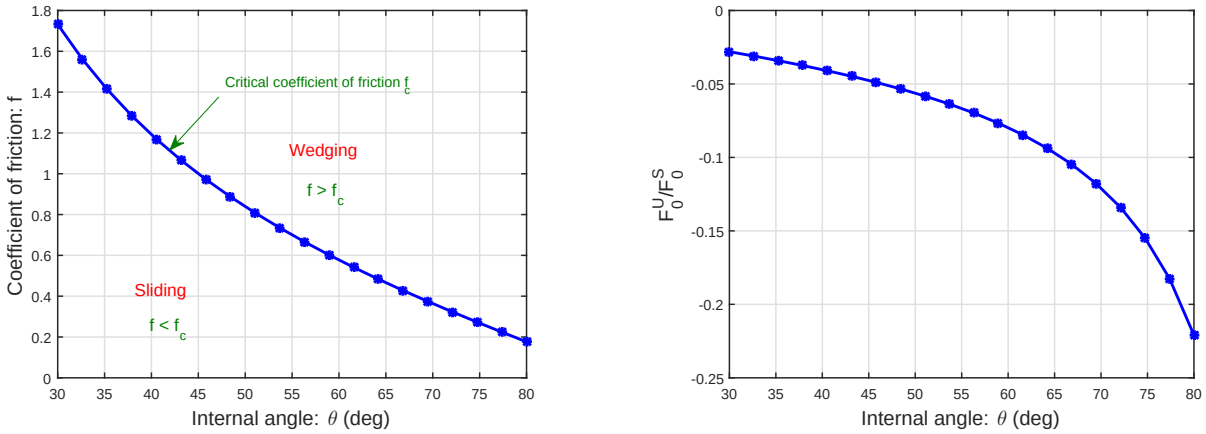


Figure 5.3: (a) Variation of critical coefficient of friction f_c with respect to the internal angle θ, and (b) Response of F_0^U/F_0^S at different internal angles of the contact when $f \gtrapprox f_c$

5.3 Finite element model

To apply these calculations and realise the practical occurrence of wedging phenomena, an equivalent finite element contact model (Figure 5.5) was constructed using the commercial FE program ABAQUS-CAE. The intended component was modelled in an idealised manner with the blade root in frictional contact with disc portion enclosing the socket end. The edges of contact interface were assumed sharp, with contacting bodies elastically similar. Considering symmetry of the problem, one half of the model was considered for simulation. Contact constraints were applied along the interface between blade and disc components. The normal constraints were enforced through direct methods intrinsic to ABAQUS, [92] whereas the tangential behaviour is imposed through the Lagrangean methods. Symmetry boundary conditions were applied along the cut portions of material. To make the simulation realistic, the dimensions and load values for the model were taken from the original dovetail specimen (refer Figure 5.4) which was a part of standard experimental set up used in the fatigue laboratory here in Oxford. The geometry was meshed using a four noded, bilinear, quadrilateral elements. The region close to the neighbourhood of contact interface was assigned a uniform and highly refined mesh, (refer Figure 5.5) so as to achieve precise results. It was noted that the model used a Young's modulus value of $E = 100GPa$ and a Poisson's ratio of 0.3.

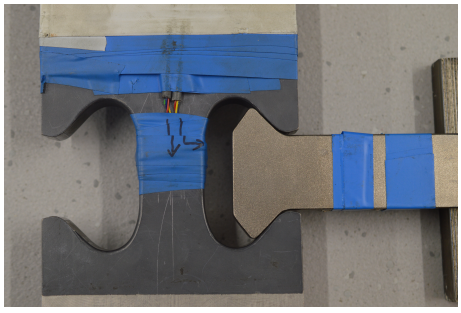


Figure 5.4: Specimen from standard experimental setup used at Fatigue Laboratory in Oxford

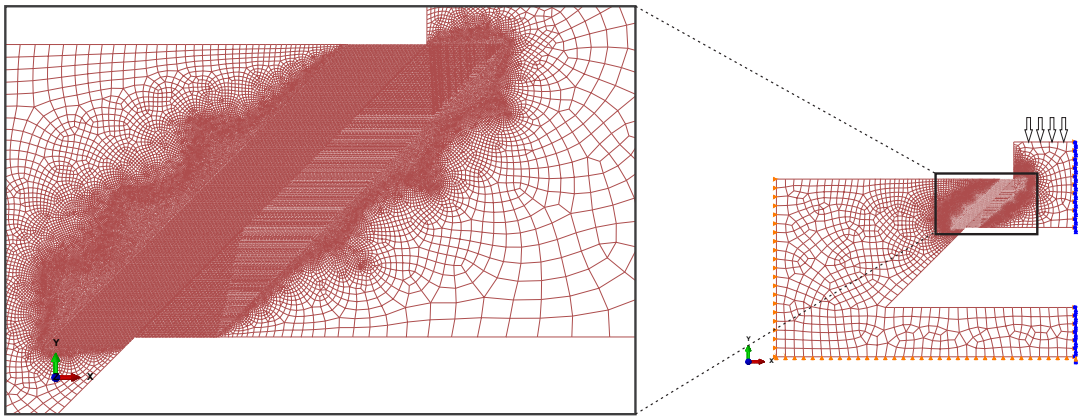


Figure 5.5: Finite element contact model of a blade-root assembly used for wedging analysis. A Zoomed-in mesh region of contact interface is provided for clear vizualisation

A normal tensile load was applied as a uniformly distributed pressure along the top of the shank portion of the blade stub and was increased up to a maximum value of $P_{max} = 144.4MPa$. It was then reduced to 20% of this maximum value in the next stage, and then cycled between the maximum and 20% load limits in subsequent cycles. A schematic of the loading regime is shown in Figure 5.6. The response of contact during unloading stage will be explained in the subsequent sections with explicit reference to the analytical results mentioned in Section 5.2.

5.4 Results

Before analysing the response of contact for individual coefficients of friction, it is worthwhile mentioning the loading stages during which the results are to be interpreted. The initial stage, A in Figure 5.6, where the load is ramped up to the maximum value, is usually neglected for the analysis, as it simply establishes the contact. Separation starts near the leading edge and grows towards the middle region of contact, while "reverse" slip is present throughout the rest of the interface. The next stages, B and C are usually the transient state in nature and constitute the process of building up the favourable residual stress required to achieve shakedown effects; they

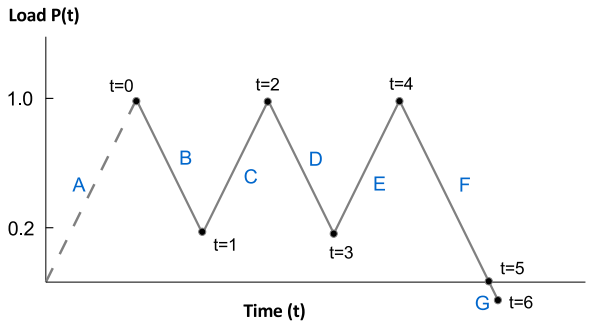


Figure 5.6: Schematic of loading regime considered for analysis

will not be considered in detail. A steady state response might be expected in the subsequent cycles and the focus will mainly be on the un-loading and removal stages where wedging or sliding phenomena are observed.

The contact results, essentially the normal and shear stress components are extracted for any of the contacting interfaces and the resultant of these components P_0 and Q are calculated using a numerical integration procedure. The ratio of these components Q/P_0 can be viewed as a measure of ability of the contacts to achieve the sliding and partial slip conditions. As the ratio Q/P_0 is less than the limiting coefficient of friction, a partial slip behaviour is implied. Once it reaches the limiting friction, a rigid body sliding of the contacting interfaces occur. The various maps (contact regimes) presented in the current chapter are done using the ABAQUS contact output CSTATUS, which provides indicators for the slip/stick/separation conditions.

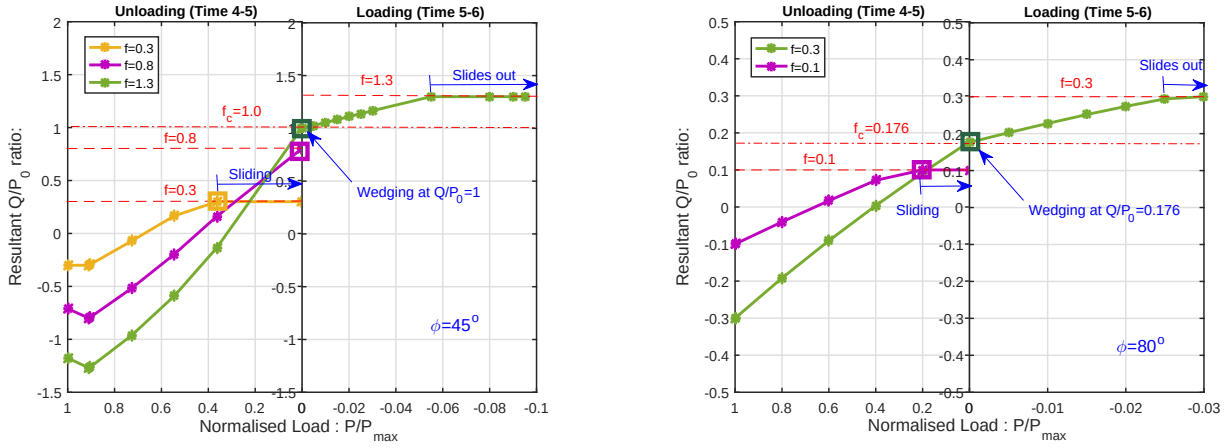
5.4.1 Wedging and sliding as a function of coefficient of friction

In order to demonstrate the validity of the conditions derived for the wedging phenomenon, finite element results were generated for contacts with internal angles 45^o and 80^o, for selected coefficients of friction which are just above and below the value of critical coefficient of friction f_c. These results are illustrated in Figure 5.7a, where the resultant load ratio Q/P_0 has been plotted as a function of the applied normal load P. First we look at the response for the practical dovetail contact with a typical internal angle 45^o, for which the critical coefficient of friction is calculated as 1. When the coefficient of friction is maintained at the rather artificial level of 1.3, the contact clearly remains stuck partially even after removal of the load, as given in Figure 5.7a. This instance can be referred at the end of the stage 'F', with the ratio Q/P_0 approaching the critical coefficient of friction f_c, signifying the effect of wedging. With minimal application of load in the negative direction, the interface slides out of contact, with the ratio Q/P_0 approaches asymptotically the limiting value of friction 1.3.

However the contact does not wedge for the coefficients of friction $f = 0.3, 0.8$ as obviously $f < f_c$, discussed earlier in Section 5.2. When $f = 0.8$, sliding occurs just on the removal of the load, while for the case of $f = 0.3$, it occurs when the applied load is reduced by a factor of ~ 0.35. This behaviour clearly shows that, for the case of increasing coefficients of friction and the loads being removed, the stick zone size increases and the contacts tend to approach partial slip condition and eventually wedge when the coefficient of friction equals f_c. The contact regime showing this response is portrayed in Figure 5.8 for the coefficients of friction $f = 0.3, 0.8$ and 1.3 during an unloading phase 'F' as referred from the loading history in Figure 5.6. For all the cases, separation zones are observed at either ends of the contact, followed by forward slip zones and a central stick zone. As unloading progresses, the contacts tend to close near the edges and the separation zone vanishes eventually on the removal of load.

However the adjacent forward slip zones increase in size, while the stick region in the middle decreases. The key aspect to be observed from the plot is the presence of stick region during the load removal phase, which causes the self-wedging phenomena. For the coefficients of friction $f = 0.3$ and 0.8, the removal of load forces all the contact nodes to slip, thus implying a sliding condition and hence the contacts does not wedge. The contact with the maximum coefficient of friction $f = 1.3$ however wedges, due to the presence of stick zone, which prevents the contact from sliding, even though the loads are completely removed.

Similar behaviour has been obtained for the contact with internal angle 80^o. The critical coefficient of friction for this case is $f_c = 0.176$. As discussed before, for $\theta = 45^o$, the wedging and sliding phenomena occurs for this internal angle for the conditions $f > f_c$ and $f < f_c$ as illustrated in Figure 5.7b.



(a) Internal angle $\theta = 45^o$ **(b)** Internal angle $\theta = 80^o$

Figure 5.7: Plot to illustrate the behaviour of wedging and sliding as a function of coefficient of friction for internal angles 45^o and 80^o: Where f_c is the critical coefficient of friction for wedging and is (a) 1 for $\theta = 45^o$ and (b) 0.176 for $\theta = 80^o$

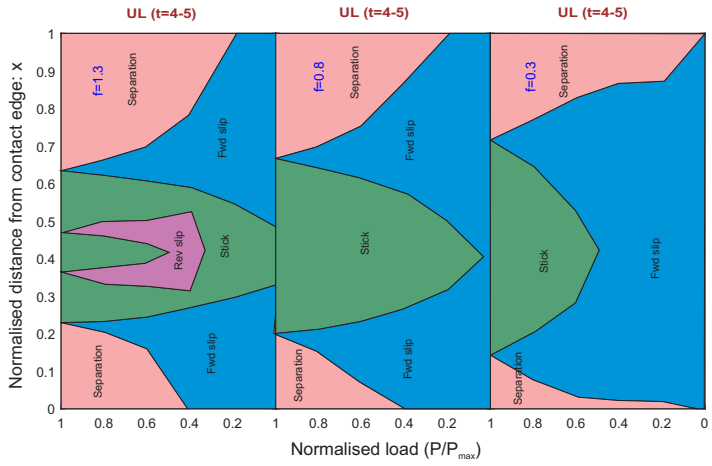


Figure 5.8: Contact regime at unloading stage 'F' to evidence the increasing stick zone for increasing coefficients of friction. Input parameters: Internal angle $\theta = 45^o$, $f = 1.3, 0.8, 0.3$

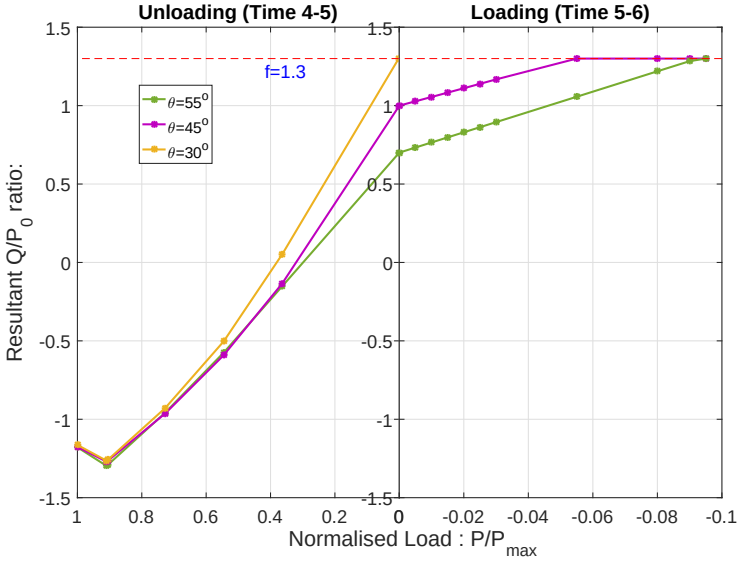


Figure 5.9: Wedging behaviour as a function of internal angle of contact. Input parameter: Coefficient of friction $f = 1.3$

5.4.2 Wedging and sliding as a function of internal angle

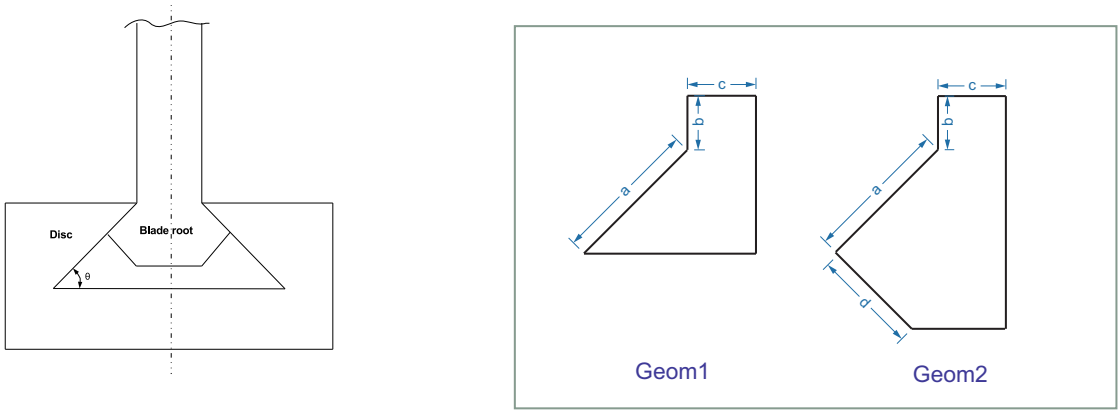
From Figure 5.3a, we know that the tendency for a contact to wedge increases with increasing internal angle of the geometry, for any given physical coefficient of friction. This can now be checked with the finite element results for representative internal angles, say, 55^o, 45^o and

30^o. A coefficient of friction of $f = 1.3$ is chosen for all the cases. The results are again given in the form of resultant load ratio Q/P_0 along the contact as a function of applied loads P in Figure 5.9. It is clear from the plot that the contact with internal angle 30^o does not wedge for the chosen coefficient of friction. This is because the critical coefficient of friction, f_c, for this narrow angle is enormously high, $f_c = 1.85$. It slides out of contact on removal of applied loads. However, wedging occurs for the geometries of internal angles 45^o and 55^o, as the coefficient of friction is more than the critical coefficient of friction f_c. It is noted that, upon removal of load, the contact with 55^o internal angle assumes less Q/P_0 value than the contact with 45^o. This suggests that the wider angle contact contains more adhered region at this instance comparatively. The effect of self wedging is more obvious in the subsequent step, where additional reversing loads are needed to pull the interface out of contact. Here the contact with wider angle ($\theta = 55^o$) requires more effort to slide out of contact, due to the presence of additional stick region. It is further noted that the magnitude of these additional loads $P = -0.055$ and -0.095, for the internal angles $\theta = 45^o$ and 55^o, nearly coincides with the ratio's F_0^U/F_0^S calculated for the respective angles (refer Figure 5.3b).

5.4.3 Contact behaviour as a function of blade geometry

Further analysis of contact behaviour has been performed for an alternative profile of the blade root used in the assembly. This is shown in Figure 5.10a, with an intention to study the following aspects of the contact (a) the traction distribution (b) wedging (c) contact regime (partial slip evolution). Figure 5.10b compares the relative dimensions of the considered geometries on an uniform scale. As can be referred from the figure, the sizes a, b and c are maintained constant, with the extension to the geometry realised through the additional dimension d.

Figure 5.11, presents a comparison of the resultant load ratio Q/P_0, obtained by FE for



(a) (b)

Figure 5.10: (a) Schematic of blade-root assembly fitted with alternate geometry and (b) Comparison of original and alternate geometries on an uniform scale

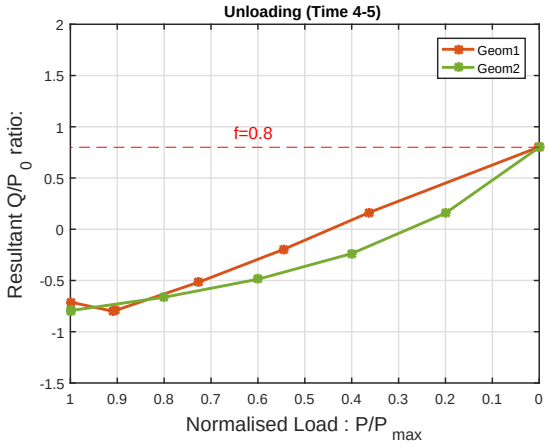
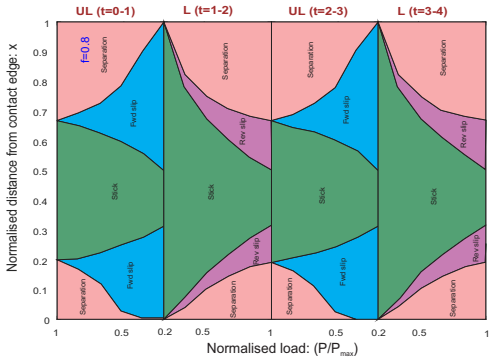
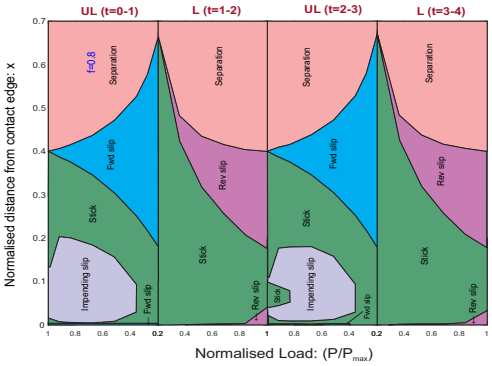


Figure 5.11: Illustration of wedging behaviour for the geometries considered during the unloading stage (4-5). Input parameters: Coefficient of friction $f = 0.8$, Internal angle $\theta = 45^o$

the profiles considered. An internal angle of 45^o and coefficient of friction 0.8 are chosen for this computation. From the plot it is clear that there are some differences initially, during the unloading process; but the results are consistent on removal of load. As the coefficient of friction is less than f_c neither geometry wedges and indicates that the addition of material at the dovetail root (Figure 5.10a) does not cause a contradiction with the condition set out in Equation 5.3.

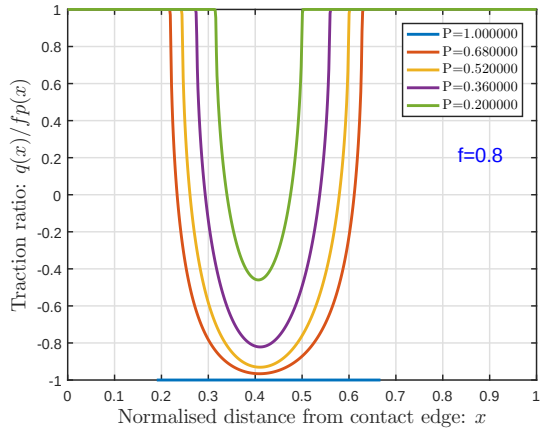


(a) Contact regime for the original geometry (Geom1) in Figure 5.10b

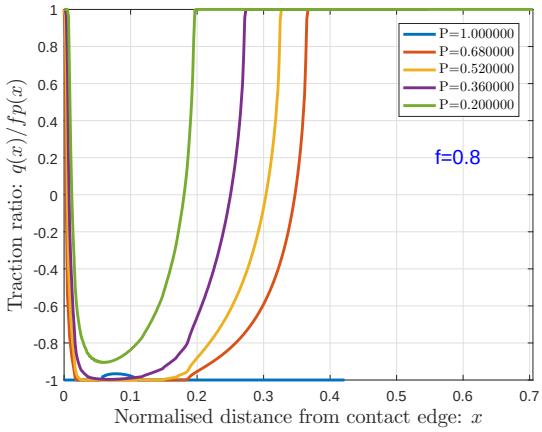


(b) Contact regime for the alternate geometry (Geom2) in Figure 5.10b

Figure 5.12: Comparison of contact regimes for the blade profiles considered. Input parameters: Internal angle $\theta = 45^o$, $f = 0.8$



(a) Traction ratio for the original geometry (Geom1) in Figure 5.10b



(b) Traction ratio for the alternate geometry (Geom2) in Figure 5.10b

Figure 5.13: Comparison of traction ratio behaviour at unloading phase (2-3) for the blade profiles considered, to validate the slip/separation zones present in Figures 5.12a and 5.12b. Input parameters: Internal angle=45^o, $f = 0.8$

Appreciable differences were observed in the evolution of contact regimes for the transient and steady states as seen in Figure 5.12 for the relevant unloading and loading stages $(B - E)$, defined in the loading cycle. First consider the contact regime for the original geometry in Figure 5.12a. When the load starts to decrease from its maximum value, the immediate effect

is for a reduction in separation zones near the leading and trailing edges, followed by advancing forward slip zones, separated by a stick region. The exact reverse behaviour happens during re-loading phase, when the load is increased from 20% to the maximum value. During this phase the separation zone increases and the nodes which experienced forward slip previously, undergoes reverse slip. The stick zone remains un-affected for most of the interface. The alternative geometry produces a similar behaviour, but with the slip zone size near the trailing edge extremely negligible compared to the leading edge zone, but it never separates near the trailing edge. The traction ratio $q(x)/(fp(x))$ corresponding to this behaviour is given in Figure 5.13 for an unloading phase $(2-3)$ in the steady state. From the plot, it is clear that slip zones are identified along the interface, where the traction ratio $q/fp = 1$, suggesting the attainment of limiting friction for these nodes. This particular value is obtained at both ends for the original geometry and at the leading edge for the alternate geometry, conforming to the observations from the contact regime in Figure 5.12. Furthermore, as unloading happens, contact pressure decreases and hence the traction ratio q/fp increases for both cases. The zone corresponding to impending slip can be treated as the case where the nodes present in this region are in the verge of a possible slip. The fact that the traction ratio plot shows a stick like behaviour confirms this particular state of contact. It is further noted that the contact width for the original geometry is 30% more compared to the alternative geometry. The different behaviour of the two contacts can be attributed to the relative stiffnesses of the blade roots. The additional material in the blade root makes the geometry stiffer and drives separation near the leading edge, and leads to negligible slip near the trailing edge.

5.5 Conclusion

The implication of the critical coefficient of friction, f_c, which plays a key role in wedging behaviour of complete contacts, has been investigated thoroughly. An idealised version of the dovetail contact assembly has been considered. Simple application of force equilibrium provides an expression for retention of the blade, in terms of the internal angle θ, when the load is completely removed. Finite element simulations of the dovetail contact assembly were carried out to study the behaviour of wedging with respect to the following parameters: (a) Coefficient of friction (b) Internal contact angle of the blade component (c) Shape of the blade geometry. From the results, it seems clear that wedging occurs in partial slip conditions, when the coefficient of friction f is greater than the critical coefficient of friction f_c. However the contact interfaces slides when $f < f_c$. This behaviour has been verified for two cases of internal angles $\theta = 45^o$ and 80^o.

The wedging phenomenon has also been studied as a function of the internal angle of the dovetail blade geometry. It further reveals that the tendency to wedge increases with the increasing angle of inclination θ, provided that $f < f_c$. Additional loads were applied to enable the wedged configurations come out of contact and the estimates were compared with the analytical predictions.

Finally an alternate blade geometry with additional material is considered for analysis. The general character of wedging behaviour remains unchanged with the addition of material. However, appreciable differences were noticed with regards to the contact stick/slip/separation regime, due to the relative stiffness of the blade geometry and the different "shape"of contact edge angle.

Chapter 6

Static Reduction method

6.1 Motivation

Methods for simulating frictional response of contact are in high demand in several engineering disciplines where accurate modelling of interactions between solids are required. Components are often subjected to substantial mean load and cyclic loads. Consider, for example, the contact interface between a turbine blade and the disk in a gas turbine engine being subjected to large constant load due to centrifugal action, but which also experiences time-varying cyclic load due to vibration and turbulence in gas flow (Murthy *et al.*, [2004])[93]. Under the cyclic loading conditions, the contact interface, which is supposedly the structure's weakest link, experiences periodic reversed relative motion and thereby inflicts wear which eventually reduces the service life of the component. However, the frictional slip that occurs during the first few cycles might set up a state of residual stress that inhibits or reduces slip in subsequent cycles. Therefore, it is very much essential to predict the loading conditions that will cause the system to experience such a range of different behaviour.

Often, conventional finite element solutions to such problems are constructed by linking

finite element models of the contacting bodies through contact elements and utilizing either the penalty or augmented Lagrangian method to handle the discontinuous nature of the contact boundary conditions. Quiet often the resulting models are very large which ultimately leads to increased computational effort and loss of accuracy.

Reduction methods are used to reduce the number of degrees of freedom in a finite element model. The static reduction method, sometimes referred to as Guyan reduction or static condensation, is the most popular reduction method in practice and is the basis for several FE sub-structuring techniques. This method, when applied to the finite element description of an elastic contact problem (where body forces are not present), reduces the dimensionality of the problem to the set of contact nodes alone. This technique is attractive as it enables increased computation speed and reduced memory requirements, especially for evolutionary contact problems, and also gives the user great control over the detailed implementation of contact and friction laws. The reduced stiffness matrix computed through this procedure is also viewed as an excellent vehicle to determine the critical coefficient of friction for the problem to be well posed and it facilitates determination of conditions under which a frictional system may shake down (Flicek et al., [2014][94]) when subjected to periodic loading.

Considering the above advantages, the static reduction method was implemented as a plugin for the Rolls-Royce proprietary finite element code SC03 to solve quasi-static frictional elastic contact problems. At the present level of implementation, this procedure may be applied to two dimensional, linear elastic, quasi-static frictional contact problems involving complete contacts where the contact interface lies approximately along a straight line.

Hence, a reduced finite element model obtained through special reduction techniques like sub-structurisation, static reduction etc., are attractive and enable the solution to be computed for desired degrees of freedom quickly and without loss of accuracy. This approach is particularly well suited to static problems where inertial forces are neglected.

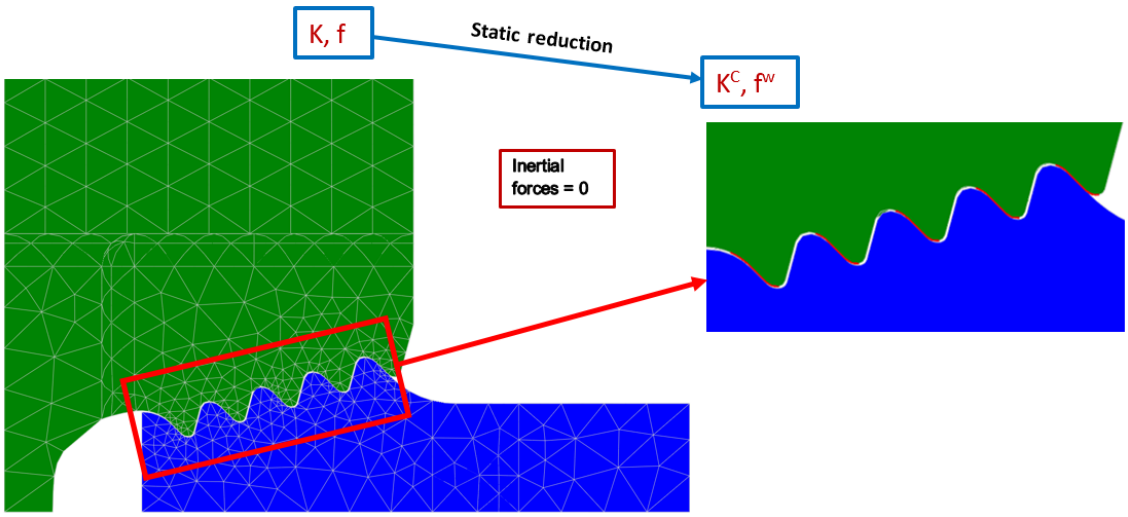


Figure 6.1: Illustration of static reduction method

6.2 Introduction

Static reduction or the static condensation method (Mario Paz et al., [2001][95]) is one of the most popular and sought-after reduction methods in practice for solving static problems. It is defined as the process of reducing the number of free displacements or degrees of freedom by mathematical operations on the assembled structural equilibrium equations. A symbolic representation of static reduction is shown in Figure 6.1. In this process the inertia terms associated with the discarded degrees of freedoms are neglected. A practical method of accomplishing the reduction of the number of degrees of freedom, and hence the reduction of the stiffness matrix, is to identify those degrees of freedom to be condensed as secondary degrees of freedom, and to express them in terms of the remaining primary degrees of freedom. The relationship between secondary and primary degrees of freedom is found by establishing the static relation between them, and hence the name "static reduction method". This relationship provides the means to reduce the number of unknowns in the system stiffness matrix equation.

6.3 Literature review

Modern structural analysis typically requires operations with very large stiffness matrices obtained by the finite element method. Procedures for structural optimization and structural identification require costly repeated analysis and sensitivity calculations. Finite element based contact problems are often associated with a refined mesh adjacent to the contact regions and the degrees of freedom to be solved are enormous especially for large models. Most of the computation time is often spent on matrix operations during the solution stage and hence efficient numerical techniques are always the need of the hour to compute the results quickly, without any compromise of accuracy.

As most of the numerical contact models that have been solved are loaded quasi statically, established methods like sub-structurization or static reduction can be employed effectively to eliminate the internal degrees of freedom. This enables computation of the reduced stiffness matrix and load vector from the global FE model, which then subsequently can be used to run transient simulations of the contact evolution at least 10 times faster than with a full finite element model.

The concept of static condensation method started earlier, in 1965, when Robert J. Guyan [1965][96] performed natural mode analysis by simultaneous reduction of the mass matrix. Later Edward L. Wilson and K.J. Bathe [1973][97] applied this method within the finite element framework and obtained a reduced form of stiffness matrix and stress-displacement transformation matrix. The technique was presented as an extension of the Gaussian elimination algorithm. Qu. Z *et al.,* [2003][98] presented three extensive condensation methods for model reduction of non-classical damped systems. The main advantage of these methods is that the explicit forms of the reduced stiffness, mass and damping matrices can be obtained directly from the reduced model.

Many commercial finite element packages allow users to apply reduction methods to eliminate degrees of freedom during the course of structural analysis. However, it is not currently possible to apply these methods to contact domains and perform advanced calculations using the reduced contact stiffness matrix, in order to determine the load factors critical for the contact to shake down. The main objective of implementing the static reduction method as a plugin to SC03 is to perform shakedown calculations using the reduced stiffness matrix, and facilitate performance studies of contacts under fatigue conditions. This requires application of cyclic loads, where numerous load cycles have to be simulated before the contact solution reaches a steady state response. The static reduction method is particularly appealing and effective in treating such problems with multiple load cases and with millions of degrees of freedom, while making the computation less intensive.

Another big advantage of this approach concerns the accuracy of the contact solution achieved using the iterative procedure suggested by Ahn and Barber [2008][99]. Contact compatibility algorithms viz., penalty or augmented Lagrange methods are often associated with approximations so as to strike a balance between achieving optimal contact stiffness and the avoidance of an ill-conditioned matrix. On the other hand, the proposed Gauss-Seidel [2008][99] based iterative solution algorithm works on a completely different approach and resolves the contact in-equalities for each node in an accurate sense and thereby avoids the approximations induced by standard algorithms.

6.4 Mathematical description of Static Reduction method

6.4.1 Elimination of degrees of freedoms using a Static Reduction process

This section aims to describe the static reduction procedure in a mathematical sense. The structural equilibrium equation for a static problem can be written as follows.

$$[K]\{U\} = \{P\}. \tag{6.1}$$

The method could be best described by assuming that those secondary degrees of freedom to be reduced or condensed are arranged in the first s nodal coordinates and the remaining primary degrees of freedom are the last p nodal coordinates. With such an arrangement equation (6.1) could be partitioned to the following form,

$$\begin{bmatrix} K_{ss} & K_{sp} \\ K_{ps} & K_{pp} \end{bmatrix} \begin{Bmatrix} u_s \\ u_p \end{Bmatrix} = \begin{Bmatrix} F_s \\ F_p \end{Bmatrix}, \tag{6.2}$$

where,

$\{u_s\}$ = Displacement vector corresponding to secondary degrees of freedom to be reduced

$\{u_p\}$ = Displacement vector corresponding to primary degrees of freedom to be retained.

A simple multiplication of the partitioned system in equation (6.2) yields the following two matrix equations

$$[K_{ss}]\{u_s\} + [K_{sp}]\{u_p\} = \{F_s\} \tag{6.3}$$

$$[K_{ps}]\{u_s\} + [K_{pp}]\{u_p\} = \{F_p\}. \tag{6.4}$$

Solving equation (6.3) for the vector u_s results in

$$\{u_s\} = [K_{ss}]^{-1}[\{F_s\} - [K_{sp}]\{u_p\}],$$

which could simply be written as follows

$$u_s = K_{ss}^{-1}[F_s - K_{sp}u_p]. \tag{6.5}$$

Recall equation (6.4) in simple form (omitting the bracket denoting matrices & vectors)

$$K_{ps}u_s + K_{pp}u_p = F_p, \tag{6.6}$$

Substituting u_s from equation (6.5) to equation (6.6) above gives

$$K_{ps}[K_{ss}^{-1}(F_s - K_{sp}u_p)] + K_{pp}u_p = F_p, \tag{6.7}$$

$$-K_{ps}K_{ss}^{-1}K_{sp}u_p + K_{pp}u_p = F_p - K_{ps}K_{ss}^{-1}F_s,$$

$$[-K_{ps}K_{ss}^{-1}K_{sp} + K_{pp}]u_p = F_p - K_{ps}K_{ss}^{-1}F_s. \tag{6.8}$$

Equation (6.8) can be conveniently represented as follows

$$\boxed{[\hat{K_{pp}}]\{u_p\} = \{\hat{F_p}\}} \tag{6.9}$$

Where,

$$[\hat{K_{pp}}] = -K_{ps}K_{ss}^{-1}K_{sp} + K_{pp}, \tag{6.10}$$

$$\{\hat{F_p}\} = F_p - K_{ps}K_{ss}^{-1}F_s. \tag{6.11}$$

Thus equation (6.9) is the condensed stiffness equation relating through the condensed stiffness matrix $[\hat{K_{pp}}]$, condensed force vector $\{\hat{F}_p\}$ and the primary nodal displacements $\{u_p\}$.

6.4.2 Recovery of the eliminated degrees of freedoms using back-substitution

Once the primary displacement degrees of freedoms are calculated using the procedure mentioned in Section 6.4.1, the question remains how the displacements for eliminated degrees of freedom can be calculated. This could be easily accomplished by a simple back-substitution of the computed primary displacements $\{u_p\}$ in equation (6.5).

Recalling the condensed set of equations from equation (6.9) and solving for $\{u_p\}$ yields

$$[\hat{K_{pp}}]\{u_p\} = \{\hat{F_p}\}, \tag{6.12}$$

$$\{u_p\} = [\hat{K_{pp}}]^{-1}\{\hat{F_p}\}. \tag{6.13}$$

The eliminated degrees of freedom $\{u_s\}$ can be determined by substituting $\{u_p\}$ from equation (6.13) to equation (6.5)

$$\{u_s\} = [K_{ss}]^{-1}\{\{F_s\} - [K_{sp}][\hat{K_{pp}}]^{-1}\{\hat{F_p}\}\}, \tag{6.14}$$

which could be written in simple form as follows:

$$\boxed{u_s = K_{ss}^{-1}\{F_s - K_{sp}\hat{K_{pp}}^{-1}\hat{F_p}\}} \tag{6.15}$$

6.5 Application of Static Reduction method to general contact problems

The proposed static reduction method is applied to two dimensional quasi-static problems, whereby the equilibrium equations are applied to the degrees of freedoms at the non-contact nodes, to reduce the problem to one defined on the set of contact nodes alone. Treatment of quasi-static problems allows elimination of inertial forces along the discarded degrees of freedom. In effect the problem then becomes formally equivalent to a system of N massless rigid blocks connected by a $N \times N$ stiffness matrix, with each block potentially in frictional contact with a rigid plane obstacle (Thaitirarot [2013][100]), as shown in Figure 6.2. This approach facilitates solving the evolutionary contact problem in a finite element perspective, without the necessity of contact elements. An iterative approach called the Gauss Seidel algorithm is formulated which resolves the contact inequalities and computes the solution for the reduced contact model using the extracted contact stiffness matrix and load vector. This generic idea of static reduction is applied to contact models which exhibit the following constitutive behaviour.

(i) Single elastic body in frictional contact with rigid body

(ii) Frictional contact between two elastic bodies

The subsequent sections discuss the procedure for extracting the reduced contact stiffness matrix from the full finite element stiffness matrix and the method adopted to solve the problem using the reduced matrices.

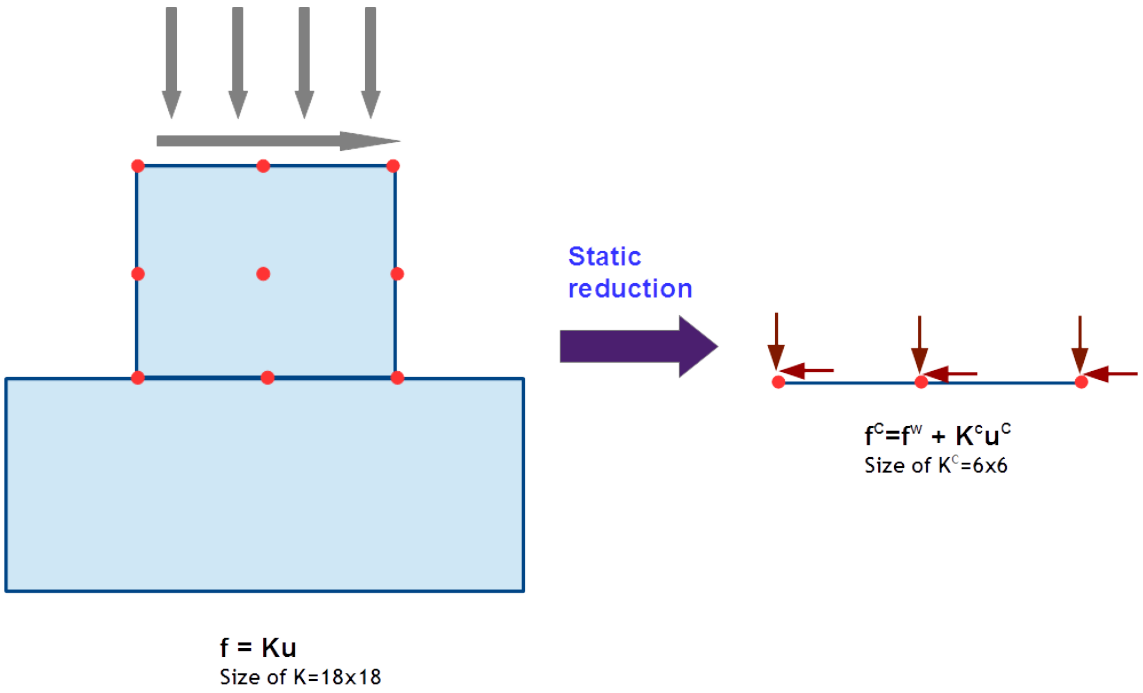


Figure 6.2: Symbolic representation of reduction of degree of freedoms

6.5.1 Single elastic body in contact with a rigid body

It is convenient, to demonstrate the application of static reduction method, to think of the simplest case where a single elastic body makes a frictional contact with a rigid obstacle at a shared set of contact nodes. Section 6.5.2 discuss the practical problem where two elastic bodies make contact with each other, which could then be solved by idealising the problem to a series of single body problems.

The initial step involves categorizing the nodes in the finite element model in to three different sets namely the contact nodes S_C, externally loaded nodes S_E, and the internal nodes S_I. For the most general case, the set S_E should be further partitioned into S_U, where non-zero nodal displacements are prescribed, and S_T, where non-zero nodal forces are prescribed, but in most practical problems one of these sets will be null. In other words, the problem could

be formulated as *either* force controlled or displacement controlled, based on the underlying boundary conditions.

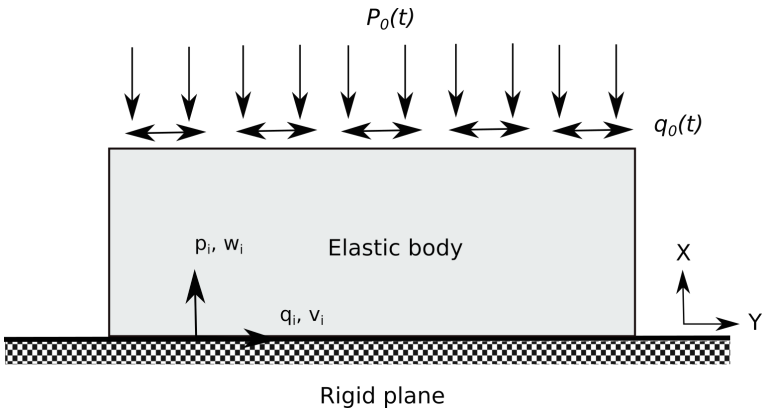


Figure 6.3: Representation of coordinate system adopted in static reduction of elastic body in contact with a rigid surface

Sign convention

At the current level of implementation only two dimensional problems are treated and hence there are two degrees of freedom applicable for each node. The sign convention adopted within the static reduction method for typical contact models is given in Figure 6.3. The nodal force f_j^C and displacement u_j^C for a contact node can be written as

$$\boldsymbol{f_j^C} = \left\{ \begin{array}{c} q_j \\ p_j \end{array} \right\} \tag{6.16a}$$

$$\boldsymbol{u_j^C} = \left\{ \begin{array}{c} v_j \\ w_j \end{array} \right\}, \tag{6.16b}$$

where, if a right hand coordinate system is defined at each contact node with positive y direction directed along the interior of the body, then the forces p_j and q_j are positive in the positive x, y directions, respectively. A similar convention holds good for the displacements v_j and w_j. Here,

the positive normal force p_j corresponds to compressive contact and a positive w_j contributes to a positive gap along the contact interface. Having defined the force vector and displacement for a single node, the complete set of nodal forces and displacement for the contact interface could be written as

$$\boldsymbol{f^C} = \left\{ \boldsymbol{f_1^C}, \boldsymbol{f_2^C}, \boldsymbol{f_3^C}, ..., \boldsymbol{f_N^C} \right\}^T \tag{6.17a}$$

$$\boldsymbol{u^C} = \left\{ \boldsymbol{u_1^C}, \boldsymbol{u_2^C}, \boldsymbol{u_3^C}, ..., \boldsymbol{u_N^C} \right\}^T, \tag{6.17b}$$

where N is the number of contact nodes. The equilibrium equation for a linear elastic system may be written as (Thaitirarot [2013][100]),

$$\boldsymbol{f^c} = \boldsymbol{f^w} + \boldsymbol{K^C u^C}, \tag{6.18}$$

where $\boldsymbol{K^C}$ is the reduced contact stiffness matrix, which is positive definite and symmetric by nature and $\boldsymbol{f^w}$ represents the contact nodal forces that would be developed by the externally applied load, if the contact nodal displacements were all constrained to be zero (i.e if $\boldsymbol{u^c} = 0$).

Elimination of internal degrees of freedom

The equilibrium equation for the case of a generic static problem can be written as

$$\boldsymbol{f} = \boldsymbol{K u}, \tag{6.19}$$

In a majority of practical problems the internal nodes outnumber the external or contact nodes present in the model. Assuming the body forces are not present, the dimensionality of the problem would be reduced significantly by applying the condition $\boldsymbol{f^I} = 0$, thereby eliminating

the respective degrees of freedom. The reduction process starts with partitioning the stiffness matrix in to components specific to external, internal and contact degrees of freedom as given in the below equation.

$$\begin{Bmatrix} \boldsymbol{f^I} \\ \boldsymbol{f^E} \\ \boldsymbol{f^C} \end{Bmatrix} = \begin{bmatrix} \boldsymbol{K^{II}} & \boldsymbol{K^{IE}} & \boldsymbol{K^{IC}} \\ \boldsymbol{K^{EI}} & \boldsymbol{K^{EE}} & \boldsymbol{K^{EC}} \\ \boldsymbol{K^{CI}} & \boldsymbol{K^{CE}} & \boldsymbol{K^{CC}} \end{bmatrix} \begin{Bmatrix} \boldsymbol{u^I} \\ \boldsymbol{u^E} \\ \boldsymbol{u^C} \end{Bmatrix}, \tag{6.20}$$

where the superscripts I,E and C corresponds to the internal, externally loaded and contact nodes respectively. The nodal forces for the internal, external, and contact nodes are represented by the vectors $\boldsymbol{f^I}$, $\boldsymbol{f^E}$, $\boldsymbol{f^C}$ respectively. A similar convention is adopted for the nodal displacements $\boldsymbol{u^I}$, $\boldsymbol{u^E}$ and $\boldsymbol{u^C}$. The terms in the partitioned stiffness matrix represents the stiffness values between any two degrees of freedom from the respective node sets. For example, the sub-matrix $\boldsymbol{K^{II}}$ corresponds to the stiffness values between the set of internal nodes, while $\boldsymbol{K^{CI}}$ represents the stiffness values between contact and internal nodes. Equation 6.20 can be further written as

$$\boldsymbol{f^I} = \boldsymbol{K^{II}u^I} + \boldsymbol{K^{IE}u^E} + \boldsymbol{K^{IC}u^C}, \tag{6.21}$$

and the remaining set of equations

$$\begin{Bmatrix} \boldsymbol{f^E} \\ \boldsymbol{f^C} \end{Bmatrix} = \begin{bmatrix} \boldsymbol{K^{EI}} & \boldsymbol{K^{EE}} & \boldsymbol{K^{EC}} \\ \boldsymbol{K^{CI}} & \boldsymbol{K^{CE}} & \boldsymbol{K^{CC}} \end{bmatrix} \begin{Bmatrix} \boldsymbol{u^I} \\ \boldsymbol{u^E} \\ \boldsymbol{u^C} \end{Bmatrix}. \tag{6.22}$$

Applying the condition $\boldsymbol{f^I} = 0$ in equation (6.21) and solving for $\boldsymbol{u^I}$ gives

$$\boldsymbol{K^{II}u^I} = -\boldsymbol{K^{IE}u^E} - \boldsymbol{K^{IC}u^C}$$

$$\boldsymbol{K^{II}u^I} = -\begin{bmatrix}\boldsymbol{K^{IE}} & \boldsymbol{K^{IC}}\end{bmatrix}\begin{Bmatrix}\boldsymbol{u^E}\\ \boldsymbol{u^C}\end{Bmatrix}$$

$$\boldsymbol{u^I} = -\left[\boldsymbol{K^{II}}\right]^{-1}\begin{bmatrix}\boldsymbol{K^{IE}} & \boldsymbol{K^{IC}}\end{bmatrix}\begin{Bmatrix}\boldsymbol{u^E}\\ \boldsymbol{u^C}\end{Bmatrix}. \tag{6.23}$$

Using this result to eliminate $\boldsymbol{u^I}$ in equation (6.22) yields

$$\begin{Bmatrix}\boldsymbol{f^E}\\ \boldsymbol{f^C}\end{Bmatrix} = \begin{bmatrix}\boldsymbol{K^{EE}} & \boldsymbol{K^{EC}}\\ \boldsymbol{K^{CE}} & \boldsymbol{K^{CC}}\end{bmatrix}\begin{Bmatrix}\boldsymbol{u^E}\\ \boldsymbol{u^C}\end{Bmatrix} + \begin{bmatrix}\boldsymbol{K^{EI}}\\ \boldsymbol{K^{CI}}\end{bmatrix}\boldsymbol{u^I}$$

$$\begin{Bmatrix}\boldsymbol{f^E}\\ \boldsymbol{f^C}\end{Bmatrix} = \left[\begin{bmatrix}\boldsymbol{K^{EE}} & \boldsymbol{K^{EC}}\\ \boldsymbol{K^{CE}} & \boldsymbol{K^{CC}}\end{bmatrix} - \begin{bmatrix}\boldsymbol{K^{EI}}\\ \boldsymbol{K^{CI}}\end{bmatrix}\left[\boldsymbol{K^{II}}\right]^{-1}\begin{bmatrix}\boldsymbol{K^{IE}} & \boldsymbol{K^{IC}}\end{bmatrix}\right]\begin{Bmatrix}\boldsymbol{u^E}\\ \boldsymbol{u^C}\end{Bmatrix}. \tag{6.24}$$

At this point, it is convenient to use these relations to define a reduced matrix

$$\boldsymbol{L} = \left[\begin{bmatrix}\boldsymbol{K^{EE}} & \boldsymbol{K^{EC}}\\ \boldsymbol{K^{CE}} & \boldsymbol{K^{CC}}\end{bmatrix} - \begin{bmatrix}\boldsymbol{K^{EI}}\\ \boldsymbol{K^{CI}}\end{bmatrix}\left[\boldsymbol{K^{II}}\right]^{-1}\begin{bmatrix}\boldsymbol{K^{IE}} & \boldsymbol{K^{IC}}\end{bmatrix}\right], \tag{6.25}$$

and to partition it such that

$$\left\{ \begin{array}{c} \boldsymbol{f^E} \\ \boldsymbol{f^C} \end{array} \right\} = \begin{bmatrix} \boldsymbol{L^{EE}} & \boldsymbol{L^{EC}} \\ \boldsymbol{L^{CE}} & \boldsymbol{L^{CC}} \end{bmatrix} \left\{ \begin{array}{c} \boldsymbol{u^E} \\ \boldsymbol{u^C} \end{array} \right\}. \tag{6.26}$$

Determination of reduced stiffness matrix and load vectors

Computation of the reduced contact stiffness matrix and load vector is very much dependent on whether the external loads are applied through force or displacement control. Hence it is very much important to specify the relevent mode of load application before the stiffness matrix and load vector is computed. This is because the contact stiffness matrix is a solution of the problem in which the prescribed loading conditions are replaced by equivalent homogeneous conditions, which is traction free in the force controlled case and corresponds to zero displacement(fixed) in the displacement controlled case.

Force controlled problem

For the case of a force controlled problem, the nodal forces at the externally loaded nodes are known functions of time t. Equation (6.26) can be written as

$$\boldsymbol{f^E} = \boldsymbol{L^{EE}}\boldsymbol{u^E} + \boldsymbol{L^{EC}}\boldsymbol{u^C}, \tag{6.27a}$$

$$\boldsymbol{f^C} = \boldsymbol{L^{CE}}\boldsymbol{u^E} + \boldsymbol{L^{CC}}\boldsymbol{u^C}. \tag{6.27b}$$

The external nodal force vector $\boldsymbol{f^E}$ is a known quantity and, from equation (6.27a), the displacement vector at the externally loaded nodes $\boldsymbol{u^E}$ can be computed as

$$\boldsymbol{u}^E = \left[\boldsymbol{L^{EE}}\right]^{-1} \left[\boldsymbol{f}^E - \boldsymbol{L}^{EC}\boldsymbol{u}^C\right]. \tag{6.28}$$

Then, substitution of $\boldsymbol{u^E}$ in equation (6.27b) yields

$$\boldsymbol{f}^C = \boldsymbol{L^{CE}}\left[[\boldsymbol{L^{EE}}]^{-1}[\boldsymbol{f}^E - \boldsymbol{L}^{EC}\boldsymbol{u}^C]\right] + \boldsymbol{L}^{CC}\boldsymbol{u}^C \tag{6.29a}$$

$$\boldsymbol{f}^C = L^{CE}[\boldsymbol{L^{EE}}]^{-1}\boldsymbol{f}^E + \left[\boldsymbol{L}^{CC} - \boldsymbol{L}^{CE}[\boldsymbol{L}^{EE}]^{-1}\boldsymbol{L}^{EC}\right]\boldsymbol{u}^C. \tag{6.29b}$$

The equilibrium equation (6.18) for a linear elastic system can be recalled as

$$\boldsymbol{f^c} = \boldsymbol{f^w} + \boldsymbol{K^C}\boldsymbol{u^C},$$

So it is apparent that the reduced equation (6.29b) is structurally similar to the form of the above equilibrium equation (6.18). The respective terms for the condensed contact stiffness matrix $\boldsymbol{K}^C$ and nodal force vector $\boldsymbol{f}^w$ can then be written as

$$\boldsymbol{K}^C = \left[\boldsymbol{L}^{CC} - \boldsymbol{L}^{CE}[\boldsymbol{L}^{EE}]^{-1}\boldsymbol{L}^{EC}\right] \tag{6.30a}$$

$$\boldsymbol{f}^w = \boldsymbol{K}^E\boldsymbol{f}^E, \tag{6.30b}$$

where

$$\boldsymbol{K}^E = \boldsymbol{L}^{CE}[\boldsymbol{L}^{EE}]^{-1}.$$

Displacement controlled problem

For the case where external load is applied in the form of displacement control, the nodal displacements at the externally loaded nodes $\boldsymbol{u^E}$ are prescribed functions of time. Recalling equation (6.27b)

$$\boldsymbol{f^C} = \boldsymbol{L^{CE}u^E} + \boldsymbol{L^{CC}u^C},$$

since the external nodal displacements u^E are known, we can immediately write the equations in the form of an equilibrium equation (6.18) as

$$\boldsymbol{K}^C = \boldsymbol{L}^{CC} \tag{6.31a}$$

$$\boldsymbol{f}^w = \boldsymbol{K}^E\boldsymbol{u}^E, \tag{6.31b}$$

where

$$\boldsymbol{K}^E = \boldsymbol{L}^{CE}.$$

6.5.2 Contact between two elastic bodies

The procedure outlined in Section 6.5.1 could be extended to solve contact problems involving two contacting bodies by idealising the problem as a series of single body problems. Assuming the body makes contact at a set of N contact nodes, the initial step requires creation of separate finite element models of two bodies, taking care to locate the contact nodes at the same points on the interface. The global stiffness matrix of each body is extracted separately and the reduced contact stiffness matrix and load vectors are then computed for the respective bodies.

The reduced contact stiffness matrix for a body with a rigid body mode is singular, which is numerically ill-conditioned. The two body contact problem is formulated based on the restriction that at least one of the reduced stiffness matrix for a body is non-singular. Therefore, in most cases one of the contacting bodies will be externally supported and the other would have rigid body degrees of freedom. In this scenario the body with rigid body modes is designated as index 1, whereas the restrained body is designated as 2. If both of the contacting bodies are

externally supported then the following formulation will work, irrespective of how the bodies are numbered.

The sign convention detailed in Figure 6.3 is adopted for each body separately. Therefore, along the contact interface, p_j^1 and p_j^2 are both compressive nodal forces and directed towards the interior of the respective bodies. The indices 1 and 2 refers to the body to which the component pertains. With this sign convention when two bodies are placed in contact, Newton's third law requires that $p_j^1 = p_j^2$ and $q_j^1 = q_j^2$, which is equivalent to the statement $f_1^C = f_2^C = f^C$. With this assumption, the subscripts 1 and 2 in the force vector are in-significant and hence can be conveniently dropped in the subsequent formulations. In geometric terms the sign conventions are enforced by the application of local right-handed x, y coordinate systems at each contact node in each body, with the $y-$axis directed in to the body.

Since the two elastic bodies make contact at a shared set of N contacting nodes, the procedure followed for single body (in contact with rigid body) problem is used to determine the reduced contact stiffness matrices K_1^C, K_2^C and the load vectors f_1^w, f_2^w for each body separately. The equilibrium equation as defined in (6.18) can be written for the bodies as (Thaitirarot [2013][100])

$$\boldsymbol{f}^C = \boldsymbol{f}_1^w + \boldsymbol{K}_1^C \boldsymbol{u}_1^C \tag{6.32a}$$

$$\boldsymbol{f}^C = \boldsymbol{f}_2^w + \boldsymbol{K}_2^C \boldsymbol{u}_2^C. \tag{6.32b}$$

Referring to the sign convention adopted in Figure 6.3, the normal and relative tangential (slip) displacements along the common set of nodal points for the full contact problem can be

written as

$$\boldsymbol{w}_j = \boldsymbol{w}_j^1 + \boldsymbol{w}_j^2 \tag{6.33a}$$

$$\boldsymbol{v}_j = \boldsymbol{v}_j^1 + \boldsymbol{v}_j^2, \tag{6.33b}$$

which is equivalent to the condition

$$\boldsymbol{u}_c = \boldsymbol{u}_c^1 + \boldsymbol{u}_c^2. \tag{6.34}$$

The reduced contact stiffness matrix $\boldsymbol{K^C}$ for the two elastic bodies in contact can be simply determined by applying the displacement relationship (6.34) over the equilibrium equations (6.32a) and (6.32b). Solving equation (6.32b) for $\boldsymbol{u}_2^C$

$$[\boldsymbol{K}_2^C]\boldsymbol{u}_2^C = (\boldsymbol{f}^C - \boldsymbol{f}_2^w)$$

$$\boldsymbol{u}_2^C = [\boldsymbol{K}_2^C]^{-1}(\boldsymbol{f}^C - \boldsymbol{f}_2^w). \tag{6.35}$$

Pre-multiplying equation (6.35) by K_1^C and using the relationship (6.34) for contact interface displacements results in

$$\boldsymbol{K}_1^C\boldsymbol{u}_2^C = \boldsymbol{K}_1^C[\boldsymbol{K}_2^C]^{-1}(\boldsymbol{f}^C - \boldsymbol{f}_2^w) \tag{6.36a}$$

$$\boldsymbol{K}_1^C(\boldsymbol{u}^C - \boldsymbol{u}_1^C) = \boldsymbol{K}_1^C[\boldsymbol{K}_2^C]^{-1}(\boldsymbol{f}^C - \boldsymbol{f}_2^w) \tag{6.36b}$$

$$\boldsymbol{K}_1^C\boldsymbol{u}^C - \boldsymbol{K}_1^C\boldsymbol{u}_1^C = \boldsymbol{K}_1^C[\boldsymbol{K}_2^C]^{-1}(\boldsymbol{f}^C - \boldsymbol{f}_2^w) \tag{6.36c}$$

$$\boldsymbol{K}_1^C\boldsymbol{u}_1^C = \boldsymbol{K}_1^C\boldsymbol{u}^C - \boldsymbol{K}_1^C[\boldsymbol{K}_2^C]^{-1}(\boldsymbol{f}^C - \boldsymbol{f}_2^w). \tag{6.36d}$$

Using equation (6.32a)

$$\boldsymbol{f}^C - \boldsymbol{f}_1^w = \boldsymbol{K}_1^C \boldsymbol{u}^C - \boldsymbol{K}_1^C [\boldsymbol{K}_2^C]^{-1} (\boldsymbol{f}^C - \boldsymbol{f}_2^w) \tag{6.36e}$$

$$\boldsymbol{f}^C + \boldsymbol{K}_1^C [\boldsymbol{K}_2^C]^{-1} \boldsymbol{f}^C = \boldsymbol{f}_1^w + \boldsymbol{f}_2^w \boldsymbol{K}_1^C [\boldsymbol{K}_2^C]^{-1} + \boldsymbol{K}_1^C \boldsymbol{u}^C \tag{6.36f}$$

$$\boldsymbol{f}^C \left[\boldsymbol{K}_1^C [\boldsymbol{K}_2^C]^{-1} + I \right] = \boldsymbol{f}_1^w + \boldsymbol{f}_2^w \boldsymbol{K}_1^C [\boldsymbol{K}_2^C]^{-1} + \boldsymbol{K}_1^C \boldsymbol{u}^C, \tag{6.36g}$$

Where I is the identity matrix. The above equation can be inverted to yield a relation of the form of the equilibrium equation (6.18), with

$$\boldsymbol{K}^C = \left[\boldsymbol{K}_1^C [\boldsymbol{K}_2^C]^{-1} + I \right]^{-1} \boldsymbol{K}_1^C \tag{6.37}$$

$$\boldsymbol{f}^w = \left[\boldsymbol{f}_1^w + \boldsymbol{f}_2^w \boldsymbol{K}_1^C [\boldsymbol{K}_2^C]^{-1} \right] \left[\boldsymbol{K}_1^C [\boldsymbol{K}_2^C]^{-1} + I \right]^{-1}. \tag{6.38}$$

6.6 Partitioning of reduced contact stiffness matrix

The preceding operations outlined in Sections 6.5.1 and 6.5.2, yield a reduced stiffness matrix with size $(2N \times 2N)$, whose components are arranged as per the respective nodal degrees of freedoms. The force and displacement vectors in this default arrangement can be written in terms of normal and tangential components as

$$\boldsymbol{f}^C = \{q_1, p_1, q_2, p_2, q_3, p_3, ..., q_N, p_N\}^T \tag{6.39a}$$

$$\boldsymbol{u}^C = \{v_1, w_1, v_2, w_2, v_3, w_3, ..., v_N, w_N\}^T. \tag{6.39b}$$

This can be inconvenient for many operations downstream and hence a more sensible approach would be to group the normal and tangential degrees of freedom as given in the following

equations (6.40a) and (6.40b).

$$\boldsymbol{f}^C = \left\{ \; q_1, q_2, q_3, ..., q_N, p_1, p_2, p_3, ..., p_N \; \right\}^T \tag{6.40a}$$

$$\boldsymbol{u}^C = \left\{ \; v_1, v_2, v_3, ..., v_N, w_1, w_2, w_3, ..., w_N \; \right\}^T . \tag{6.40b}$$

The above reorganization of the force and displacement vector leads to movement of terms in the reduced contact stiffness matrix K^C, which after partitioning can be written as

$$K^C = \begin{bmatrix} \boldsymbol{A} & \boldsymbol{B}^T \\ \boldsymbol{B} & \boldsymbol{C} \end{bmatrix} . \tag{6.41}$$

Therefore the force displacements relation after this reorganization can be written as

$$\begin{Bmatrix} \boldsymbol{q} \\ \boldsymbol{p} \end{Bmatrix} = \begin{bmatrix} \boldsymbol{A} & \boldsymbol{B}^T \\ \boldsymbol{B} & \boldsymbol{C} \end{bmatrix} \begin{Bmatrix} \boldsymbol{v} \\ \boldsymbol{w} \end{Bmatrix} + \begin{Bmatrix} \boldsymbol{q^w} \\ \boldsymbol{p^w} \end{Bmatrix} . \tag{6.42}$$

The reduced contact stiffness matrix K^C must be symmetric, which means that the submatrices A, C are symmetric, but B is generally not symmetric. Note that the submatrix B signifies the coupling between the tangential displacements and normal reactions and they obey the condition $B \neq B^T$. A frictional elastic contact problem is described as 'uncoupled' if and only if the matrix $B = 0$. When $B \neq 0$ the problem becomes coupled and this has important consequences for frictional elastic systems under periodic loading.

6.7 Time evolution solution algorithm for frictional Quasi-static contact problems

6.7.1 Introduction

If an elastic system is subjected to external loads that vary slowly in comparison with the period of the lowest natural frequency, it is possible to predict its behaviour using a quasi-static analysis in which the mass of the system is neglected and the structure is assumed to pass through a sequence of equilibrium states (Young [2009][101]). However, if friction exists at the contact interface, Couloumb friction law must also be considered. Furthermore, if the system with frictional interface experiences time varying cyclic loads which tend to produce micro-slip in certain contact areas but not all of the contact interface, it is very much important to identify the behaviour, since erosion of the surface and a failure known as fretting fatigue are closely related to it. Therefore, a numerical algorithm capable of tracking the behaviour of a system with frictional interfaces is essential.

The quasi-static contact problem can be set-up as either as a single elastic body in contact with a rigid surface or as a elastic body in contact with another elastic body. The stiffness matrix is extracted and reduced as per the method described in Sections 6.5.1 and 6.5.2 respectively. The iterative solution algorithm proposed by Ahn et al., [2008][99] is adopted to solve the inequalities and subsequent computation of displacements and reactions over the contact interface.

6.7.2 Frictional constraints

Once the reduced stiffness matrix $\boldsymbol{K^C}$ and the time varying external nodal force vector $\boldsymbol{f^w(t)}$ has been determined, the problem becomes equivalent to that of a set of N massless blocks in potential contact with a set of rigid plane obstacles. At any given point of time t in the loading cycle, each contact node i must be in one of the four states, which are then defined by the following relationships governed by Coulomb's friction law (Klarbring et al., [2007][102]).

Stick:

The node is in contact and there is no relative motion observed between the particles at these nodes and hence the equation becomes

$$w_i = 0; \quad \dot{v}_i = 0. \tag{6.43}$$

For this state to hold, the normal reaction must be compressive and the tangential reaction must satisfy the Coulomb's frictional in-equality, giving

$$p_i > 0; \quad -fp_i \leq q_i \leq fp_i. \tag{6.44}$$

Separation:

The node is out of contact and hence the reaction forces are zero leading to the equations

$$p_i = 0 \quad q_i = 0. \tag{6.45}$$

The normal displacement i.e, the vertical distance between the respective contact points should be non-negative, which requires

$$w_i > 0. \tag{6.46}$$

Forward slip:

The node is in contact and slipping to the right and so the displacements become

$$w_i = 0; \quad \dot{v}_i \geq 0. \tag{6.47}$$

The normal reaction should be compressive and since the tangential traction opposes the direction of motion it assumes a negative value.

$$p_i > 0; \quad q_i = -fp_i. \tag{6.48}$$

Backward slip:

The node is in contact and slipping to the left. The tangential traction is positive as it points towards the direction of motion.

$$w_i = 0; \quad \dot{v}_i < 0; \quad p_i > 0; \text{ and } q_i = fp_i \tag{6.49}$$

6.7.3 Solution procedure

As part of the static reduction procedure, the internal degrees of freedoms of the discretized elastic body are eliminated, and hence the resulting reactions along the contact interface may be written in the form

$$\boldsymbol{f}^C = \boldsymbol{f}^w + \boldsymbol{K}^C \boldsymbol{u}^C \tag{6.50}$$

where

$$\boldsymbol{q} = [q_i]^T, \boldsymbol{p} = [p_i]^T, \boldsymbol{v} = [v_i]^T, \boldsymbol{w} = [w_i]^T, \boldsymbol{f^C} = [\boldsymbol{q}^T, \boldsymbol{p}^T]^T, u^C = [\boldsymbol{v}^T, \boldsymbol{w}^T]^T.$$

The solution of the frictional contact problems under any transient loading $p_0(t)$ and $q_0(t)$ can be stated and solved in terms of the variables defined in equation (6.50), making use of the frictional constraint equations (6.43) to (6.49). The problem is solved at a series of time increments t_j in which case the stick condition $\dot{v} = 0$ in equation (6.43) translates to

$$v_i(t_{j+1}) = v_i(t_j). \tag{6.51}$$

The frictional inequalities $\dot{v}_i > 0$ and $\dot{v}_i < 0$ represented in equations (6.47) and (6.49) translate respectively to

$$v_i(t_{j+1}) > v_i(t_j) \quad \text{and} \quad v_i(t_{j+1}) < v_i(t_j). \tag{6.52}$$

Therefore, if the state of the system is completely known at time t_j, then equations (6.43) to (6.49) provide a set of conditions sufficient to determine the state of the contact at time t_{j+1}.

6.7.4 Algorithmic setting

The algorithm proposed by Ahn and Barber [2008][99] is considered for the solution phase, which relies on the basic assumption that the nodal displacements are updated one by one, while those at other nodes remain unchanged. At each time step, the algorithm cycles through the entire set of contact nodes several times until the governing equations at all nodes are satisfied against a set tolerance. A block diagram of the proposed algorithm is given in Figure 6.4. For the update procedure, the state (stick, forward slip, backward slip or separation) at the node in question is assumed to be inherited from the previous iteration. The corresponding

equations are then solved and the appropriate inequalities are checked. If the inequalities are not satisfied, the state assumption is changed and the node is solved again.

As mentioned by Ahn and Barber [2008][99], the system memory is entirely contained in the instantaneously locked-in displacements in the stick regions and this memory is acquired at times when any node makes the transition from slip or separation to stick. Such a transition normally occurs at a time interval between t_j and t_{j+1} and hence the accuracy of the stored displacements depends on the time step (or more strictly the load increment) being small enough for this to have a negligible effect on the solution. When the transition occurs from separation to stick, a better approximation is achieved by first identifying the position of node predicted under the zero traction assumption. If there is to be a transition to contact, this will involve a negative gap. By assuming a linear trajectory from the previous position of the node, the point of first contact can be established and this could then be used to compute the tangential nodal displacement at the newly stuck node.

The iteration at each time step is terminated when the changes Δv_i, Δw_i in the displacements v_i, w_i at all slipping and separated nodes during the last iteration are less than a given proportion of the corresponding displacement. In other words, when $\epsilon < \epsilon_0$, where

$$\epsilon = \underset{v_i, w_i}{max} \left(\frac{\Delta v_i}{v_i}, \frac{\Delta w_i}{w_i} \right) \tag{6.53}$$

Summary of steps involved in solution algorithm

The implementation of the time evolution solution algorithm is summarized as follows:

(i) Assume the initial state to be 'stick' for all the nodes.

(ii) Assume previous state for all the nodes at the start of the iteration and let the displacements be denoted as u^{prev}.

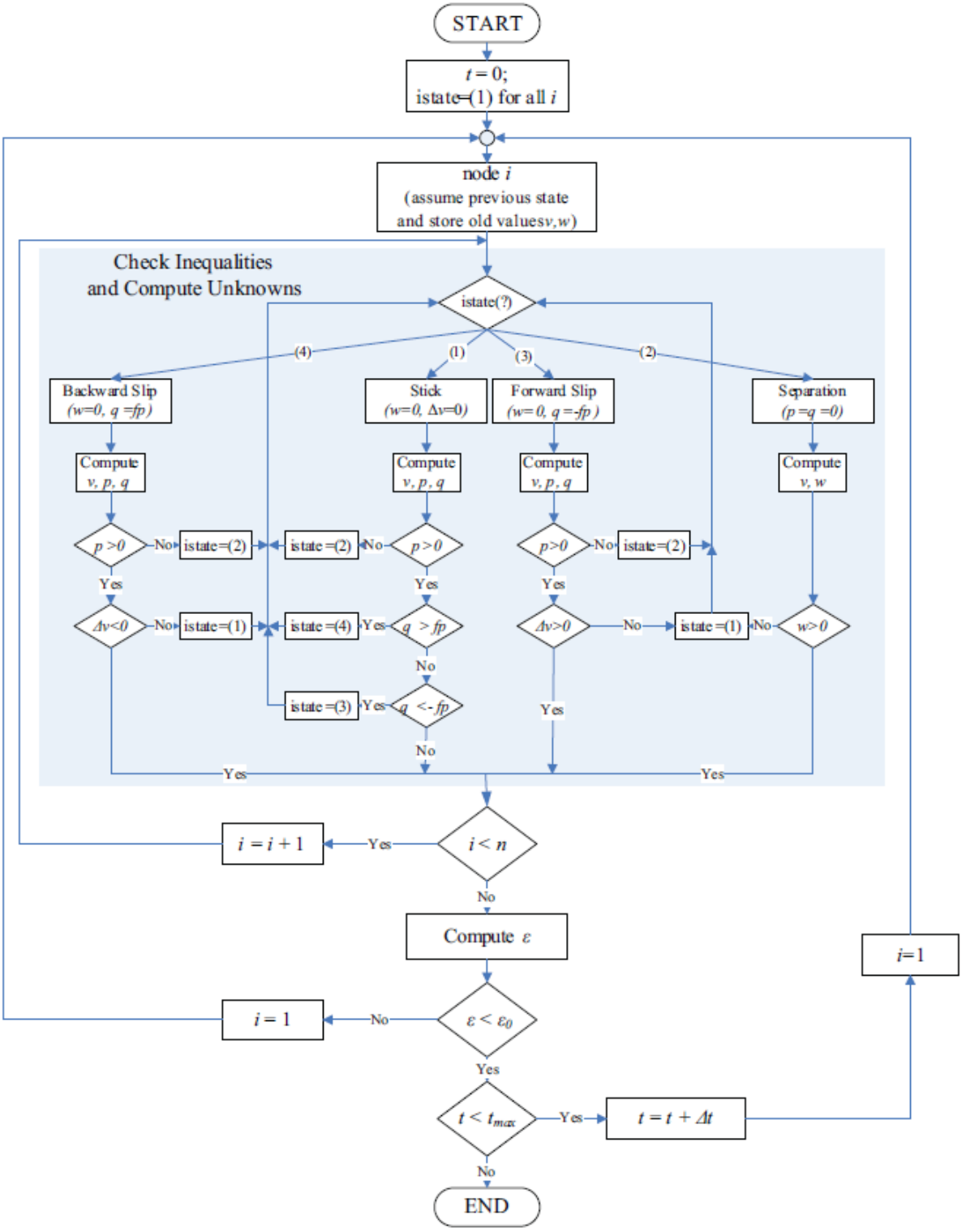


Figure 6.4: Solution algorithm based upon Gauss Seidel procedure described in Ahn [2009][101]

(iii) Calculate unknowns at node i.

(iv) Check inequality at node i.

(v) Change the state at node i if any inequality is violated.

(vi) Repeat step (iii) to (v) until the inequality is satisfied.

(vii) Let the new displacements calculated at step (iii) be denoted as u^{cur}.

(viii) Compute tolerance $\epsilon = u^{cur} - u^{prev}$ at node i.

(ix) Move to node i+1 and repeat the same procedure.

(x) Check convergence criterion ($\epsilon < \epsilon_0$) after cycling through all the nodes $i = 1 \sim N$.

(xi) If convergence not achieved, start again at node i until the tolerances are satisfied

(xii) Go to the next time step if convergence is achieved and repeat the same procedure listed above.

6.7.5 Application of Static Reduction procedure to example numerical models

6.7.6 Introduction

The proposed static reduction method (§6) and the quasi-static solution algorithm (§6.7) have been implemented into a structural finite element program called SC03 [103], in the form of a plugin. In order to verify the validity of the above formulations, the following examples are considered and analysed: (*i*) the frictional contact of an elastic (trapezoidal) block in contact with a rigid plane (*ii*) the frictional contact between two elastic (trapezoidal) blocks. The purpose of these examples is to demonstrate how the developed algorithm is capable of simulating different contact phenomena such as sticking and slipping conditions for a single and two body elastic contacts respectively. In addition, the sensitivity of the contact behaviour with respect to different parameters like normal load, shear traction, coefficient of friction and Poisson's ratio have been studied. The validity of the implemented method is confirmed through the comparison of these results with the corresponding results obtained through ABAQUS and SC03. At the current level of implementation, only complete contact models with contact degrees of freedom aligning along the global axes are considered.

6.7.7 Frictional contact of an elastic block in contact with a rigid plane

Figure 6.5 shows a trapezoidal elastic block in contact with a flat surface, which is taken to be perfectly rigid. The block is loaded with a normal force $\boldsymbol{P}$ which is uniformly distributed along the top surface of the block. The coefficient of friction between the contact interfaces is maintained as 0.2. A finite element model of the block was developed with 40 nodes in

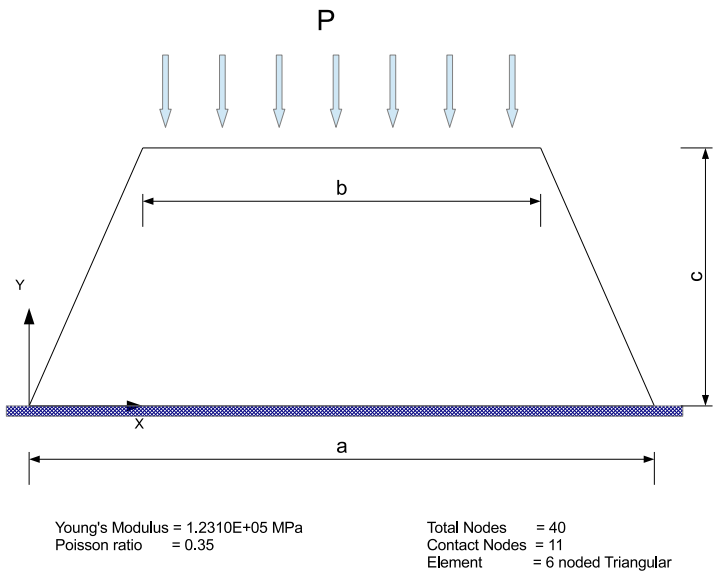


Figure 6.5: Geometry of an elastic body in contact with rigid plane surface

total and 11 nodes along the contact interface. Therefore the size of the stiffness matrix $\boldsymbol{K}$ for the full model becomes 80×80, whilst the statically reduced matrix $\boldsymbol{K^C}$ is only 22×22. In SC03, the single body contact was modelled essentially as a two body contact, with the stiffness moduli of the lower body intentionally given an infinite value to simplify the problem to a state where a single elastic body makes contact with a rigid plane. Figure 6.6 shows the tangential contact displacements plotted along the contact interface when the normal load $\boldsymbol{P}$ alone is applied. As expected, the distribution of slip displacements is anti-symmetric with a central stick region. The leading edge on the right edge suffers forward slip, while the trailing edge slips in the negative direction. An equivalent finite element model was created in ABAQUS, with the rigid body contact modelled as an Analytical rigid. Similar behaviour is predicted by ABAQUS, with the relative slip displacements (CSLIP1) seems to be in good agreement with the corresponding plugin results (refer Figure 6.6).

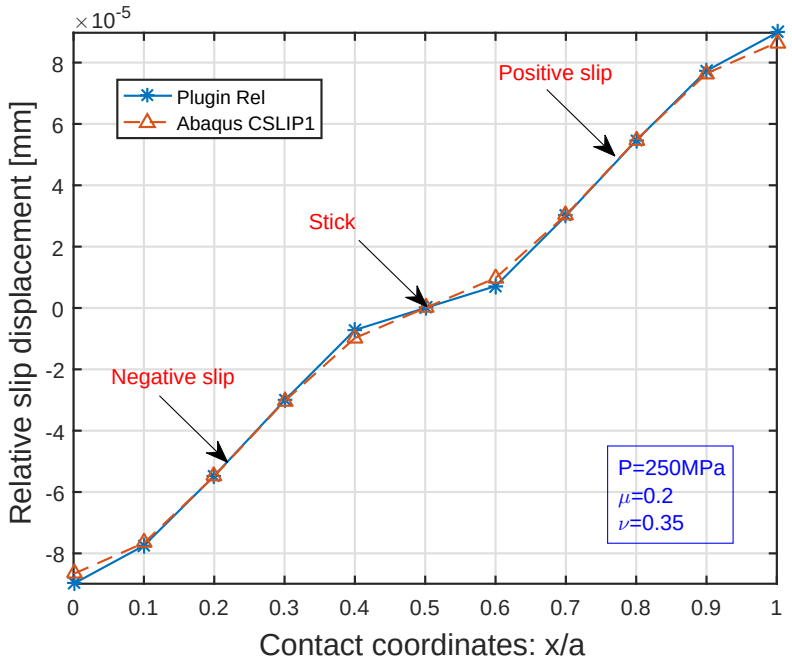


Figure 6.6: Evolution of slip behaviour for elastic-rigid type of contact, along with ABAQUS comparison

6.7.8 Frictional contact of an elastic body in contact with another elastic body

The example shown in Figure 6.7 explains the case where two elastic bodies are pushed into contact. The problem considered in Figure 6.5 is treated again, but in this case the rigid plane obstacle is replaced by an identical elastic body with same material properties. The finite element model of this contact problem is generated with 73 nodes and 11 contact nodes. Subsequent application of the static reduction procedure results in the stiffness matrix size being reduced from 146×146 to 22×22.

Figure 6.8 displays the slip displacements are plotted for different values of normal load $\boldsymbol{P}$. It is evident that as the normal load is increased, leading edge slip increases in the forward direction and trailing edge slip increases in the reverse direction. ABAQUS simulation produces

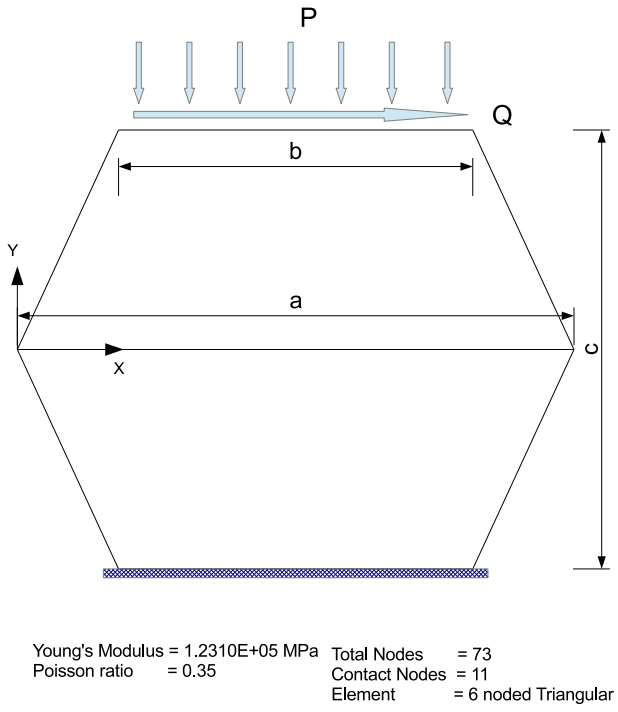


Figure 6.7: Geometry of an elastic body in contact with another elastic body

a similar behaviour, nevertheless gives appreciable differences with plugin results near the leading and trailing edges where the slip displacements reaches maximum value. Further it is clear that the plugin predicts an extended central stick region, whereas ABAQUS shows a sticking effect at the middle node alone, with the rest of the nodes in the neighbourhood suffers minimal slip. The results reported by Thaitirarot [2013][104] reveals the same extended stick region for both the single and two body elastic contact problems and verifies the consistency of the behaviour generated by the static reduction method. Intuitively we can further infer that the plugin results are comparably more accurate than its ABAQUS counterpart, due to the precise way in which the contact inequalities are resolved in a discrete manner by the Gauss Seidel algorithm. ABAQUS on the other hand, introduces approximations in the solution through the

imposition of penalty and augmented Lagrangean terms and hence may be computationally less accurate. The results could match still closer had a denser mesh been used. At the current stage of implementation, this seems to be an expensive option computationally and needs additional sparse matrix features to relax the restrictions imposed on the matrix operations handled in the code.

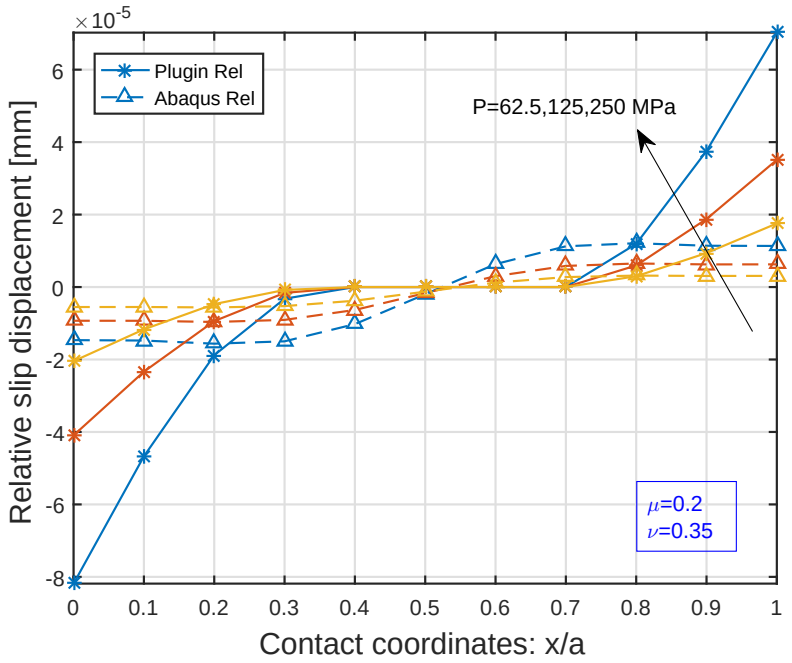


Figure 6.8: Plot of relative slip displacements for elastic-elastic type of contact at different levels of normal load (with ABAQUS comparison)

It is clear from the above formulation (refer section 6.5.2), that the plugin displacement results are outputted in a relative format. An attempt was therefore made to compute the absolute slip displacement results to enable a comparison with SC03 global contact solver results. However the conversion to absolute displacements is not a straight-forward task and required to be completed in two phases (refer Figure 6.9). The first phase involves running the plugin and generating the constraint equations for the computed relative displacements. In the next phase, a non-contact model of the same geometry is created and constraint equations are

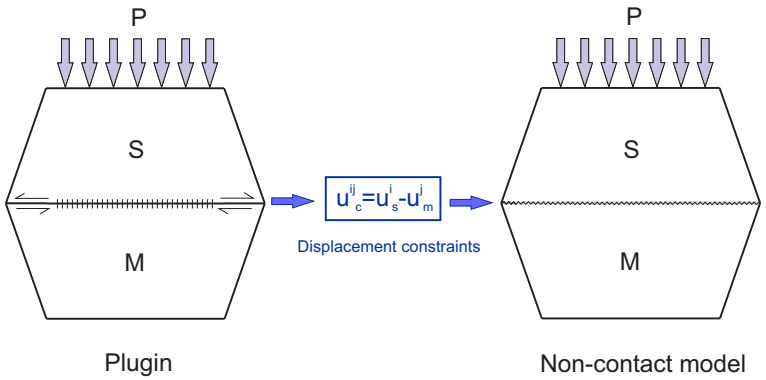


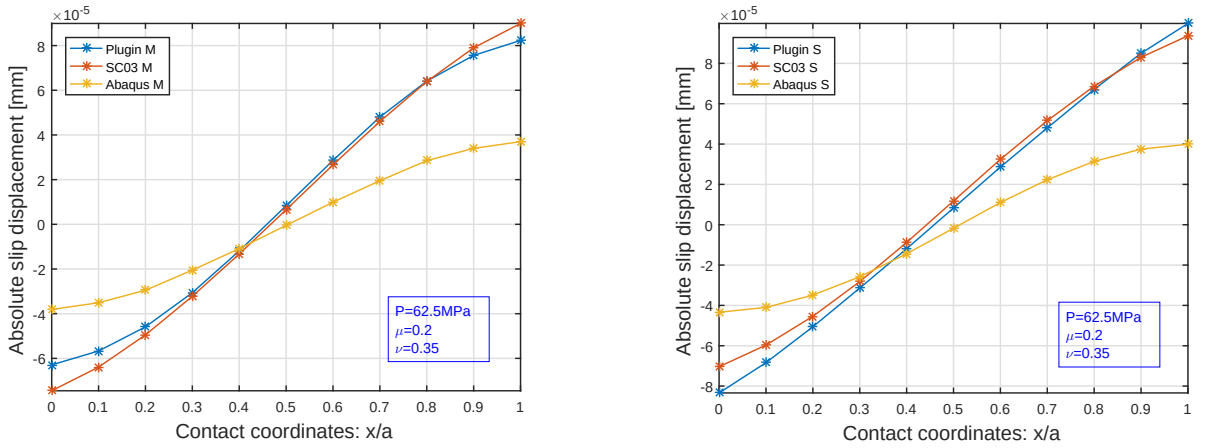
Figure 6.9: Mechanism of conversion of plugin relative displacements to absolute values using constraint equations applied to contact nodes in SC03

enforced at the respective nodal locations of the contact interfaces. Running a static analysis on the non-contact model generates the absolute displacements, restricted to the values dictated by the relative displacements present in the constraint equations. The plugin absolute results were subsequently compared with the respective results for SC03 and ABAQUS for both contacting interfaces [1] and are given in Figure 6.10. Comparison reveals a close agreement between the plugin and SC03 displacements, with ABAQUS results varying slightly near the edges and are consistent with the relative results shown in Figure 6.8.

The conversion to absolute displacements facilitates the computation of global resultants for the plugin results and a further comparison of the contour plots. From Figure 6.11, it is clear that the contour plot of tangential displacements remains identical for all the finite element codes SC03, Plugin and ABAQUS. The maximum and minimum values are observed along the RHS and LHS edges, suggesting the presence of forward and reverse slip in the neighbourhood regions. From Figure 6.12 we see that the stress contours in the tangential direction remains nearly same for all the cases, with the maximum values observed in the interior of the contact, say at $x/a \simeq 0.2 - 0.6$. The plugin stresses reach maximum values at x spatial location slightly

[1] Note that the slave and master contact interfaces could be identified in the upper body and lower bodies respectively and are referred by the sign conventions 'S' and 'M' throughout the chapter

before the other two cases SC03 and ABAQUS, due to the high values of slip near the edges. A summary of maximum/minimum values of the displacement and stress components in the 'x' direction for the finite element codes Plugin, SC03 and ABAQUS is given in Table 6.1.



(a) Absolute slip displacements for master interface

(b) Absolute slip displacements for slave interface

Figure 6.10: Comparison of absolute slip displacements between the finite element codes Plugin, SC03 and ABAQUS

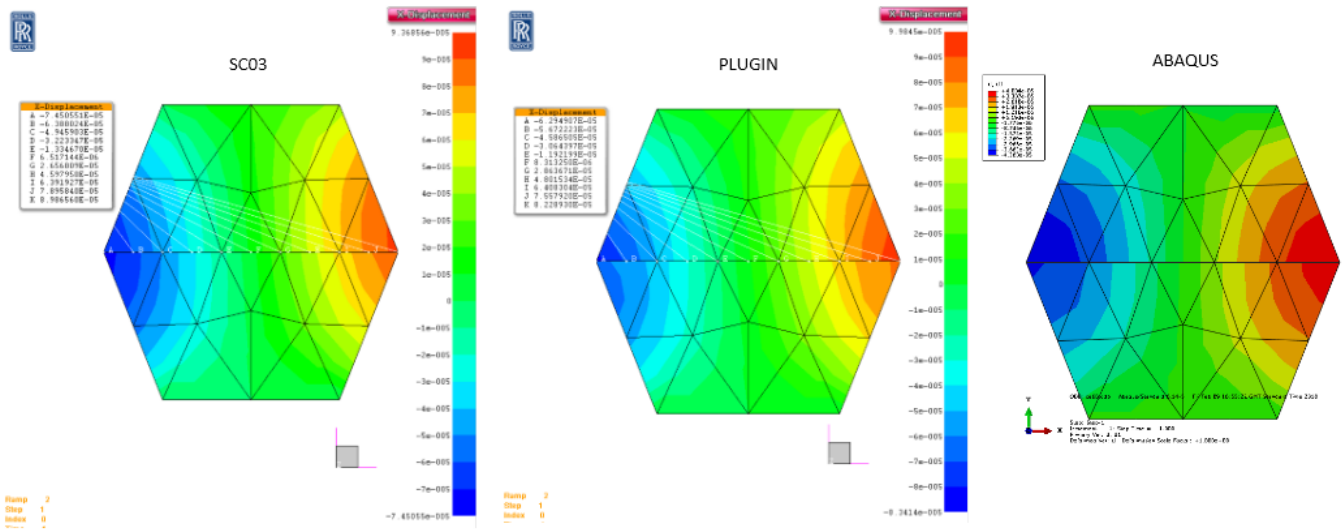


Figure 6.11: Comparison of displacement contours in the tangential direction between the finite element codes SC03, Plugin and ABAQUS

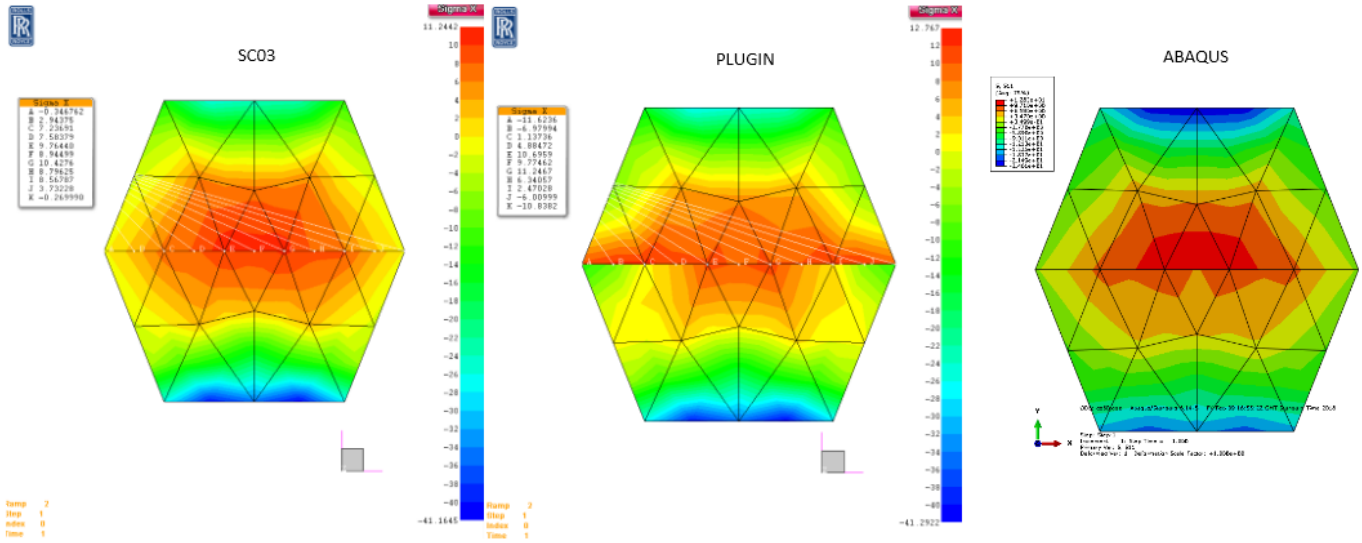


Figure 6.12: Comparison of stress contours in the tangential direction between the finite element codes SC03, Plugin and ABAQUS

	Plugin		**SC03**		**ABAQUS**	
	u_x	σ_x	u_x	σ_x	u_x	σ_x
Max	9.98×10^{-5}	12.767	9.37×10^{-5}	11.24	4.0×10^{-5}	12.83
Min	-8.34×10^{-5}	−41.29	-7.45×10^{-5}	−41.16	-4.36×10^{-5}	−24.61

Table 6.1: Summary of maximum/minimum values of the displacements and stress components (u_x and σ_x) for the finite element codes considered

The effect of coefficient of friction μ and Poisson's ratio, ν, on the contact behaviour is shown in Figures 6.13 and 6.14 respectively. At constant normal load $\boldsymbol{P}$, the simulation is run for several values of coefficient of friction and Poisson's ratio. With an increase in coefficient of friction the resistance to slip increases and hence the forward and backward slip decrease. On the other hand, an increase in Poisson's ratio causes more deformation in the tangential direction, resulting in an increased forward and backward slip along the leading and trailing edges respectively. It is further clear from the plot (Figure 6.14a) that ABAQUS results are not very sensitive to the effect of Poisson's ratio, although it shows a similar trend as that of the plugin. A zoomed-in version of the plot has been provided in Figure 6.14b for clear

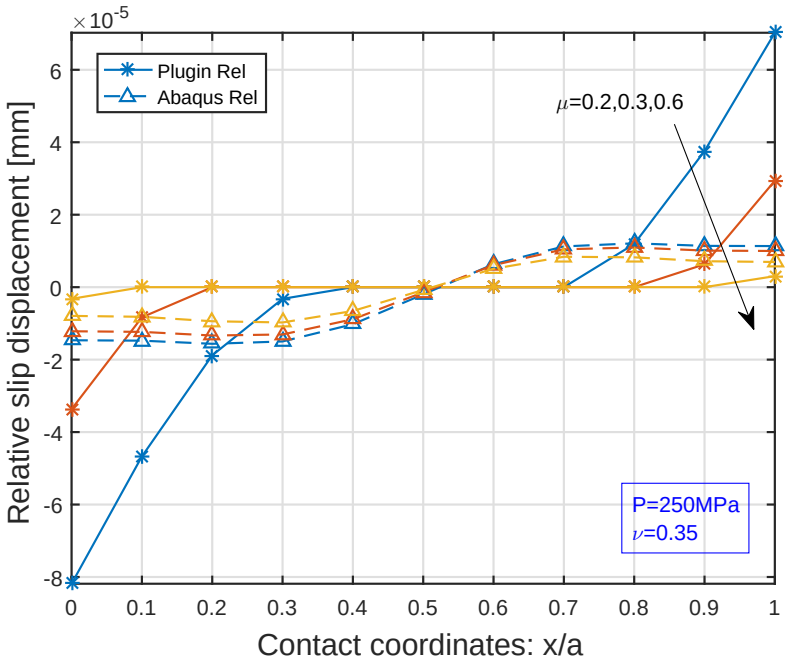
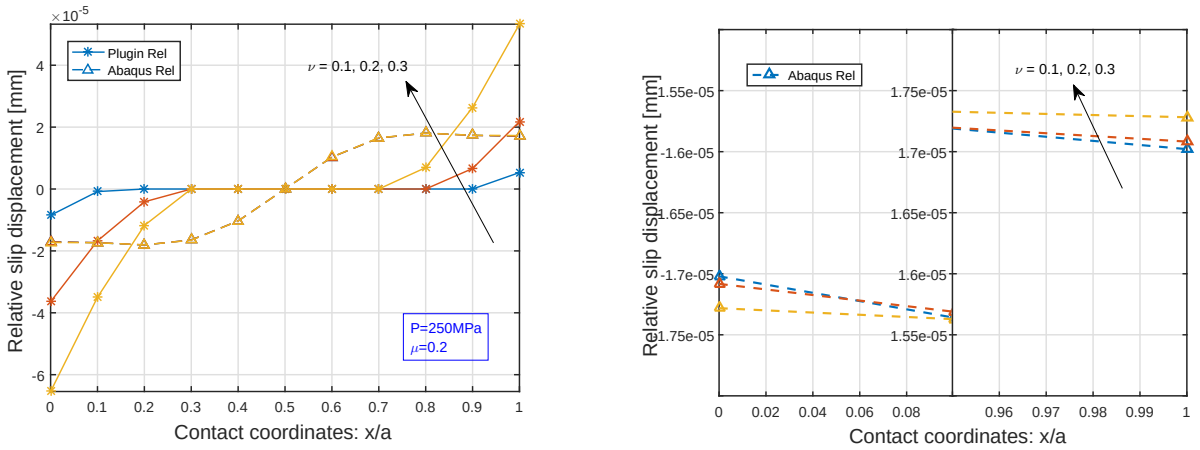


Figure 6.13: Plot of relative slip displacement for elastic-elastic type of contact at different levels of coefficient of friction μ (with ABAQUS comparison)

vizualisation of ABAQUS results near the edges of either ends of contact. ABAQUS results given in Figure 6.14 were generated using symmetric boundary conditions applied on the bottom edge of the lower contacting body. Earlier, the enforcement of ABAQUS encastre (fixed) boundary conditions reduces the reverse slip near the trailing edge, which is physically not admissible, unless a shear load is applied or if the material exhibits an anisotropic/orthotropic response.

Figure 6.15 displays the slip displacements for different values of shear traction $\boldsymbol{Q(t)}$ at constant normal load $\boldsymbol{P}$. The model is initially loaded with a normal force $\boldsymbol{P}$ which is uniformly distributed along the top surface of the block. A uniformly distributed shear traction $\boldsymbol{Q(t)}$ is then subsequently applied over the top of the block, and its magnitude is increased monotonically in time. As the shear traction is increased, the slip occuring near the leading edge area increases in the forward direction, while the reverse slip along the trailing edge decreases. This



(a) Slip displacements as a function of Poisson's ratio ν

(b) Zoomed in ABAQUS slip displacements near the edges of either ends of contact

Figure 6.14: Response of relative slip displacements for elastic-elastic type of contact at different values of Poisson's ratio (with ABAQUS comparison)

behaviour is mainly due to the fact that the trailing edge sticks upon the application of shear traction and this reduces the reverse displacement that is already present due to the normal load and this behaviour continues as the shear traction is increased in value. A comparison with ABAQUS results requires the line of action of the shear loads to be enabled statically along the contact interface. However due to restrictions in SC03 licence, a remote access to the software may not be possible and hence the method of load application could not be completed for a comparison with ABAQUS.

6.7.9 Conclusion

The static reduction method has been implemented in to Rolls-Royce proprietary finite element code SC03 in the form of a plugin, in order to study efficiently the contact behaviour of two dimensional, linear elastic, quasi-static frictional problems. At the present level of implementation only complete contacts with the contact interface aligning with the global axes are considered. Preliminary results indicates that this method is able to simulate the expected con-

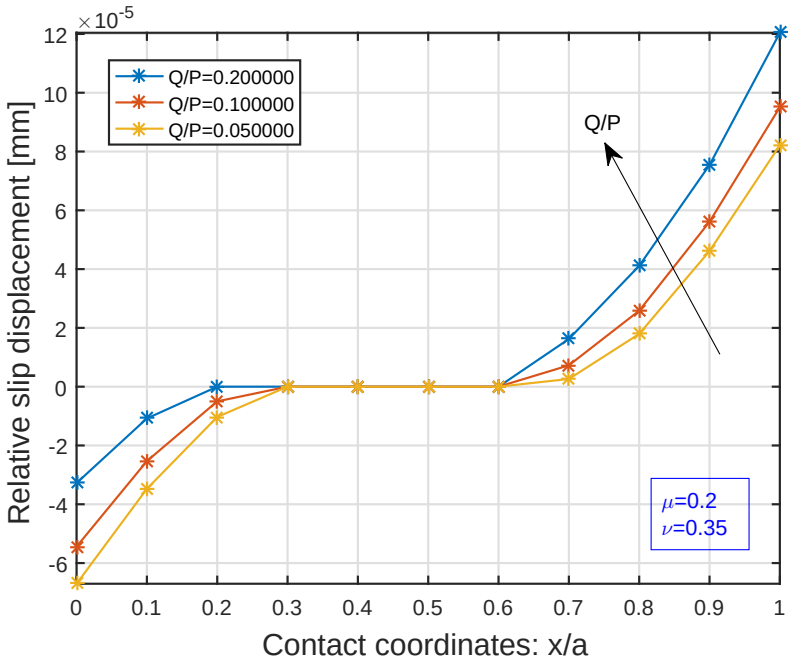


Figure 6.15: Plot of relative slip displacements for elastic-elastic type of contact at different levels of shear tractions

tact behaviour at reasonably good accuracy, when compared with SC03 (contact solver without static condensation method) and ABAQUS equivalent results. The matrix operations/calculations occurring in the code is currently handled in full format. This needs to be migrated completely to sparse format in order to gain some savings in execution time and therefore the comparison of computational effort was not performed at this point of time.

The fact that the plugin and SC03 results match closely indicates that the proposed static condensation method can be viewed as an effective alternate for the SC03 global contact solver, provided the enhancements identified for future course of work (in section 7.3) been implemented. A complete plugin solver with all the essential features could then be used to perform shakedown calculations, where series of repetitive simulations are required to identify the load factors necessary for the contacts to achieve frictional shakedown (Barber [2011][105]).

Chapter 7

Concluding remarks and future work

An outline of the thesis is presented in this chapter, followed by a summary of conclusions from each chapter. Future course of work is identified and recommendations have been made for further continuation of the work.

7.1 Overview

The work done in the thesis is concerned mainly with the analysis of fretting performance of complete contacts found in dovetail/fir-tree assemblies in an aero engine. The mechanics of contacting components in these assemblies is an extremely challenging problem, due to the presence of friction and extreme operating environments. The partial slip conditions occurring in the contacting interfaces accelerates the initiation and early propagation of cracks, causing a significant reduction in the fatigue life of the engineering components. Therefore, it is extremely critical to assess the fatigue performance of the components and it can be done by obtaining an accurate description of the stress state along the contact interface. Consequently the response of partial-slip, stick and separation resulting from application of external loads

must be established, which would then enable us to correlate against fretting performance.

It is to be noted, here, that the fretting cracks initiate near the edge of contact, which nevertheless produces huge stress intensities, particularly for the case of a completely adhered contact. This results in a very complex and multi-axial stress state, with steep gradients which may be difficult to represent using a standard numerical approach. However, asymptotic forms are extremely accurate in providing a description of the behaviour near the edge of contact and are given in Chapters §2-4. These asymptotic forms characterize the behaviour, when the edge of contact is present close to an adjacent stress concentrator, thereby providing an option to study the interaction between the resulting stress concentration effects.

However, there are certain instances where the edge results are not sufficient to characterize the behaviour of the contact, e.g., for the cases when there is interior slip or separation. For these specific cases, finite element results for the entire length of the contact would provide the necessary information. The finite element code developed using the static condensation method may be used as an effective alternative to solve for the entire length of contact problem, in addition to its intrinsic advantage of increased computation speed and reduced memory requirements. This method can also be used to analyse the steady state response of complete contacts, especially when subjected to cyclic loading.

Wedging behaviour occurs for certain cases of complete contacts on removal of applied loads and when the coefficient of friction is greater than a critical value. A finite element analysis of the blade root assembly has been performed to understand the behaviour and the results are compared with the analytical calculations.

7.2 Conclusion

A general form of complete contact was considered, with the edge of contact close to adjacent material and separated either infinitesimally or by a finite width. Enforcing material similarity and interfacial displacement continuity, the finite geometry to be studied was modelled as a bonded semi-infinite wedge of included angle 360^o. The proposed wedge model effectively models the dovetail geometry along with the socket end and considers the resulting interaction between stress concentration effects occurring near the edges in the enclosed region. If the side clearance is negligible, the width may be thought of as a crack and the semi-infinite crack eigen-solution is used to obtain the tractions along the adjacent contact interface. It is to be noted, here, that the resulting asymptotic stress field is self-similar, as the two eigen-solutions exert an equal influence on the behaviour of the edge of contact.

A finite problem in the form of a square block resting in an elastically similar rectangular trench is considered for initial analysis. Application of normal load alone reveals additional, important, components of stress field in the form of T-stress. The combination of applied external loads that results in edge separation and slip is calculated and compared with the results from a finite element analysis. For realistic coefficients of friction, the contact edge is found to be in a closed and adhered condition.

A generic solution was obtained to characterise the behaviour of the contact edge when a finite clearance is introduced between the block and the trench wall. A contact problem of a square block resting in a half-plane and formulated as a 270^o asymptote was studied previously, just to observe the behaviour when the finite width ratio $d/a \longrightarrow \infty$. Comparison with the 'closely fitting' solution reveals that the isolated block exhibits more stringent requirement for closure condition. The displacement components corresponding to T-stress was derived and included in the solution in the form of boundary conditions. Unlike the closely fitting solution,

the traction ratio here is a function of edge internal angle alone and therefore the minimum coefficient of friction needed for adhered conditions is calculated as 0.543 (if the block has 90^o corner).

A problem similar to the type of a square block resting in a trench is considered, but with a finite side clearance. The trench solution was validated to check the consistency of the results with the reference wedge solution for separate application of normal and shear loads. In the next phase, the normal and shear loads are applied together and the notch intensities obtained from the trench solution used to compute the interfacial traction ratio. Comparison with the finite element results reveals that the trench solution is extremely accurate near the edge and the trend continues over a distance greater than the width of the clearance but less than the next nearest length dimension. Further, we note that the tractions adjoining the edge of contact are not very sensitive to the presence of adjacent wall when normal loads are applied.

Analysis of contacts with inclined edges was conducted next, starting with the development of asymptotic forms for a contact internal angle of $\pi/4$ radians. The eigen solution for the edge reveals a requirement of un-realistic high coefficient of friction for adhered conditions and therefore the presence of edge slip is unavoidable for geometries of this inclination. This, however, is not the case for obtuse angled contacts with an internal angle of $3\pi/4$ radians. An elaborate discussion of asymptotic forms was done for all cases of edge clearances. Prediction of traction ratio response for various mixed mode conditions was performed for the semi-infinite trench geometry with a finite edge separation.

The punch geometries ($\pi/2, 3\pi/4, \pi/4$ radians) along with the contacting solids was considered separately and the behaviour of traction ratios along the entire length of the interface was studied for two extreme cases of separation i.e., when $d/a \longrightarrow \infty$ and 0. The comparison reveals that the tractions interior to the contact are substantially independent of the presence of adjacent material, except for the near edge region. Further comparison of results with finite

width geometry was done to check how relevant the trench method is in characterizing the behaviour of class of contacts. This reveals that the trench method is extremely accurate in predicting the tractions close to the contact edge, up to a length equivalent to $\sim 5\%$ of the total width of the contact from the edge and more appropriate for finite widths $d/a \lesssim 0.1$. The wedge asymptote gives an accurate description of the edge response when the distance between the block and trench is extremely large, $d/a \gg 1$. The crack asymptote provides an unique edge solution that depends on the mode mixity prevailing in the region and can be used when the clearance is negligible.

A prototype of static condensation method has been implemented as a plugin in to the Rolls-Royce proprietary finite element code SC03, to simulate the frictional response of two-dimensional, linear elastic frictional contact problems. The present version of the code contains very limited features and is intended to address contact problems where the interface more or less aligns with the global axis. The same code can also be used to run incomplete contact problems as long as the contact curvatures are not steep. Test models were created to validate the behaviour of the code for single and two body contact problems. A comparison was done with equivalent SC03 (global contact solver) and ABAQUS results to verify the accuracy of the slip response predicted by the plugin. An initial analysis reveals that the static condensation method generates results that are in good agreement with SC03 and ABAQUS contact solvers. However a measure of the computational speed was not performed, due to the pending implementation of sparse matrix features in the plugin code.

A closer analysis of results shows that the plugin and SC03 codes predict identical contact behaviour with good accuracy and thus enable static condensation method an effective alternate for the SC03 contact solver. A number of additional features were identified to improve the performance of the code in terms of speed and various other numerical aspects (Section 7.3). A complete plugin code with all these features could potentially be used to perform calculations

required to identify the load factors necessary for the contacts to achieve frictional shakedown.

The occurrence of self-wedging behaviour in complete contacts was investigated thoroughly, with particular attention to critical coefficient of friction f_c. Assuming force equilibrium conditions of the dovetail contact assembly, an expression was derived for the insertion and retention of the blade, in terms of the internal angle θ. The fraction of load removed to overcome the effect of wedging was quantified by a finite element simulation of the assembly. Further investigation was performed to study the effect of changing the following quantities: (a) Coefficient of friction (b) Internal contact angle of the blade component (c) Shape of the blade geometry. From the results, it seems obvious that wedging occurs in partial slip conditions when the coefficient of friction f is maintained greater than the critical coefficient of friction f_c, regardless of the detailed geometry of the contact. Further, the tendency of a contact to wedge increases with the internal angle θ for any given coefficient of friction. The wedging behaviour remains unchanged when the dovetail profile is changed, i.e., with addition of material. However appreciable differences were noticed with regards to the contact separation, slip and stick regimes.

7.3 Future work

Several pieces of work were identified for further continuation of research outlined in the thesis and are given here.

The asymptotic analysis of complete contacts carried out in this thesis focus mainly on the assumption that the contacting components are materially similar. However it would be interesting to notice the behaviour of the contact, when the components are made out of different materials. The solution procedure developed by Bogy [1968,1971][55] [106] must be used to investigate the behaviour of tractions in the near edge region, assuming adhered conditions.

Further research can be carried out by introducing a radius near the edges, so as to model realistically the contact assembly and study the resulting behaviour. It's quiet obvious that the radiused edge behaves incomplete regionally and that the contact pressure vanishes smoothly as it approaches the edge. A semi-infinite contact formulation could be developed to evaluate the contact length and maximum contact pressure along the curved region. An analysis could be performed to study the influence of the radius on the tractions neighbourhood of the flat region quantitatively. These would give an indication of the potential slip behaviour, which may lead to the violation of our initial adhered assumptions and further validity of the semi-infinite wedge and crack asymptotes to probe the edge behaviour. From Section §4.2 we note that for contacts with internal angle $\pi/4$, the edge would invariably slip for realistic coefficient of friction and might perhaps slide when the friction is minimal. A semi-infinite solution obtained by Gdoutos and Theocaris [1975][107] and by Comninou [1976][108] can be used to address the sliding wedge problems of these kind, which simulate precisely the intended behaviour.

The static reduction method is a finite element based approach to solve quasi-static frictional contact problems more efficiently and was implemented as a plugin for the Rolls-Royce proprietary finite element code. The current version of the code contains limited features and can run complete contact problems with very less degrees of freedom. Therefore several new features have been identified and considered for further development, in order to make the code more robust and run a variety of contact problems.

(i) At current level of implementation, the matrix operations during the solution phase is performed using conventional mode of storage mechanism. A conversion to sparse mode of storage is necessary to reduce significantly the computation time and memory usage.

(ii) The code currently works for a single time step in the computational chain of the program. More work is however needed to enable the code run properly within the chain, exchanging

information between the plugin and solution module of the core program.

(iii) The current version of code requires that the nodes are aligned, i.e., it occupies the same coordinates in the space, which is often considered a limitation when working with complicated models. Modern contact modelling approaches like node-to-node or node-to-surface etc., can be adopted to add more flexibility to the program, thereby reducing the burden on the user.

(iv) The present approach requires that the contact interface lies approximately along a straight line. This means that the code for complete (sharp edged) contacts can be used to run incomplete contact problems as long as the interfacial curvature is maintained minimal. The code however needs transformation of the partitioned stiffness matrices to the respective local coordinate systems for steep curvatures.

(v) The Gauss-Seidel solution algorithm need to be tuned to work for three dimensional problems, as there would be two potential tangential directions the node can move.

(vi) The code can be extended to include the effects of inertia, thereby allowing the dynamic reduction of mass matrices.

An analysis of wedging behaviour in complete contacts has been performed, assuming the edges to be sharp and materially similar. The response might vary significantly for the contacts with rounded edges and for the case where the materials are different. An investigation could therefore be done to check the effect of these entities on the wedging behaviour.

Bibliography

[1] W. Schütz. A history of fatigue. *Eng. Fract. Mech*, 54(2):263–300, 1996.

[2] F.M. Eden, W.N. Rose, and F.L. Cunningham. The endurance of metals: Experiments on rotating beams at university college. london. *Proc. Inst. Mech Eng*, 4:839–974, 1911.

[3] R.B. Waterhouse. A historical introduction to fretting fatigue. *Americal Society of Testing and Materials*, 1159:8–9, 1992.

[4] F.W. Carter. Railway electric traction. *Edward Arnold*, 1922.

[5] C. Cattaneo. Sul contactto di due corpi elsatici: dismush1953itribution local degli sfozi. *Reconditi dell accademia nazionale deMuskhelishvilii lincei*, 27:342–348, 434–436, 474–478, 1938.

[6] R.D. Mindlin. Compliance of elastic bodies in contact. *Journal of Applied Mechanics*, 16(3):259–268, 1949.

[7] N.I. Muskhelishvili. *Some basic problems of the mathematical theory of elasticity*. Noordhoff, Gröningen, 1953.

[8] N.I. Muskhelishvili. *Singular integral equations, Boundary problems of funtion theory and their application to mathematical physics*. Noordhoff, Gröningen, 1953.

[9] G.M.L Gladwell. Contact problems in the classical theory of elasticity. *Sijtoff and Noordhoff, Maryland, USA*, 1980.

[10] K.L Johnson. *Contact mechanics*. Cambridge university press, cambridge, 1985.

[11] D.A. Hills, D. Nowell, and J.J. O'Connor. On the mechanics of fretting fatigue. *Wear*, 125(1):129–146, 1988.

[12] J.R. Barber, A. Klarbring, and M. Ciavarella. Shakedown in frictional contact problems for the continuum. *C.R Mechanique*, 336:34–41, 2008.

[13] A. Klarbring and J.R. Barber M. Ciavarella. Shakedown in elastic contact problems with coulomb friction. *International Journal of Solids and Structures*, 44:8355–8365, 2007.

[14] J.R. Fleming and N.P. Suh. Mechanics of crack propagation in delamination wear. *Wear*, 44:39–56, 1977.

[15] J. Dundurs and M. Comninou. Some consequences of the in-equality conditions in contact and crack problems. *Journal of Elasticity*, 9:–, 1979.

[16] S.B. Liu and C.L. Tan. Two dimensional boundary element contact mechanics analysis of angled crack problems. *Engineering Fracture Mechanics*, 42:273–288, 1992.

[17] J. Jäger. A new principle in contact mechanics. *Journal of Tribology*, 120:677–684, 1998.

[18] M. Ciavarella. The generalised cattaneo partial slip plane contact problem. i-theory. *International Journal of Solids and Structures*, 35(18):2349–2362, 1998a.

[19] M. Ciavarella. The generalised cattaneo partial slip plane contact problem. ii-examples. *International Journal of Solids and Structures*, 35(18):2363–2378, 1998b.

[20] C.M. Churchman and D.A. Hills. Slip zone length at the edge of complete contact. *International Journal of Solids and Structures*, 43:2037–2069, 2006.

[21] J.A. Greenwood and J.B.P. Williamson. Contact of nominally flat surfaces. *Proceedings of Royal Society of London*, 295:300–319, 1966.

[22] P.R. Nayak. Random process model of rough surfaces in plastic contact. *Wear*, 26:305–333, 1973.

[23] A.W. Bush, R.D. Gibson, and T.R. Thomas. The elastic contact of a rough surface. *wear*, 35:87–111, 1975.

[24] A.W. Bush, R.D. Gibson, and G.P. Keogh. Strongly anisotropic rough surfaces. *ASME Journal of Lubrication Technology*, 101:15–20, 1979.

[25] R.D. Gibson. The surface as a random process. *Rough Surfaces*, ed. T.R. Thomas Longman, London:–, 1982.

[26] X. Tian and B. Bhushan. A numerical three-dimensional model for the contact of rough surfaces by variational principle. *ASME Journal of Tribology*, 118:33–42, 1996.

[27] D.M. Bailey and R.S. Sayles. Effect of roughness and sliding friciton on contact stresses. *ASME Journal of Tribology*, 113:729–738, 1991.

[28] M.H. Yu and B. Bhushan. Contact analysis of three dimensional rough surfaces under frictionless and frictional contact. *Wear*, 200:265–280, 1996.

[29] T. Merriman and J. Kannel. Analysis of the role of surface roughness on the contact stresses between elastic cylinders with and without soft surface coating. *ASME Journal of Tribology*, 111:87–94, 1989.

[30] S.J. Cole and R.S. Sayles. A numerical model for the contact of layered elastic bodies with real rough surfaces. *ASME Journal of Tribology*, 114:334–340, 1992.

[31] J.T. Oden and J.A.C. Martins. Models and computational methods for dynamic friction phenomena. *Computer Methods in Applied Mechanics and Engineering*, 52:527–634, 1985.

[32] J.A.C Martins, J.T. Oden, and F.M.F. Simoes. A study of static and dynamic friction. *International Journal of Engineering and Science*, 28:29–92, 1990.

[33] J. Dundurs and M. Stippes. Role of elastic constants in certain contact problems. *Journal of Applied Mechanics*, 37(4):965–970, 1970.

[34] G. Amontons. De la résistance causée dans les machines. *Mémoires de l'Académie Royale, A*, pages 257–282, 1699.

[35] C.A. Couloumb. Theorie des machines simples, en ayant regard au frottement de leurs parties, et a la roideur des cordages. *Mem. Math. Phys.*, pages 161–342, 1785.

[36] D.A. Hills and D. Nowell. *Mechanics of fretting fatigue*. Kluwer academic publishers, 1994.

[37] O. Vingsbo and Söderberg. On fretting maps. *Wear*, pages 131–147, 1988.

[38] S. Fouvry, P. Kapsa, and L. Vincent. Quantification of fretting damage. *Wear*, pages 186–205, 1996.

[39] G.A. Tomlinson. The rusting of steel surfaces in contact. *Proceedings of Royal society of London*, 115(771):472–483, 1927.

[40] K. Nishioka and K. Hirkawa. Bull. *JSME*, 15:135–144, 1972.

[41] R. Bramhall. Studies in fretting fatigue. *DPhil thesis, University of Oxford*, 1973.

[42] D. Nowell, D. Dini, and D.A. Hills. Recent developments in the understanding of fretting fatigue. *Engineering fracture mechanics*, 73:207–222, 2006.

[43] C. Ruiz, P.H.B Boddington, and K.C. Chen. *Experimental mechanics*, 24:208–217, 1984.

[44] P. Papanikos and S.A. Meguid. *Fatigue Fracture Engineering Materials and Structures*, 17:539–550, 1994.

[45] C.H. Goh, J.M. Wallace, R.W. Neu, and D.L. McDowell. Polycrystal plasticity simulations of fretting fatigue. *International journal of fatigue*, 23:423–435, 2001.

[46] M. Zhang, R.W. Neu, and D.L. McDowell. Micro-structure sensitive modelling: Application to fretting contacts. *International journal of fatigue*, 31:1397–1406, 2009.

[47] O.J. McCarthy, J.P. McGarry, and S.B. Leen. The effect of grain orientation on fretting fatigue plasticity and life prediction. *Tribology international*, 76:100–115, 2014.

[48] D. Nowell, D.A. Hills, and R. Moobala. Length scale considerations in fretting fatigue. *ASTM*, pages 141–153, 2000.

[49] H. Proudhan, S. Fouvry, and J.Y. Buffiere. A fatigue crack initiation prediction taking in to account the surface roughness and the crack nucleation process volume. *International journal of fatigue*, 27:569–579, 2005.

[50] D.A. Hills, A. Thaitirarot, J.R. Barber, and D. Dini. Correlation of fretting fatigue experimental results using an asymptotic approach. *International Journal of Fatigue*, 43:62–75, 2012.

[51] R. Khadem and J.J. O'Connor. Adhesive or frictionless compression of an elastic rectangle between two identical elastic half-spaces. *International Journal of Engineering Science*, 7(2):153–168, 1969a.

[52] R. Khadem and J.J. O'Connor. Axial compression of an elastic circular cylinder in contact with two identical elastic half spaces. *International Journal of Engineering Science*, 7(8):785–800, 1969b.

[53] A. Mugadu and D.A. Hills. The evolution of the process zone when a complete contact is subject to cyclically varying loads. *International Journal of Solids and Structures*, 40:4417–4435, 2003.

[54] M.L. Williams. Stress singularities resulting from various boundary conditions in angular corners of plates in extension. *Journal of Applied Mechanics*, 19(4):526–528, 1952.

[55] D.B. Bogy. Edge-bonded dissimilar orthogonal elastic wedges under normal and shear loading. *Journal of Applied Mechanics*, 35(3):460–466, 1968.

[56] E.E. Gdoutos and P.S. Theocaris. Stress concentrations at the apex of a plane indenter acting on an elastic half plane. *Journal of Applied Mechanics*, 42(3):688–692, 1975.

[57] M. Comninou. Stress singularity at a sharp edge in contact problems with friction. *Journal of Applied Mathematics and Physics*, 27(4):493–499, 1976.

[58] A. Mugadu, D.A. Hills, and L. Limmer. An asymptotic approach to crack initiation in fretting fatigue of complete contacts. *Journal of Mechanics and Physics of Solids*, 50:531–547, 2002.

[59] S. Karuppanan. *Dissertation: Analysis of incomplete and complete contacts in sliding and partial slip.* Department of engineering science, Oxford, 2007.

[60] C.M. Churchman and D.A. Hills. General results for complete contacts subject to oscillatory shear. *Journal of Mechanics and Physics of Solids*, 54:1186–1205, 2006.

[61] S. Karuppanan, C.M. Churchman, D.A. Hills, and E. Giner. Sliding frictional contact between a square block and an elastically similar half-plane. *European Journal of Mechanics A/Solids*, 27:443–459, 2008.

[62] R.C. Flicek, D.A. Hills, and D. Dini. Sharp edged contacts subject to fretting: A description of corner behaviour. *International Journal of Fatigue*, 71:26–34, 2015.

[63] C. Navarro, A. Mugadu, D.A. Hills, and J. Dominguez. The influence of underlying tension on partial slip in complete and nearly complete contacts. *International Journal of Mechanical Sciences*, 45:757–773, 2003.

[64] R.P. Cartwright, R.J.H. Paynter, D.A. Hills, and D. Nowell. Long term wear of complete contacts subject to fretting. *Wear*, 271:2821–2825, 2011.

[65] D.A. Hills, R.J.H. Paynter, and D. Dini. An overview of the quantification of fretting fatigue lives of complete contacts. *Engineering Fracture Mechanics*, 80:3–12, 2012.

[66] J. Juoksukangas, A. Lehtovaara, and A. Mantyla. The effect of contact edge geometry on fretting fatigue behaviour in complete contacts. *Wear*, 308:206–212, 2013.

[67] D.A. Hills, P.A. Kelly, D.N. Dai, and A.M.Korsunsky. *Solution of crack problems: The distributed dislocation technique*. Springer, 1996.

[68] C.M. Churchman and D.A. Hills. The edge dislocation in a three-quarter plane. Part II: Application to an edge crack. *European Journal of Mechanics A/Solids*, 25:380–396, 2006.

[69] R.J.H. Paynter, D.A. Hills, and D. Dini. Separation and slip at the edge of complete contact: An asymptotic solution. *International Journal of Solids and Structures*, 47:2613–2619, 2010.

[70] N. Banerjee and D.A. Hills. Analysis of stick-slip and contact edge behaviour in a simplified fretting fatigue test. *Journal of Strain Analysis*, 41(3):183–192, 2006.

[71] E. Melan. Theorie statisch unbestimmter systeme aus ideal-plastichem Baustoff.Sitzungsber.d. Akad.d. Wiss. *Wien*, 2A(145):195–218, 1936.

[72] G. Bjorkman and A. Klarbring. Shakedown and residual systems in frictional systems. *Contact Mechanics and Wear of Rail/Wheel Systems II: Proceedings of the 2nd International Symposium*, pages 27–39, 1987.

[73] R.C. Flicek, D.A. Hills, J.R. Barber, and D.Dini. Determination of the shakedown limit for large, discrete frictional systems. *European Journal of Mechanics A/Solids*, 49:242–250, 2014.

[74] T.L. Anderson. *Fracture Mechanics: Fundamentals and Application*. CRC Press, 2005.

[75] B.R. Lawn and T.R. Wilshaw. *Fracture of brittle solids*. Cambridge university press, 1975.

[76] J.R. Barber. *Elasticity*. Kluwer academic publishers, 1992.

[77] D.A. Hills and D.Dini. What level of friction guarantees adhesion in a complete contact? *Journal of Strain Analysis in Engineering*, 39(5):549–551, 2004.

[78] D.A. Hills and D. Dini. Characteristics of the process zone at sharp notch roots. *International Journal of Solids and Structures*, 48(14–15):2177–2183, 2011.

[79] K. Jeong-Ho and G.H. Paulino. T-stress, mixed mode stress intensity factors, and crack initiation angles in functionally graded materials: A unified approach using the interation integral method. *Computer methods in applied mechanics and engineering*, 192:1463–1494, 2003.

[80] M.R. Ayatollahi, M.J. Pavier, and D.J.Smith. Determination of t-stress from finite element analysis for mode i and mixed mode i/ii loading. *International journal of fracture*, 91:283–298, 1998.

[81] R.C. Flicek, D.A. Hills, and D. Dini. Sharp edged contacts subject to fretting: A description of corner behaviour. *International Journal of Fatigue*, 71:26–34, 2015.

[82] B. Arun and D.A. Hills. Partial slip under complete contacts near adjacent corners. *International Journal of Strain Analysis*, pages –, 2017.

[83] H. Murthy, G.Harish, and T.N. Farris. Efficient modelling of fretting of blade/disk contact using load history effects. *Transactions of the ASME. Journal of Tribology*, 126(1), 2004.

[84] S. Berczynski and P.Gutowski. Identification of the dynamic models of machine tool supporting systems. Part I: An algorithm of the method. *Journal of Vibration and Control*, 12(3), 2006.

[85] S.S. Law, Z.M. Wu, and S.L.Chan. Analytical model of a slotted bolted connection element and its behaviour under dynamic load. *Journal of Sound and Vibration*, 292(3-5), 2006.

[86] L. Limmer, D. Nowell, and D.A. Hills. A combined testing and modelling approach to the prediction of the fretting fatigue performance of splined shafts. *Proc. Instn Mech Engrs*, 215(G), 2001.

[87] N. Banerjee and D.A. Hills. Analysis of stick-slip and contact edge behaviour in a simplified fretting fatigue test. *Journal of Strain Analysis*, 41(G), 2006.

[88] J.B. Walsh. A theoretical analysis of sliding of rough surfaces. *Journal of Geophysical Research*, 108(B8), 2003.

[89] E. Melan. Theorie statisch unbestimmter systeme aus ideal-plastichem Baustoff.Sitzungsber.d. Akad.d. Wiss. *Wien*, 2A(145):195–218, 1936.

[90] A. Klarbring, M. Ciavarella, and J.R. Barber. Shakedown in elastic contact problems with coulomb friction. *International Journal of Solids and Structures*, 44, 2007.

[91] J.R. Barber, A. Klarbring, and M. Ciavarella. Shakedown in frictional contact problems for the continuum. *C. R. Mecanique*, 336, 2008.

[92] *ABAQUS user manual*. Version 6.14.

[93] A. Murthy, G. Harish, and T.N. Farris. Efficient modelling of fretting of blade/disk contact including load history effects. *Journal of Tribology*, 126(1):56–64, 2004.

[94] R.C. Flicek, D.A. Hills, J.R. Barber, and D. Dini. Determination of the shakedown limit for large, discrete frictional systems. *European Journal of Mechanics A/Solids*, 49(2015):242–250, 2014.

[95] Mario Paz and William Leigh. *Static condensation and substructuring*. Kluwer academic publishers, 2001.

[96] R.J. Guyan. Reduction of stiffness and mass matrices. *The American Institute of Aeronautics and Astronautics*, 3(2):380, 1965.

[97] K.J. Bathe and E.L. Wilson. Solution methods for eigen value problems in structural mechanics. *International Journal for Numerical Methods in Engineering*, 6:213–226, 1973.

[98] Z. Qu, R.P. Selvam, and Y. Jung. Model condensation for non-classically damped systems-Part I: Static condensation. *Mechanical Systems and Signal Processing*, 17(5):1003–1016, 2003.

[99] Young Ju Ahn and J.R. Barber. Response of frictional receding contact problems to cyclic loading. *International Journal of Mechanical sciences*, 50(2008):1519–1525, 2008.

[100] A. Thaitirarot, R.C. Flicek, D.A. Hills, and J.R. Barber. The use of static reduction in the finite element solution of two-dimensional frictional contact problems. *Proceedings of the Institution of Mechanical Engineers, Part C: Journal of Mechanical Engineering Science*, pages 1–14, 2013.

[101] Young Ju Ahn. Response of coupled frictional contacts to cyclic loading. *DPhil dissertation*, pages 1–134, 2009.

[102] A. Klarbring, J.R. Barber, and M. Ciavarella. Shakedown in elastic contact problems with coulomb friction. *International Journal of Solids and Structures*, 44(2007):8355–8365, 2007.

[103] N. Cherukkunnath. *SC03 Methods help manual*. Rolls-Royce, 2015.

[104] A. Thaitirarot, R.C. Flicek, D.A. Hills, and J.R. Barber. The use of static reduction in the finite element solution of two-dimensional frictional contact problems. *Journal of Mechanical Engineering Science*, pages 1–14, 2013.

[105] J.R. Barber. Frictional systems subjected to oscillating loads. *Ann. of Solid and Structural Mechanics*, 2:45–55, 2011.

[106] D.B. Bogy. Two edge-bonded elastic wedges of different materials and wedge angles under surface tractions. *Journal of Applied Mechanics*, 38(2):377–386, 1971.

[107] E.E. Gdoutos and P.S. Theocaris. Stress concentrations at the apex of a plane interacting on an elastic half-plane. *Journal of Applied Mechanics*, 42(3):688–692, 1975.

[108] M. Comninou. Stress singularity at a sharp edge in contact problems with friction. *Journal of Applied Mathematics and Physics*, 27(4):493–499, 1976.

Appendix A

User subroutine to assign displacement boundary conditions

An ABAQUS user subroutine was developed to assign the displacement field along the outer circumference of the asymptote, which is consistent with the crack-tip stress intensities and T-stress. The subroutine is executed for all the nodes in each time step and computes the displacement components for the user input values of K_I, K_{II} and σ_0. The program internally converts the coordinate system from cartesian to polar, which originate from the right hand side edge of the notch tip, with the horizontal axis aligning along the bisector.

```
c**********************************************************************
      subroutine  disp(u,kstep,kinc,time,node,noel,jdof,coords)
c**********************************************************************
c
      include 'aba_param.inc'
c
      real*8  u(3),time(2),coords(3)
      integer jdof,kstep,kinc,node,noel
      real*8  a, b, c, e, nu, mu, k1, k2, d0, lambda1, lambda2, th,
     &        x, y, r
      real*8  alpha, uri, urii, uthi, uthii, tinv, bisang, modmixa,pi
      real*8  load, psi, kosvc, numr, denr, x1, y1,uscal
      real*8  l1p1t,l1m1t,l1p1p,l1m1p,l2p1t,l2m1t,l2p1p,l2m1p
      real*8  thb2,th3b2,fr1,fr2,ft1,ft2,ft3
```

```
      parameter (lambda1=0.5d0, lambda2=0.5d0) ! singularity data
      parameter (load=100.0, e=100000.d0, nu = 0.3d0, modmixa=90.0) ! loa

! definition of pi = 3.14....
      pi=4.0d0*datan(1.0d0)

c-----------------------------------------------------------------------
! conversion of each node represented in cartesion CS to polar CS
c-----------------------------------------------------------------------
      x = coords(1)
      y = coords(2)
! Coordinate transform from global to bisector
      bisang=90.0*pi/180.0  ! 90 deg Transformation
      x1 = x*cos(bisang)-y*sin(bisang)
      y1 = x*sin(bisang)+y*cos(bisang)
      x=x1
      y=y1
      r = sqrt(x**2 + y**2)
      th=atan2(y,x)
c
c-----------------------------------------------------------------------
! compute displacement field corresponding to william's stress state
c-----------------------------------------------------------------------
! Calculation of stress intensity factors
      alpha = modmixa*pi/180.0
      mu = e/(2.0d0*(1.0d0+nu)) ! shear modulus/rigidity modulus
! Initialise stress intensity loads
      k1 = 100
      k2 = 50
      T =  200

      a=(-k1/(2.0d0*e))*(r/(2.0d0*pi))**0.5d0
      b=(k2/(2.0d0*e))*(r/(2.0d0*pi))**0.5d0
      c=((r*T)/e)*(1+nu)

      a = a*time(1)
      b = b*time(1)
      c = c*time(1)

      psi=180.0*pi/180.0
```

```
      kosvc=3.0-4.0*nu

! Displacement loads
      thb2=th/2.0d0
      th3b2=3.0d0*th/2.0d0

      if (jdof.eq.1) then
        fr1=(1+nu)*((2*kosvc  - 1.0d0)*cos(thb2) - cos(th3b2))
        fr2=(1+nu)*((-2*kosvc + 1.0d0)*sin(thb2) + 3*sin(th3b2))
        fr3=(cos(th)**2) - nu
        u(1) = (a*fr1 + b*fr2 + c*fr3)
      else if (jdof.eq.2) then
        ft1=(1+nu)*((-2*kosvc - 1.0d0)*sin(thb2) + sin(th3b2))
        ft2=(1+nu)*((-2*kosvc - 1.0d0)*cos(thb2) + 3*cos(th3b2))
        ft3= -(sin(th)*cos(th))
        u(1) = (a*ft1 + b*ft2 + c*ft3)
      end if

      return
      end
```